RICE UNIVERSITY

Resistor Networks and Optimal Grids for the Numerical Solution of Electrical Impedance Tomography with Partial Boundary Measurements

by

Alexander Vasilyevich Mamonov

A Thesis Submitted
in Partial Fulfillment of the
Requirements for the Degree

Doctor of Philosophy

Approved, Thesis Committee:

Liliana Borcea, Noah G. Harding Professor, Chair,
Computational and Applied Mathematics

Danny C. Sorensen, Noah G. Harding Professor,
Computational and Applied Mathematics

William W. Symes, Noah G. Harding Professor,
Computational and Applied Mathematics

Dennis D. Cox, Professor,
Statistics

Houston, Texas

May 2010

Abstract

Resistor Networks and Optimal Grids for the Numerical Solution of Electrical Impedance Tomography with Partial Boundary Measurements

by

Alexander Vasilyevich Mamonov

The problem of Electrical Impedance Tomography (EIT) with partial boundary measurements is to determine the electric conductivity inside a body from the simultaneous measurements of direct currents and voltages on a subset of its boundary. Even in the case of full boundary measurements the non-linear inverse problem is known to be exponentially ill-conditioned. Thus, any numerical method of solving the EIT problem must employ some form of regularization. We propose to regularize the problem by using sparse representations of the unknown conductivity on adaptive finite volume grids known as the optimal grids, that are computed as part of the problem. Then the discretized partial data EIT problem can be reduced to solving the discrete inverse problems for resistor networks. Two distinct approaches implementing this strategy are presented.

The first approach uses the results for the EIT problem with full boundary measurements, which rely on the use of resistor networks with circular graph topology. The optimal grids for such networks are essentially one dimensional objects, which

can be computed explicitly using discrete Fourier transform and rational interpolation with continued fractions. We solve the partial data problem by reducing it to the full data case using the theory of extremal quasiconformal (Teichmüller) mappings.

The second approach is based on resistor networks with the pyramidal graph topology. Such network topology is better suited for the partial data problem, since it allows for explicit treatment of the inaccessible part of the boundary. We present a method of computing the optimal grids for the networks with general topology (including pyramidal), which is based on the sensitivity analysis of both the continuum and the discrete EIT problems. This is the first study of the optimal grids for the case, where reduction to one dimension is not possible.

We present extensive numerical results for the two approaches. We demonstrate both the optimal grids and the reconstructions of smooth and discontinuous conductivities in a variety of domains. The numerical results show several advantages of our approaches compared to the traditional optimization-based methods. First, the inversion based on resistor networks is orders of magnitude faster than any iterative algorithm. Second, our approaches are able to correctly reconstruct both smooth and discontinuous conductivities including those of very high contrast, which usually present a challenge to the iterative or linearization-based inversion methods. Finally, our method does not require any form of artificial regularization via penalty terms. However, our method allows for such regularization to incorporate prior information in the solution.

Acknowledgements

First, I would like to thank my advisor Prof. Liliana Borcea for her guidance, support and help throughout my studies. I thank Dr. Vladimir Druskin of Schlumberger Doll Research for his invaluable advice and many fruitful discussions. I am greatly indebted to my colleague Dr. Fernando Guevara Vasquez, who shared with me his code, studying which I learned as much about the EIT as I did reading books and papers.

I am grateful to faculty of CAAM, in particular my committee members Prof. Danny Sorensen, and Prof. William Symes, who are the strong examples for me of excellency in both research and teaching. I would like to thank Professor of Statistics Dennis Cox for serving on my thesis committee. I would also like to thank Prof. Mark Embree and Prof. Dmitry Leykekhman for valuable teachings and discussions.

I am also grateful to my instructors and mentors at Lomonosov Moscow State University for their guidance on my way to becoming a mathematician. I am particularly indebted to the Chair of Mechanics of Composites Prof. Boris Efimovich Pobedrya, and my undergraduate advisor Prof. Sergey Vladimirovich Sheshenin for their excellent courses in continuum mechanics and numerical analysis.

I dedicate this work to my mother Tatiana L'vovna Mamonova and to the memory of my father Vasily Fedorovich Mamonov.

This work was supported by NSF grants DMS-0604008, DMS-0934594 and by Schlumberger Technology Corporation under the research agreement R62860.

Contents

List of Figures

Chapter 1

Introduction and background

This thesis is concerned with the numerical solution of the Electrical Impedance Tomography (EIT) problem with partial data. We consider an approach based on the theory of inverse problems for resistor networks, and the theory of optimal grids. We begin in this chapter with an overview of the EIT problem. We discuss theoretical results of existence, uniqueness and stability. Then we describe the ill-conditioned nature of the problem. Numerical methods and discretization are discussed next, followed by an example of how the theory of optimal grids provides a crucial link between the discrete and continuum inverse problems.

1.1 Electrical Impedance Tomography: existence, uniqueness and stability

The mathematical problem of Electrical Impedance Tomography is concerned with determining the coefficient of an elliptic equation (the conductivity σ) inside a bounded simply connected domain $\Omega \subset \mathbb{R}^d$, given simultaneous measurements of the Dirichlet data (voltages) and the Neumann data (currents) on the boundary $\partial\Omega = \mathcal{B}$. Explic-

itly, we have

$$\begin{aligned} \nabla \cdot (\sigma(x)\nabla u(x)) &= 0, \quad x \in \Omega, && (1.1) \\ u(x) &= \phi(x), \quad x \in \mathcal{B}, && (1.2) \\ (\Lambda_\sigma \phi)(x) &= \sigma(x)\frac{\partial u}{\partial \nu}(x), \quad x \in \mathcal{B}, && (1.3) \end{aligned}$$

where u is the electric potential, ν in the unit outward normal, and Λ_σ is the *Dirichlet-to-Neumann* (DtN) map. Equation (1.1) is understood in the weak sense, the potential u is in $H^1(\Omega)$, the conductivity $\sigma > 0$ is in $L^\infty(\Omega)$, $\phi \in H^{1/2}(\mathcal{B})$ is the Dirichlet boundary data, and $\Lambda_\sigma : H^{1/2}(\mathcal{B}) \to H^{-1/2}(\mathcal{B})$. We refer to the problem of finding σ given the knowledge of Λ_σ as the continuum EIT. It is also known in the literature as Impedance Computed Tomography, Impedance Imaging, or the Inverse Conductivity problem. The above formulation was first given by Calderon in [22]. Substantial progress has been made since then.

We consider the EIT problem in $d = 2$ spatial dimensions, however for completeness we also present results of existence, uniqueness and stability for higher dimensions. The EIT can also be formulated in terms of the Neumann-to-Dirichlet (NtD) map, which maps boundary currents to boundary voltages. In theory, this formulation is equivalent to the previous one. Working with the NtD map may be advantageous in practice, because the NtD map is smoothing, acting from $\left\{ J \in H^{-1/2}(\mathcal{B}) \mid \int_{\mathcal{B}} J dS = 0 \right\}$ to $H^{1/2}(\mathcal{B})$. In this work we consider the DtN map only, since in two dimensions it can be easily related to the NtD map using convex duality.

According to the definition of Hadamard [45] of a well-posed problem of mathematical physics, it must satisfy three properties: existence, uniqueness, and stability of the solution. We first review the existence and uniqueness results for the EIT.

The first uniqueness results of Kohn and Vogelius [56] were local in nature, i.e. they showed that Λ_σ uniquely determines piecewise analytic σ in dimensions two or higher, and in domains with C^∞ boundary. Independently, Druskin proved the injectivity of the DtN map for piecewise constant conductivities with piecewise smooth interfaces of discontinuity in possibly unbounded domains [35]. He extended the results to piecewise-analytic conductivities in [36]. The first global result was obtained by Sylvester and Uhlmann in [81] for $\sigma \in C^\infty(\overline{\Omega})$, in three or more dimensions and smooth boundary $\mathcal{B}$. An improvement of the Sylvester and Uhlmann result and a constructive reconstruction method based on scattering theory was given by Nachman in [68], for $\sigma \in C^{1,1}(\Omega)$ and $\mathcal{B} \in C^{1,1}$. The global result in two dimensions remained open until another work of Nachman [69], that further relaxed the regularity conditions to $\sigma \in W^{2,p}(\Omega)$, $p > 1$, and domains with Lipschitz boundary. The result was consecutively improved in [20] to $\sigma \in W^{1,p}(\Omega)$, $p > 2$. Finally, the uniqueness question in two dimensions was answered in the most general case of L^∞ conductivities by Astala and Päivärinta in [3]. The question of uniqueness in higher dimensions $d \geq 3$ for L^∞ conductivities is still open.

Note that the above uniqueness results are formulated for scalar-valued σ, i.e. for isotropic conductive media. In anisotropic media the conductivity $\sigma : \mathbb{R}^d \to \mathbb{R}^{d\times d}$ is a symmetric positive-definite matrix valued function, which is not uniquely defined by the DtN map [79, 4]. We limit our study to isotropic conductivities, but we show that in the partial measurement settings certain numerical methods can introduce an artificial anisotropy that should be taken into account.

The main difficulties in solving the EIT problem come from the stability issues. In [1] Alessandrini constructs a simple example of a pair of discontinuous $L^\infty(\Omega)$ conductivities σ_1, σ_2 such that $\|\sigma_1 - \sigma_2\|_\infty = 1$, but $\|\Lambda_{\sigma_1} - \Lambda_{\sigma_2}\|_{H^{1/2}(\mathcal{B})\to H^{-1/2}(\mathcal{B})}$ can be arbitrarily small, which shows that the problem is unstable for general $L^\infty(\Omega)$

conductivities. In the same paper Alessandrini obtains stability estimates in $d \geq 3$ dimensions for $\sigma \in W^{2,\infty}(\Omega)$ (see also [2, 61]). Stability in two spatial dimensions $d = 2$ was shown by Liu in [60] for $\sigma \in W^{2,p}(\Omega)$, $p > 1$, which was improved in Barcelo et. al. [8] to include σ in $C^{1+\alpha}(\Omega)$, $\alpha > 0$. While the above results seem like they make the EIT problem well posed, in practice they are not of much value. Let us consider a typical stability estimate from [9, Theorem 1.1].

Theorem 1.1.1. *Let Ω be Lipschitz domain in the plane. Let σ_1, σ_2 be two planar conductivities satisfying*

- *Ellipticity:* $\left\| \frac{1-\sigma_j}{1+\sigma_j} \right\|_{L^\infty(\Omega)} < \kappa < 1$, $j = 1, 2$,
- *α-regularity:* $\sigma_j \in C^\alpha(\overline{\Omega})$ *with* $\alpha > 0$ *and with a priori bound* $\|\sigma_j\|_{C^\alpha} < L$, $j = 1, 2$,

Then there exists a non-decreasing continuous function $V : \mathbb{R} \to \mathbb{R}$ with $V(0) = 0$, such that

$$\|\sigma_1 - \sigma_2\|_{L^\infty(\Omega)} \leq V\left(\|\Lambda_{\sigma_1} - \Lambda_{\sigma_2}\|_{H^{1/2}(\mathcal{B}) \to H^{-1/2}(\mathcal{B})} \right), \tag{1.4}$$

where V can be taken

$$V(\rho) = C\,|\log(\rho)|^{-a}, \tag{1.5}$$

with positive constants C and a depending on α, κ, L.

First note, that a priori bounds on ellipticity of the differential operator and regularity of the conductivity are required. Second, even if the conductivity is known a priori to have the desired properties, the stability bound has a logarithmic modulus of continuity V. Thus, a linear improvement of the misfit between σ_j requires an exponential improvement of the misfit between the data Λ_{σ_j}. In practice it means that the quality of the solution with any numerical scheme will be severely restricted

by the errors in measuring Λ_σ, as well as by the round-off errors of the finite precision arithmetic. In the work of Mandache [61] it is shown that the inconvenient feature of logarithmic stability is indeed unavoidable for $d \geq 2$ under any a priori assumption of the form

$$\|\sigma_j\|_{C^k(\overline{\Omega})} \leq E, \quad j = 1, 2, \tag{1.6}$$

for any E, and finite $k = 0, 1, 2, \ldots$, i.e. no matter how much regularity we ask from σ_j, the logarithmic stability bound is sharp.

The above stability estimates demonstrate that for all practical purposes the EIT problem is ill-conditioned. Because of the logarithmic nature of stability bounds, we expect the conditioning of the numerical approximations to the continuum EIT problem to deteriorate exponentially fast as the size of discretization is increased. Consequentially, the discrete problem has to be properly regularized. These questions are addressed in chapter 2, where we describe a method of solution of the EIT problem discretized on optimal grids.

1.2 Partial data EIT

In the partial data EIT problem we can measure potentials and currents only on parts of the boundary. We write the mathematical formulation in compact form as follows

$$\begin{aligned} \nabla \cdot (\sigma(x)\nabla u(x)) &= 0, \quad x \in \Omega & (1.7)\\ u(x) &= \phi(x), \quad x \in \mathcal{B}_D, & (1.8)\\ au(x) + b\sigma(x)\frac{\partial u}{\partial \nu}(x) &= 0, \quad x \in \mathcal{B}\backslash\mathcal{B}_D, & (1.9) \end{aligned}$$

where the constants a and a in (1.9) provide us with the choice of enforcing either a homogeneous Dirichlet ($a = 1,\ b = 0$) or Neumann ($a = 0,\ b = 1$) condition, depending on whether the inaccessible part of the boundary is grounded or insulated.

The partial data EIT problem is then to find the conductivity σ given the partial measurements of the current

$$(\Lambda_\sigma \phi)|_{\mathcal{B}_A} = \left(\sigma \frac{\partial u}{\partial \nu}\right)\Big|_{\mathcal{B}_A}, \tag{1.10}$$

where $\mathcal{B}_A \subset \mathcal{B}$ is the *accessible boundary*. In this work we only consider the case $\mathcal{B}_A = \mathcal{B}_D$, however in some of the theoretical studies of the partial data problem other measurements are considered. When the accessible boundary coincides with $\mathcal{B}_D$ we refer to $\mathcal{B}_I = \mathcal{B} \backslash \mathcal{B}_D$ as the *inaccessible boundary*.

It is worth mentioning that many of the works referenced in this section deal with recovery of bounded potentials q of Schrödinger equation $\Delta u + qu = 0$, which can be related to the conductivity σ in (1.7) by

$$q = \frac{\Delta \sqrt{\sigma}}{\sqrt{\sigma}}, \tag{1.11}$$

assuming obvious regularity of σ.

Unlike the classical EIT problem with full data, which has been studied extensively since the early 1980s starting with Calderon's paper [22], most of the global results about existence and uniqueness of the solutions of the partial data EIT were not obtained until 2000s. Before that the existence and uniqueness of the solution to the partial data EIT problem was known only for real-analytic [55] or piecewise real-analytic [56] conductivities in three dimensions (see also [36]).

The first global result of existence and uniqueness was obtained in [21] for $C^2(\overline{\Omega})$

conductivities, in a special setting where the potential is specified on the whole boundary $\mathcal{B}_D = \mathcal{B}$ (which has to be a sphere in three or more dimensions), and $\mathcal{B}_A$ is slightly larger than half of $\mathcal{B}$. The result was subsequently generalized to less restrictive measurement settings in [53].

For two spatial dimensions the first global result for $\sigma \in C^{3+\epsilon}(\overline{\Omega})$, $\epsilon > 0$ was established in [48], however it required $(\mathcal{B} \backslash \mathcal{B}_D) \subset \mathcal{B}_A$ ($a = 1$, $b = 0$), i.e. the current is measured on a subset slightly larger than the grounded part of the boundary. For realistic measurement setups it is more convenient to have the measurements of the current on $\mathcal{B}_D$, which was considered in [47]. Below is a result from [47, Corollary 1.1] that establishes uniqueness of the solution to the partial data EIT problem for the setting we are interested in: $a = 1$, $b = 0$, $\mathcal{B}_A = \mathcal{B}_D$.

Theorem 1.2.1. *Let $\sigma_j \in C^{3+\epsilon}(\overline{\Omega})$, $j = 1, 2$, for some $\epsilon > 0$ be non-negative functions. Assume that*

$$(\Lambda_{\sigma_1}\phi)|_{\mathcal{B}_A} = (\Lambda_{\sigma_2}\phi)|_{\mathcal{B}_A},$$

for any $\phi \in H^{1/2}(\mathcal{B})$, such that supp $\phi \subset \mathcal{B}_D$. Then $\sigma_1 = \sigma_2$.

To the best of our knowledge, no stability results exist yet for the partial data problem in the setting of the Theorem 1.2.1. Obviously, stability of the partial data problem could not be better then logarithmic, as follows from the analysis of the full data case. For the setting with $\mathcal{B}_D = \mathcal{B}$, the estimate exists for the three dimensional problem only with the modulus of continuity of log-log type (see [46]).

1.3 Numerical methods

Since the introduction of the EIT problem in [22] a lot of research has been dedicated to the numerical solution of the problem. Non-linearity and severe ill-conditioning

make such studies challenging. The existing approaches can be sorted into the following groups:

1. Non-iterative algorithms solving a linearized problem;
2. Iterative methods solving the non-linear problem;
3. Direct methods based on integral equations (non-linear problem);
4. Direct methods based on layer stripping (non-linear problem);
5. Optimal grid based methods (non-linear problem).

The first two groups of methods are general techniques, that can be applied to a wide range of inverse problems. Linearization approaches search for the unknown conductivity in the form $\sigma = \sigma_0 + \delta\sigma$, with the inverse problem linearized around a reference conductivity σ_0 (usually a constant), and a perturbation $\delta\sigma$ considered to be small. Calderon proposed in [22] a linearization scheme, that uses complex exponentials to obtain the Fourier transform of $\delta\sigma$. The implementation of his method was given in [23, 52]. Other linearization based methods include one-step Newton algorithms [24, 63, 64], and backprojection algorithms [7, 72]. The iterative methods are usually formulated as an optimization problem with some form of least squares functional and a regularization term added to account for the ill-conditioning of the problem. Examples of output least squares algorithms are given in [10, 13, 12, 31, 32]. Equation-error methods are also used in an iterative framework [85, 57, 54].

The third and the fourth categories of methods solve the full non-linear problem, but unlike the iterative methods require a finite number of steps to do so. The constructive existence and uniqueness proofs of Nachman in $d \geq 3$ dimensions [68], and in $d = 2$ dimensions [69], reduce the non-linear EIT problem to two linear integral

equations in a manner somewhat similar to Gel'fand-Levitan's treatment of inverse spectral problem [42]. These integral equations can be solved numerically using the so-called $\overline{\partial}$-method (dbar-method), which has been successfully implemented in [66, 65, 73, 74].

The layer stripping (peeling) methods determine the unknown conductivity on a subset of Ω adjacent to the boundary, this subset is then stripped away, resulting in an EIT problem on a smaller domain, for which the same step is applied again. Layer stripping methods can be applied directly to a continuum problem [76, 80], or to a discretized one [26].

Finally, the class of methods that we are most interested in are the algorithms based on the use of optimal grids. The optimal grid approach can be used for solving inverse PDE problems as described in the next section. At the core of the method is the separation of the data fitting step and the reconstruction step. In the data fitting step we solve a discrete inverse problem for a resistor network with a DtN map that is obtained via a measurement operator applied to the continuum DtN map. The discrete inverse problem can be solved using either an iterative or a layer stripping method. In the next step, we use the solution of the discrete inverse problem to obtain an approximation of the continuum one at the nodes of a special finite-difference grid, known as an optimal grid. This approximation can be further improved using a Newton-type iteration [15]. Thus, the optimal grid based methods can be viewed as a combination of ideas from different classes of algorithms. The concept of optimal grids is detailed in the next section.

Note that the methods that form the above mentioned groups are usually developed to solve the EIT problem with full boundary measurements. Depending on the class of algorithms, it may be straightforward or difficult to use them in the partial data setting. For example, the linearization or iterative schemes, being the most

general approaches to inverse problems, are the easiest to generalize to solve partial data problems. However, they tend to be inefficient. The linearization approach can usually determine only small perturbations relative to the background conductivity, and the iterative schemes require careful regularization. On the other hand, the direct methods based on layer stripping or Nachman's integral equations are more powerful, but their generalization to partial data cases is non-trivial. In this work we explore different approaches to generalizing the optimal grid reconstruction procedure of [15] to partial data EIT problems.

1.4 Optimal grids for inverse problems

The similarities between the inverse problems in discrete and continuous settings have been observed by a number of authors. For example, consider a one-dimensional inverse spectral problem for the Sturm-Liouville equation

$$\begin{aligned} \frac{\partial}{\partial z}\left(\sigma(z)\frac{\partial u}{\partial z}\right) - \lambda\sigma(z)u(z) &= 0, \quad z \in [0, L], \\ u(0) &= 1, \\ u(L) &= 0, \end{aligned} \tag{1.12}$$

with Dirichlet-to-Neumann map given by $F_\sigma(\lambda) = -\left.\dfrac{\partial u}{\partial z}\right|_{z=0}$. The continuum inverse spectral problem is to determine $\sigma(z)$ for $z \in [0, L]$, given the knowledge of F_σ as a function of λ (this is equivalent to knowing the spectrum of the differential operator in (1.12)). A constructive proof of existence and uniqueness of the solution of this problem is due to Gel'fand and Levitan [42] (see also [59, 62]).

When discretized using a finite difference method on a staggered grid with a three

point stencil, equation (1.12) takes the form

$$Tu = \lambda u, \tag{1.13}$$

where T is a Jacobi matrix (in an appropriately weighted inner product space), with entries determined by

$$\gamma_j = \frac{h_j}{\widehat{\sigma}_j} = \int_{z_j}^{z_{j+1}} \frac{dz}{\sigma(z)}, \quad \widehat{\gamma}_j = \widehat{h}_j \widehat{\sigma}_j = \int_{\widehat{z}_{j-1}}^{\widehat{z}_j} \sigma(z) dz. \tag{1.14}$$

Here z_j, $\widehat{z}_j$ are the primary and dual grid nodes, h_j, $\widehat{h}_j$ are the primary and dual grid steps, and σ_j, $1/\widehat{\sigma}_j$ are the algebraic and harmonic averages of $\sigma(z)$ respectively.

If we are given only the first N poles λ_k and residues y_k of F_σ (i.e. the truncated spectral measure of the differential operator in (1.12)), then we can solve a discrete inverse spectral problem to find the matrix T with eigenvalues λ_k, $k = 1, \ldots, N$ and first components of the eigenvectors equal to y_k, $k = 1, \ldots, N$, (see [25, 37]). This can be done, for example using Lanczos' method [25], or a discrete Gel'fand-Levitan's approach, as shown by Natterer in [70].

While the connection between the discrete and continuum problem exists in the above sense, it is not enough by itself to construct a numerical method that gives an approximation of the solution of the continuum inverse problem. The entries of T depend on the averages of the unknown coefficient σ over cells of a grid, which is unknown. This is where the concept of *optimal grids* comes in.

Optimal grids have been introduced in [6, 5, 50, 38] to obtain very fast (usually exponential) convergence of the finite-difference approximations to $F_\sigma(\lambda)$. The first use of optimal grids in inversion was proposed in [14]. These grids are constructed by solving the discrete inverse problem for a fixed reference conductivity σ_1 (usually

taken as $\sigma_1 \equiv 1$), for which F_{σ_1} is known analytically (or can be computed). The optimal grid spacings are then obtained from T_1 using relations (1.14).

It was established in [16] that the optimal grids are essential to obtaining convergence of the solution of discrete inverse spectral problem to the continuum one. Explicitly, the solution of the discrete inverse problem converges to the true continuum limit if and only if the discretization grid is asymptotically close to the optimal one. This result motivated the use of the optimal grids in the numerical solution of other inverse problems. For example, in [15] the optimal grids were used to solve numerically the EIT problem with full boundary measurements. Our work extends these results to the case of partial data measurements.

Chapter 2

EIT with resistor networks and optimal grids

In this chapter we present a framework for solving the Electrical Impedance Tomography problem numerically using resistor networks and optimal grids. The chapter is organized as follows. First, a finite-volume discretization of the two-dimensional EIT problem on a staggered grid is discussed, and how the resulting system of linear equations resembles that of a resistor network. Properties of the networks with the underlying graphs with topology of circular planar, including a discrete analogue of the inverse problem, are presented in section 2.2. In section 2.3 a connection is made between the discrete and continuum inverse problems, and the notion of optimal grids is introduced. Finally, the optimal grids for the full data EIT in the unit disk are studied in section 2.4.

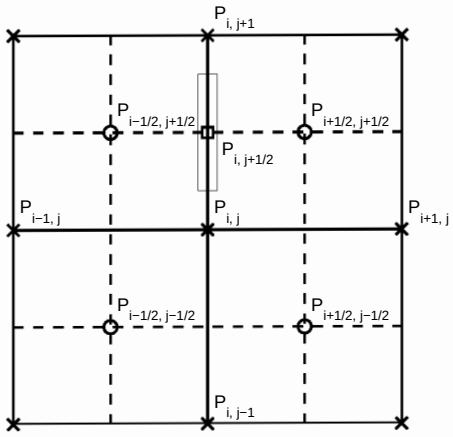

Figure 2.1: Vicinity of a primary node $P_{i,j}$ in a staggered grid. The primary grid lines are solid, and the dual grid lines are dashed. The primary grid nodes are $\times$ and the dual grid nodes are $\circ$. We show the resistor along the primary edge $(P_{i,j+1}, P_{i,j})$ as a rectangle and denote by $\square$ its intersection with the dual edge.

2.1 Finite volume discretization and resistor networks

The use of resistor networks for the numerical solution of EIT can be motivated in the context of finite volume discretizations of (1.1)–(1.2) on staggered grids. Such grids consist of intersecting primary and dual grid lines, which are allowed to be curvilinear. We refer to the intersections of primary (dual) grid lines as the primary (dual) grid nodes. The potential u is discretized at the primary grid nodes, while the current fluxes $\sigma\nabla u$ are discretized at the dual grid nodes.

We illustrate in figure 2.1 the vicinity of an interior primary grid node $P_{i,j}$. Let $C_{i,j}$ be the dual grid cell with boundary

$$\partial C_{i,j} = \Sigma_{i,j+\frac{1}{2}} \cup \Sigma_{i+\frac{1}{2},j} \cup \Sigma_{i,j-\frac{1}{2}} \cup \Sigma_{i-\frac{1}{2},j}, \tag{2.1}$$

the union of the four dual grid segments

$$\Sigma_{i,j\pm\frac{1}{2}} = \left(P_{i-\frac{1}{2},j\pm\frac{1}{2}}, P_{i+\frac{1}{2},j\pm\frac{1}{2}}\right), \quad \Sigma_{i\pm\frac{1}{2},j} = \left(P_{i\pm\frac{1}{2},j-\frac{1}{2}}, P_{i\pm\frac{1}{2},j+\frac{1}{2}}\right).$$

We integrate (1.1) over $C_{i,j}$, and use the divergence theorem to obtain the balance of fluxes across the boundary $\partial C_{i,j}$

$$\int_{C_{i,j}} \nabla\cdot(\sigma\nabla u)dV = \left(\int_{\Sigma_{i,j+\frac{1}{2}}} + \int_{\Sigma_{i+\frac{1}{2},j}} + \int_{\Sigma_{i,j-\frac{1}{2}}} + \int_{\Sigma_{i-\frac{1}{2},j}}\right)\sigma\frac{\partial u}{\partial\nu}dS = 0. \qquad (2.2)$$

The linear algebraic system of equations for the discretized potential is obtained by approximating the boundary integrals in (2.2) with a one-point quadrature rule, and the normal derivatives in the integrands with a two point finite difference. We have

$$\int_{\Sigma_{i,j\pm\frac{1}{2}}} \sigma\frac{\partial u}{\partial\nu}dS \approx \sigma(P_{i,j\pm\frac{1}{2}})\frac{L(\Sigma_{i,j\pm\frac{1}{2}})}{L(\Pi_{i,j\pm\frac{1}{2}})}\left[u(P_{i,j\pm1}) - u(P_{i,j})\right], \qquad (2.3)$$

$$\int_{\Sigma_{i\pm\frac{1}{2},j}} \sigma\frac{\partial u}{\partial\nu}dS \approx \sigma(P_{i\pm\frac{1}{2},j})\frac{L(\Sigma_{i\pm\frac{1}{2},j})}{L(\Pi_{i\pm\frac{1}{2},j})}\left[u(P_{i\pm1,j}) - u(P_{i,j})\right], \qquad (2.4)$$

where $P_{i,j\pm\frac{1}{2}}$ and $P_{i\pm\frac{1}{2},j}$ are the intersections of the primary grid segments

$$\Pi_{i,j\pm\frac{1}{2}} = (P_{i,j}, P_{i,j\pm1}), \quad \Pi_{i\pm\frac{1}{2},j} = (P_{i,j}, P_{i\pm1,j})$$

with the dual grid segments $\Sigma_{i,j\pm\frac{1}{2}}$ and $\Sigma_{i\pm\frac{1}{2},j}$, as shown in figure 2.1. The arc lengths of the primary and dual grid segments are denoted by $L(\Pi)$ and $L(\Sigma)$, respectively.

The system of linear algebraic equations for the discretized potential $u_{i,j} \approx u(P_{i,j})$

is

$$\begin{aligned} \gamma_{i,j+\frac{1}{2}}\left(u_{i,j+1}-u_{i,j}\right)+\gamma_{i+\frac{1}{2},j}\left(u_{i+1,j}-u_{i,j}\right) &+ \\ \gamma_{i,j-\frac{1}{2}}\left(u_{i,j-1}-u_{i,j}\right)+\gamma_{i-\frac{1}{2},j}\left(u_{i-1,j}-u_{i,j}\right) &= 0, \end{aligned} \tag{2.5}$$

where

$$\gamma_{\alpha,\beta}=\sigma(P_{\alpha,\beta})\gamma^{(1)}_{\alpha,\beta}, \tag{2.6}$$

$$(\alpha,\beta)\in\left\{\left(i,j+\frac{1}{2}\right),\left(i+\frac{1}{2},j\right),\left(i,j-\frac{1}{2}\right),\left(i-\frac{1}{2},j\right)\right\}, \tag{2.7}$$

and

$$\gamma^{(1)}_{\alpha,\beta}=\frac{L(\Sigma_{\alpha,\beta})}{L(\Pi_{\alpha,\beta})} \tag{2.8}$$

corresponds to the constant conductivity $\sigma\equiv 1$. Equation (2.6) can be viewed as Kirchhoff's node law for a certain resistor network with graph $\Gamma=(Y,E)$ and the conductance $\gamma: E\to\mathbb{R}_+$. The set of graph vertices Y consists of the primary grid nodes and the set of edges E is comprised of the primary grid segments $\Pi_{\alpha,\beta}$. For the conductance we write $\gamma_{\alpha,\beta}=\gamma\left(\Pi_{\alpha,\beta}\right)$.

2.2 The inverse problem for resistor networks

At the core of our inversion method is the solution of the discrete inverse problem of finding conductances in a resistor network from discrete measurements of the DtN map. We begin in section 2.2.1 with a definition of a DtN map of a resistor network, and a discrete inverse problem. We review the existence and uniqueness of its solution in section 2.2.2. The connection between the continuum and discrete DtN maps is given in section 2.2.3. Finally, we describe in section 2.2.4 the possible approaches to the numerical solution of the discrete inverse problem.

2.2.1 The DtN map of a resistor network

Let us formally define resistor networks, which may or may not correspond to the discretization of an elliptic equation given in the previous section. A *resistor network* is a pair (Γ, γ), where $\Gamma = (Y, E)$ is a graph with vertices (nodes) Y and edges $E \subset Y \times Y$, and $\gamma : E \to \mathbb{R}_+$ is a positive valued *conductance* function. The set Y is the union of two disjoint sets Y_B and Y_I of *boundary* and *interior* vertices. The decomposition $Y = Y_I \cup Y_B$ is needed in what follows to define a discrete analogue of the DtN map. We let

$$n = |Y_B| \tag{2.9}$$

be the number of boundary nodes, and use hereafter the symbol $|\cdot|$ to denote the cardinality of finite sets.

Define a *potential* function $u : Y \to \mathbb{R}$ and denote by u_B and u_I its restriction to the boundary and interior nodes respectively. The potential satisfies Kirchhoff's node law

$$\begin{bmatrix} K_{II} & K_{IB} \\ K_{BI} & K_{BB} \end{bmatrix} \begin{bmatrix} u_I \\ u_B \end{bmatrix} = \begin{bmatrix} 0 \\ J_B \end{bmatrix}, \tag{2.10}$$

where $J_B \in \mathbb{R}^n$ is the vector of currents through the boundary nodes, and K is the symmetric Kirchhoff matrix

$$K_{ij} = \begin{cases} -\gamma[(v_i, v_j)], & \text{if } i \neq j \text{ and } (v_i, v_j) \in E, \\ 0, & \text{if } i \neq j \text{ and } (v_i, v_j) \notin E, \\ \displaystyle\sum_{k:(v_i,v_k)\in E} \gamma[(v_i, v_k)], & \text{if } i = j. \end{cases} \tag{2.11}$$

We write in (2.10) the block structure of K, using the notation K_{XZ} for the block with row indices in $X \subseteq Y$ and column indices in $Z \subseteq Y$.

The DtN map of the network is the matrix $\Lambda_\gamma \in \mathbb{R}^{n\times n}$ that takes u_B to J_B. It equals the Schur complement of K_{II}

$$\Lambda_\gamma = K_{BB} - K_{BI}K_{II}^{-1}K_{IB}, \tag{2.12}$$

which is well defined for non singular K_{II}. As long as the network has a connected graph[1], the invertability of K_{II} follows from the discrete analogue of the maximum principle, as shown in [26, 27, 28].

The discrete inverse problem is to find the conductance function γ given a network with known graph Γ and DtN map Λ_γ. The solvability of the discrete inverse problem depends on the topological properties of Γ, that we review below.

2.2.2 Solvability of the discrete inverse problem

In this work we study EIT in two dimensions, in simply connected domains $\Omega \subset \mathbb{R}^2$. By the Riemann mapping theorem, all such domains are conformally equivalent, so we can identify Ω with the unit disk $\mathbb{D}$ in $\mathbb{R}^2$ or in $\mathbb{C}$. Thus, it is natural to consider networks with the so-called *circular planar* graphs Γ which can be embedded in the plane, without self-intersections of the edges, in such a way that all interior nodes are in the unit disk, and the boundary nodes are on the unit circle $\partial\mathbb{D}$.

Following [26, 27, 28], we number the boundary nodes $Y_B = \{v_1, \ldots, v_n\}$ so that they appear in a circular (clockwise or counterclockwise) order on $\partial\mathbb{D}$. Consider a pair $(P;Q)$ of subsets of Y_B, with $P = \{v_{i_1}, \ldots, v_{i_k}\}$, $Q = \{v_{j_k}, \ldots, v_{j_1}\}$ belonging to disjoint arcs of $\partial\mathbb{D}$. The pair is called *circular* if the nodes $\{v_{i_1}, \ldots, v_{i_k}; v_{j_k}, \ldots, v_{j_1}\}$ appear in circular order on $\partial\mathbb{D}$.

[1] We say that the graph $\Gamma = (Y, E)$ is connected when each pair of vertices in Y is connected by at least one set of edges in E.

A circular pair $(P;Q)$ is called *connected*, if there exist k disjoint paths α_s connecting v_{i_s} and v_{j_s}, $s = 1, \ldots, k$. The boundary nodes are allowed in α_s only as the first and the last nodes (the paths must not touch the boundary). We let $\pi(\Gamma)$ be the set of all connected circular pairs, and we say that the graph is *well connected* if all circular pairs are in $\pi(\Gamma)$.

Once we define $\pi(\Gamma)$ we can address the question of whether the discrete inverse problem is uniquely solvable. This question is closely related to the topology of the graph Γ. For circular planar graphs, the question was resolved in [27], using the theory of *critical networks*.

Let Γ' be the graph obtained by removing one edge in $\Gamma = (Y, E)$. The edge can be removed either by deletion or by contraction. Then, the network with graph Γ is called *critical* if removing any edge breaks some connection in $\pi(\Gamma)$ (i.e. $\pi(\Gamma') \subset \pi(\Gamma)$).

It is shown in [27] that the discrete inverse problem for a network with given circular planar graph has a unique solution if and only if it is critical and the data matrix Λ_γ belongs to the set $\mathcal{D}_n$ of DtN maps of well connected networks. The set $\mathcal{D}_n$ is defined in [27]. It consists of all symmetric matrices $\Lambda_\gamma \in \mathbb{R}^{n\times n}$ satisfying the conservation of currents condition

$$\Lambda_\gamma \mathbf{1} = \mathbf{0}, \tag{2.13}$$

and whose *circular minors* are totally non-positive. A circular minor of Λ_γ is a submatrix $(\Lambda_\gamma)_{PQ}$ with row indices in P and column indices in Q, where $(P;Q)$ is a circular pair. The total non-positivity means that

$$\det\left[-(\Lambda_\gamma)_{PQ}\right] \geq 0. \tag{2.14}$$

Equality in (2.14) occurs if and only if $(P;Q) \notin \pi(\Gamma)$. Thus, in a well connected network the inequality (2.14) is always strict.

2.2.3 From the continuum to the discrete DtN map

To connect the continuum EIT problem with discrete inverse problem for resistor network, we relate the matrix valued DtN map Λ_γ of a network to the continuum DtN map Λ_σ. We do so my means of linear measurement operators

$$\mathcal{M}_n : \left(H^{1/2}(\mathcal{B}) \to H^{-1/2}(\mathcal{B})\right) \to \mathbb{R}^{n\times n}. \tag{2.15}$$

Following [15, 44], we define the operators $\mathcal{M}_n$ with a set of n non-negative *measurement functions* χ_j with disjoint supports on $\mathcal{B}$. The measurement functions are normalized by

$$\int_{\mathcal{B}} \chi_j(x) dS_x = 1, \qquad j = 1, \dots, n. \tag{2.16}$$

We can think of them as modeling the support of electrodes attached to the boundary. The symmetric matrix $\mathcal{M}_n(\Lambda_\sigma)$ has off-diagonal entries

$$(\mathcal{M}_n(\Lambda_\sigma))_{i,j} = \langle \chi_i, \Lambda_\sigma \chi_j \rangle, \quad i \neq j, \tag{2.17}$$

where $\langle \cdot, \cdot \rangle$ is the duality pairing between $H^{1/2}(\mathcal{B})$ and $H^{-1/2}(\mathcal{B})$, and the diagonal entries are given by

$$(\mathcal{M}_n(\Lambda_\sigma))_{i,i} = -\sum_{j\neq i} \langle \chi_i, \Lambda_\sigma \chi_j \rangle, \quad i = 1, \dots, n, \tag{2.18}$$

which ensures that $\mathcal{M}_n(\Lambda_\sigma)$ satisfies the conservation of current condition.

Alternatively, we can consider the *pointwise* measurements of the DtN map. For

a sufficiently regular σ, the first order pseudodifferential operator Λ_σ can be written in an integral form as

$$(\Lambda_\sigma \phi)(x) = \int_{\mathcal{B}} \mathcal{K}_\sigma(x,y)\phi(y)dS_y, \qquad x \in \mathcal{B}, \tag{2.19}$$

where $\mathcal{K}_\sigma(x,y)$ is a symmetric kernel continuous away from the diagonal [51]. The pointwise measurement operator $\mathcal{M}_n$ is defined at the points $x_j \in \mathcal{B}$, $j = 1, \ldots, n$, by

$$(\mathcal{M}_n(\Lambda_\sigma))_{i,j} = \begin{cases} \mathcal{K}_\sigma(x_i, x_j), & i \neq j, \\ -\sum\limits_{k \neq i} \mathcal{K}_\sigma(x_i, x_k), & i = j. \end{cases} \tag{2.20}$$

These definitions do not distinguish between the full or partial boundary measurement setups. The partial data case corresponds to supp$\chi_j \subset \mathcal{B}_A$ for (2.17), or $x_j \in \mathcal{B}_A$ for (2.20).

Other measurement operators that use more accurate electrode models, such as the "complete electrode" model [75] can be used in principle. The crucial question is whether the range of the operators belongs to the set $\mathcal{D}_n$ of DtN maps of well connected networks. This is the case for the operators (2.20) and (2.17), as proved in [51] and [15, 44], respectively. Then, we can write that

$$\Lambda_\gamma = \mathcal{M}_n(\Lambda_\sigma), \tag{2.21}$$

for some conductance γ, and conclude based on the results reviewed in section 2.2.2, that there exists a unique network with given critical circular planar graph Γ and DtN map Λ_γ [27, 30].

2.2.4 Solving the discrete inverse problem

Given $\mathcal{M}_n(\Lambda_\sigma) \in \mathcal{D}_n$ we would like to construct an efficient algorithm of solving the discrete inverse problem (2.21). This can be done with at least two approaches.

The first approach is a direct layer peeling (invariant imbedding) method which solves the nonlinear EIT problem in a finite number of algebraic operations. In this work we use the networks with two different topologies of Γ. For the networks with *circular* graphs the layer peeling algorithm is given in [26]. For *pyramidal* networks the algorithm is presented in chapter 4. The layer peeling algorithm begins by determining the conductances in the outermost layer adjacent to the boundary nodes. Then it peels off the layer and proceeds inwards. The algorithm stops when the innermost layer of resistors is reached. The advantage of layer peeling is that it is fast and explicit. The disadvantage is that it quickly becomes unstable, as the number of layers grows. This is a manifestation of the ill-conditioning of the discrete inverse problem, which is expected given the instability of the continuum EIT.

The second approach is to solve the discrete EIT problem with non-linear, regularized least squares, as in [17]. In general, it is unclear how to regularize the least squares for network recovery using penalty terms, because we cannot speak of regularity assumptions (such as total variation) in the discrete setting. We have recovered in [17] networks with optimization using a Gauss-Newton iteration regularized with the SVD truncation of the Jacobian. Adaptive SVD truncation of the Jacobian allows the Gauss-Newton iteration to converge without the use of artificial penalty terms. The advantage of optimization is that in general it allows the recovery of larger networks than layer peeling. The downside is the increased computational cost and the possibility of the method being trapped in local minima.

All the computations in this work are with layer peeling, which we regularize by

restricting n as follows. We solve a sequence of discrete inverse problems for increasing n, until our layer peeling method fails to produce positive conductances. Then we set n to the last but one value in the sequence, and accept as the solution of the inverse problem the non-negative conductance obtained from (2.21).

2.3 From the discrete to the continuum inversion: the optimal grids

Once we have determined the discrete conductance γ, the question is how to use it to approximate the conductivity σ, the solution of the continuum EIT problem. As shown in (2.6), we must also have information about the finite volumes grid to approximate $\sigma(P_{\alpha,\beta})$ from the knowledge of $\gamma_{\alpha,\beta}$. This leads us to the construction of the optimal grids, which are computed from the resistor networks with the same graph and DtN map

$$\Lambda_{\gamma^{(1)}} = \mathcal{M}_n(\Lambda_1). \tag{2.22}$$

Here, Λ_1 is the continuum DtN map for constant conductivity $\sigma \equiv 1$, and $\gamma^{(1)}$ is the conductance (2.8).

Thus, the optimal grids are computed so that finite volumes discretizations compute $\Lambda_{\gamma^{(1)}}$ exactly. Then, we can estimate the conductivity at points $P_{\alpha,\beta}$, the intersections of the primary and dual grid segments, by

$$\sigma(P_{\alpha,\beta}) \approx \sigma^\star(P_{\alpha,\beta}) = \frac{\gamma_{\alpha,\beta}}{\gamma^{(1)}_{\alpha,\beta}}. \tag{2.23}$$

The *reconstruction mapping* $\mathcal{Q}_n : \mathcal{D}_n \to \mathcal{S}$ is defined on the set $\mathcal{D}_n$ of discrete DtN maps, with values in $\mathcal{S}$, the set of positive and bounded conductivities. It takes the

measurements $\mathcal{M}_n(\Lambda_\sigma)$ to the piecewise linear interpolation of the values of $\sigma^\star$ on the optimal grid.

Finally, the images can be improved further using a Gauss-Newton iteration that minimizes the objective function

$$\mathcal{O}(\sigma^s) = \|\mathcal{Q}_n[\mathcal{M}_n(\Lambda_\sigma^s)] - \mathcal{Q}_n[\mathcal{M}_n(\Lambda_\sigma)]\|_2^2 \tag{2.24}$$

over search conductivities $\sigma^s \in \mathcal{S}$. Note that $\mathcal{Q}_n$ is used here as a preconditioner of the forward map $\mathcal{F}_n : S \to \mathcal{D}_n$, which takes $\sigma^s \in \mathcal{S}$ to $\mathcal{M}_n(\Lambda_\sigma^s)$. How good a preconditioner $\mathcal{Q}_n$ is depends on the extrapolation properties of the optimal grids. That is to say, how accurate does the finite volumes approximation of $\mathcal{M}_n(\Lambda_\sigma)$ remain for a wide class of conductivity functions that include the constant $\sigma \equiv 1$. Illustrations of the good extrapolation properties of optimal grids, for various measurement setups, are in [16, 15, 44, 14, 18].

There is only one part of the inversion algorithm outlined above that is sensitive to the measurement setup. It is the definition of the optimal grid, and therefore of the reconstruction mapping $\mathcal{Q}_n$. The optimization (2.24) was studied in detail in [15, 44] and is not presented here. An important observation is that we can incorporate various types of prior information in (2.24), for example via the addition of penalty terms. Thus, our approach is compatible with all traditional regularization techniques, such as Tikhonov [83, 84] or total variation regularizations.

2.4 Optimal grids for the full data EIT in the unit disk

One of the two approaches to the numerical solution of the partial data EIT presented in this work is based on the construction of optimal grids for the full data problem in the unit disk. Tensor product discretization of the full data problem in $\mathbb{D}$ leads to circular resistor networks that are reviewed in section 2.4.1. The discretization itself is outlined in section 2.4.2. The optimal grids are computed for the constant reference conductivity $\sigma \equiv 1$, which leads to layered circular networks discussed in sections 2.4.3–2.4.4. The inverse problem for layered networks can be solved using rational interpolation, and in the case $\sigma \equiv 1$ an explicit solution can be obtained whose properties are presented in section 2.4.5.

2.4.1 Circular resistor networks

Following [15, 44] we consider networks with a special topology, as illustrated in figure 2.2. These networks are called in [26] *circular resistor networks*, and are denoted by $C(l, n)$. The notation indicates that the network has l layers with n resistors in each layer. These resistors may be aligned along the radius (radial resistors), or they may be transversal to the radius (angular resistors). The layers of radial and angular resistors alternate, with the innermost layer being radial.

It is shown in [15, 44] that the graph of $C(l, n)$ is critical if and only if n is odd and $l = (n-1)/2$. This is why we consider in here circular resistor networks of the form $C\left((n-1)/2, n\right)$, with odd n. In what follows, it is convenient to use an integer parameter m and a binary $m_{1/2} \in \{0, 1\}$, such that the number of layers is $l = 2m + m_{1/2} + 1$, where $m_{1/2}$ determines if the outer layer in $C(l, n)$ is radial

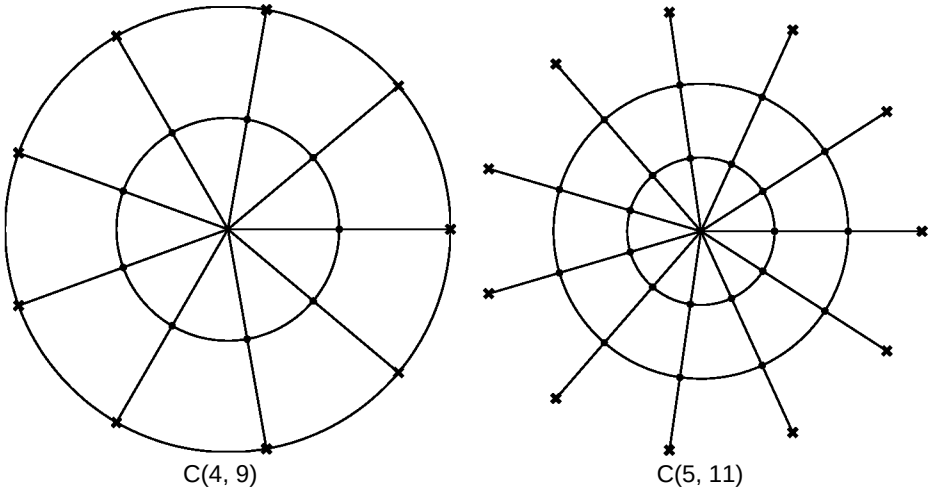

Figure 2.2: Circular resistor networks $C(l, n)$ with critical graphs: $l = (n-1)/2$. Interior nodes are $\bullet$, boundary nodes are $\times$.

($m_{1/2} = 0$) or circular ($m_{1/2} = 1$). For the conductances in a circular network we use notation $\gamma_{j,k}$, $j = 1, \ldots, m+1$, $k = 1, \ldots, n$, for the conductances of radial resistors, and $\widehat{\gamma}_{j,k}$, $j = 2 - m_{1/2}, \ldots, m+1$, $k = 1, \ldots, n$, for the conductances of angular resistors.

2.4.2 Tensor product discretization in the unit disk

Let us consider equation (1.1) in the unit disk $\mathbb{D} = \{(r, \theta) \mid r \in (0, 1],\ \theta \in [0, 2\pi]\}$ in polar coordinates

$$\frac{1}{r}\frac{\partial}{\partial r}\left(r\sigma(r,\theta)\frac{\partial}{\partial r}u\right) + \frac{1}{r^2}\frac{\partial}{\partial \theta}\left(\sigma(r,\theta)\frac{\partial}{\partial \theta}u\right) = 0. \tag{2.25}$$

The continuum EIT problem for (2.25) with full boundary measurements has the important property of rotational invariance for layered conductivities $\sigma(r, \theta) = \sigma(r)$, which of course includes the case $\sigma \equiv 1$. To maintain this rotational invariance in the discrete setting, the measurements of the DtN map must be centered at equidistant

points on $\partial\mathbb{D}$. Explicitly, the measurement functions $\chi_j(\theta)$ are angular translations of the same function $\chi(\theta)$,

$$\chi_k(\theta) = \chi(\theta - \theta_k), \tag{2.26}$$

such that supp$\chi \subset (\widehat{\theta}_0, \widehat{\theta}_1)$, where $\theta_k = 2\pi(k-1)/n$ and $\widehat{\theta}_k = 2\pi(k-1/2)/n$ are the primary and dual boundary grid nodes respectively, for $k = 1, \ldots, n$.

Then, the problem simplifies for layered conductivities, because when taking Fourier transforms in θ, the problem becomes one dimensional. The same simplification can be made in the discrete seting, by taking the discrete Fourier transform, provided that we have a tensor product discretization grid with the boundary nodes given above. The placement of the radial nodes in this tensor product grid is obtained as we describe below.

The radial component of the grid is staggered and the primary radii r_j and the dual radii $\widehat{r}_j$ are ordered as

$$1 = r_1 = \widehat{r}_1 > r_2 > \widehat{r}_2 > \ldots > r_{m+1} > \widehat{r}_{m+1} > r_{m+2} > 0, \quad \text{for} \quad m_{1/2} = 0, \tag{2.27}$$

$$1 = \widehat{r}_1 = r_1 > \widehat{r}_2 > r_2 > \ldots > r_{m+1} > \widehat{r}_{m+2} > r_{m+2} > 0, \quad \text{for} \quad m_{1/2} = 1. \tag{2.28}$$

To determine these radii, we must solve a discrete EIT problem to get $\gamma^{(1)}$, $\widehat{\gamma}^{(1)}$ from (2.22). The method of solution is similar to that of finding γ, $\widehat{\gamma}$ from (2.21).

Consistent with the notation in (2.27) and (2.28), the general formulas (2.6) become

$$\gamma_{j,k} = \quad \sigma(\widehat{r}_{j+m_{1/2}}, \theta_k)\frac{\widehat{r}_{j+m_{1/2}} h_\theta}{r_j - r_{j+1}}, \qquad j = 1, \ldots, m+1, \tag{2.29}$$

$$\widehat{\gamma}_{j,k} = \quad \sigma(r_j, \widehat{\theta}_k)\frac{\widehat{r}_{j+m_{1/2}-1} - \widehat{r}_{j+m_{1/2}}}{r_j h_\theta}, \qquad j = 2 - m_{1/2}, \ldots, m+1, \tag{2.30}$$

where $h_\theta = 2\pi/n$ is the angular grid step and $k = 1, \ldots, n$. We refer to these equations as the *averaging formulas*.

Since the family of measurement functions $\chi_k(\theta)$ is chosen to be rotationally invariant, the matrix $\mathcal{M}_n(\Lambda_1)$ is circulant. Thus, in the case $\sigma \equiv 1$, the solution $\gamma_{j,k}^{(1)}$, $\widehat{\gamma}_{j,k}^{(1)}$ of (2.22) does not depend on the angular index k, and the resulting optimal grid is indeed a tensor product grid. Once the conductances $\gamma_j^{(1)}$, $\widehat{\gamma}_j^{(1)}$ are known, the radii of the optimal grid are obtained sequentially from equations (2.29)–(2.30), starting from the boundary with $r_1 = \widehat{r}_1 = 1$. We obtain

$$r_{j+1} = r_j - h_\theta \widehat{r}_{j+m_{1/2}} / \gamma_j^{(1)}, \quad j = 1, \ldots, m+1, \tag{2.31}$$

$$\widehat{r}_{j+1} = \widehat{r}_j - h_\theta r_{j+1-m_{1/2}} \widehat{\gamma}_{j+1-m_{1/2}}^{(1)}, \quad j = 1, \ldots, m+m_{1/2}. \tag{2.32}$$

Note that the averaging formulas (2.29)–(2.30) correspond to the discretization of the forward problem. However, we use them for the conductances $\gamma_{j,k}$ and $\widehat{\gamma}_{j,k}$ that solve the discrete inverse problem. These conductances are not the same as in the forward problem, unless we use a grid that makes the averaging formulas exact. The results in [15, 44] show that the optimal grids that make the averaging formulas exact in the case $\sigma \equiv 1$, also give a good approximation for a wider class of conductivities.

Note also that formulas (2.29)–(2.30) and (2.31)–(2.32) are not the only possible relations that can be used to determine the grid from $\gamma_j^{(1)}$, $\widehat{\gamma}_j^{(1)}$. In fact a different set of relations was used in [15, 44]. We refer to these relations as log-averaging, and give their definition in the following sections.

Finally, there are alternative choices of the measurement operator. In particular, in the case of layered conductivities, there exists a measurement operator that leads to an explicit solution of the discrete EIT problem [11], which can then be used to prove certain properties of the optimal grids, as we show next.

2.4.3 Alternative measurements for the layered problem

Let us consider in more detail the case of layered conductivity $\sigma(r,\theta)=\sigma(r)$. From the rotational symmetry of the layered problem it follows that $e^{ik\theta}$ are the eigenfunctions of the DtN map

$$\Lambda_\sigma e^{ik\theta}=R_\sigma(k)e^{ik\theta},\quad k\in\mathbb{Z}, \tag{2.33}$$

where the eigenvalues $R_\sigma(k)=R_\sigma(-k)>0$ are given in terms of the *admittance* function R_σ, which can be extended to the whole complex plane in terms of the spectral measure of the differential operator (2.25). A trivial calculation in the case $\sigma\equiv 1$ shows that

$$R_1(\lambda)=|\lambda|. \tag{2.34}$$

Thus, we can formally write

$$\Lambda_1=\sqrt{-\frac{\partial^2}{\partial\theta^2}}. \tag{2.35}$$

In what follows it is convenient to define $\beta_\sigma(\lambda)=R_\sigma(\lambda)/|\lambda|$.

Our goal is to derive a discrete analogue of (2.35), which is possible if we introduce the measurement operator $\mathcal{M}_n^*$ defined below. Instead of using a single set of measurement functions χ_k, we consider two families ζ_k and η_j, where ζ_k are the eigenfunctions of Λ_σ, and η_j are the indicator functions of intervals $(\widehat{\theta}_j,\widehat{\theta}_{j+1})$. Then the vector of measured currents $J^{(k)}$ is given by

$$J_j^{(k)}=\int_0^{2\pi}\eta_j(\theta)\left(\Lambda_\sigma\zeta_k\right)(\theta)d\theta=\beta_\sigma(k)\int_{\frac{2\pi}{n}(j-1/2)}^{\frac{2\pi}{n}(j+1/2)}|k|e^{ik\theta}d\theta, \tag{2.36}$$

where $j=1,\dots,n$ and $k=-(n-1)/2,\dots,(n-1)/2$.

Let $\zeta_j^{(k)}=\zeta_k(\theta_j)=e^{i\frac{2\pi kj}{n}}$ be the components of the vector of boundary potential at the primary grid nodes. The action of the measurement operator $\mathcal{M}_n^*(\Lambda_\sigma)$ on vectors

$\zeta^{(k)}$ is

$$\mathcal{M}_n^*(\Lambda_\sigma)\zeta^{(k)} = J^{(k)}. \tag{2.37}$$

Rewriting (2.36) we observe that

$$J_j^{(k)} = 2\beta_\sigma(k)\left|\sin\left(\frac{\pi k}{n}\right)\right| e^{i\frac{2\pi kj}{n}}. \tag{2.38}$$

Using notation $\omega_k^{(n)} = 2|\sin(\pi k/n)|$ we finally arrive at

$$\mathcal{M}_n^*(\Lambda_\sigma)\zeta^{(k)} = \beta_\sigma(k)\omega_k^{(n)}\zeta^{(k)}, \quad k = -\frac{n-1}{2}, \ldots, \frac{n-1}{2}. \tag{2.39}$$

Consider a symmetric circulant matrix $\Delta^{(n)} \in \mathbb{R}^{n\times n}$ given by

$$\Delta^{(n)} = \begin{bmatrix} -2 & 1 & 0 & \ldots & \ldots & 0 & 1 \\ 1 & -2 & 1 & 0 & \ldots & 0 & 0 \\ 0 & 1 & -2 & \ddots & \ddots & \vdots & \vdots \\ \vdots & 0 & \ddots & \ddots & \ddots & 0 & \vdots \\ \vdots & \vdots & \ddots & \ddots & -2 & 1 & 0 \\ 0 & 0 & \ldots & 0 & 1 & -2 & 1 \\ 1 & 0 & \ldots & \ldots & 0 & 1 & -2 \end{bmatrix}. \tag{2.40}$$

Up to a scaling factor $1/h_\theta^2$ (2.40) is a finite difference discretization of the second derivative on a three point stencil at equidistant nodes θ_k. Since $\Delta^{(n)}$ is circulant, its eigenvectors are $\zeta^{(k)}$ and its eigenvalues λ_k are the discrete Fourier transform of its first column [29, 43]

$$\lambda_k = -2 + e^{i\frac{2\pi k}{n}} + e^{-i\frac{2\pi k}{n}} = -\left(\omega_k^{(n)}\right)^2. \tag{2.41}$$

Combining (2.39) with (2.41) it is easy to observe that (2.39) for $\sigma \equiv 1$ ($\beta_1 \equiv 1$) is a discrete analogue of (2.35)

$$\mathcal{M}_n^*(\Lambda_1) = \sqrt{-\Delta^{(n)}}. \tag{2.42}$$

Note that while (2.42) is a direct analogue of (2.35), it is not clear that there exist a network with a DtN map $\mathcal{M}_n^*(\Lambda_1)$, since the results of [51, 15, 44] are only applicable to measurements (2.20) and (2.17). We show below that (2.42) is indeed compatible with a layered resistor network, which can be recovered using rational interpolation.

2.4.4 Layered networks and rational interpolation

A layered resistor network is a network, in which the values of conductances do not depend on angular index, i.e. $\gamma_{j,s} = \gamma_j$, $\widehat{\gamma}_{j,s} = \widehat{\gamma}_j$. Let us for now consider a critical circular network with $m_{1/2} = 0$, therefore $n = 4m + 3$. The Kirchhoff law is

$$\gamma_{j-1}(u_{j,s} - u_{j-1,s}) + \gamma_j(u_{j,s} - u_{j+1,s}) + \widehat{\gamma}_j(2u_{j,s} - u_{j,s+1} - u_{j,s-1}) = 0, \tag{2.43}$$

where $j = 2, \dots, m+1$, $s = 1, \dots, n$, $u_{m+2} = 0$, the Dirichlet boundary condition is $u_{1,s} = \phi_s$, and the boundary currents are given by $J_s = \gamma_1(u_{1,s} - u_{2,s})$. The difference operator in the third term of (2.43) is nothing but $-\Delta^{(n)}$. Since the eigenvectors of $\mathcal{M}_n^*(\Lambda_1)$ and $\Delta^{(n)}$ are the same, we can do a discrete Fourier transform of (2.43),

$$u_{j,s} = \sum_{k=-(n-1)/2}^{(n-1)/2} a_j^{(k)} e^{i\frac{2\pi k s}{n}}, \tag{2.44}$$

and obtain from (2.42)

$$\gamma_{j-1}(a_j^{(k)} - a_{j-1}^{(k)}) + \gamma_j(a_j^{(k)} - a_{j+1}^{(k)}) + \left(\omega_k^{(n)}\right)^2 \widehat{\gamma}_j a_j^{(k)} = 0. \tag{2.45}$$

Let $b_j^{(k)} = \gamma_j(a_j^{(k)} - a_{j+1}^{(k)})$, then the boundary current is $b_1^{(k)}$, and we may write $\lambda_k = \frac{b_1^{(k)}}{a_1^{(k)}}$, if we normalize $a_1^{(k)} = 1$. From the definition of $b_j^{(k)}$ and from (2.45) we derive

$$a_j^{(k)} = a_{j+1}^{(k)} + \frac{1}{\gamma_j} b_j^{(k)}, \tag{2.46}$$

$$b_j^{(k)} = b_{j+1}^{(k)} + \left(\omega_k^{(n)}\right)^2 \widehat{\gamma}_{j+1} a_{j+1}^{(k)}, \tag{2.47}$$

which gives us the expansion

$$\frac{b_j^{(k)}}{a_j^{(k)}} = \cfrac{1}{\cfrac{1}{\gamma_j} + \cfrac{1}{\widehat{\gamma}_{j+1}\left(\omega_k^{(n)}\right)^2 + \cfrac{b_{j+1}^{(k)}}{a_{j+1}^{(k)}}}}, \tag{2.48}$$

which we can apply recursively to obtain the expression for the eigenvalues of the DtN map of a layered network

$$\lambda_k = R^{(n)}\left(\omega_k^{(n)}\right) = \cfrac{1}{\cfrac{1}{\gamma_1} + \cfrac{1}{\widehat{\gamma}_2\left(\omega_k^{(n)}\right)^2 + \ldots + \cfrac{1}{\cfrac{1}{\gamma_m} + \cfrac{1}{\widehat{\gamma}_{m+1}\left(\omega_k^{(n)}\right)^2 + \gamma_{m+1}}}}}. \tag{2.49}$$

By analogy to the continuum case, we call $R^{(n)}(\lambda)$ the discrete admittance function. Recall that equation (2.49) holds for $m_{1/2} = 0$. In the case $m_{1/2} = 1$ the discrete

admittance takes the form

$$R^{(n)}(\lambda) = \widehat{\gamma}_1\lambda^2 + \cfrac{1}{\cfrac{1}{\gamma_1} + \cfrac{1}{\widehat{\gamma}_2\lambda^2 + \ldots + \cfrac{1}{\cfrac{1}{\gamma_m} + \cfrac{1}{\widehat{\gamma}_{m+1}\lambda^2 + \gamma_{m+1}}}}}. \tag{2.50}$$

Equations (2.49) and (2.50) hold for any layered resistor network with, not just for the network corresponding to $\mathcal{M}_n^*(\Lambda_1)$, which we are interested in. The discrete admittance $R^{(n)}$ is related to continuum one via the rational interpolation, which has the form

$$R^{(n)}\left(\omega_k^{(n)}\right) = \omega_k^{(n)}\beta_\sigma(k), \quad k = 1, \ldots, (n-1)/2. \tag{2.51}$$

It follows from the results of [49] that the rational interpolation problem (2.51) admits a solution of the form (2.49) or (2.50) with positive coefficients γ_j, $\widehat{\gamma}_j$. Thus, $\mathcal{M}_n^*(\Lambda_\sigma)$ is indeed DtN map of a resistor network. Moreover, in the case $\sigma \equiv 1$

$$R^{(n)}\left(\omega_k^{(n)}\right) = \omega_k^{(n)}$$

the conductances admit an analytic expression

$$\gamma_j^{(1)} = \tan\left(\frac{\pi(2m+3-2j)}{n}\right), \quad j = 1, \ldots, m+1, \tag{2.52}$$

$$\widehat{\gamma}_j^{(1)} = \cot\left(\frac{\pi(2m+4-2j)}{n}\right), \quad j = 2 - m_{1/2}, \ldots, m+1, \tag{2.53}$$

as shown in [11]. These expressions allow us to establish the properties of the optimal grids, as we show in the next section.

2.4.5 Properties of optimal grids

To study the properties of the optimal grids it is easier to work with the log-averaging formulas used in [15, 44] instead of the averaging formulas (2.29)–(2.30). The log-averaging formulas are

$$\gamma_{j,k} = \sigma(\widehat{r}_{j+m_{1/2}}, \theta_k)\frac{h_\theta}{\log\left(\frac{r_j}{r_{j+1}}\right)},\ j = 1, \ldots, m+1,\ k = 1, \ldots, n, \tag{2.54}$$

$$\widehat{\gamma}_{j,k} = \sigma(r_j, \widehat{\theta}_k)\frac{\log\left(\frac{\widehat{r}_{j+m_{1/2}-1}}{\widehat{r}_{j+m_{1/2}}}\right)}{h_\theta},\ j = 2 - m_{1/2}, \ldots, m+1,\ k = 1, \ldots, n. \tag{2.55}$$

The radii of the optimal grid take the form

$$r_{j+1} = \exp\left(-h_\theta \sum_{s=1}^{j} \frac{1}{\gamma_s^{(1)}}\right), \quad j = 1, \ldots, m+1 \tag{2.56}$$

$$\widehat{r}_{j+m_{1/2}} = \exp\left(-h_\theta \sum_{s=2-m_{1/2}}^{j} \widehat{\gamma}_s^{(1)}\right), \quad j = 2 - m_{1/2}, \ldots, m+1. \tag{2.57}$$

We show in figure 2.3 the radial optimal grids corresponding to the measurement operators $\mathcal{M}_n(\Lambda_1)$ and $\mathcal{M}_n^*(\Lambda_1)$ and two choices of averaging formulas: (2.29)–(2.30) and (2.56)–(2.57). We observe that the grids obtained from the same averaging formulas but different measurement operators are almost indistinguishable. There is a slight difference between the grids given by the two averaging formulas, but this difference is mostly near the origin $r = 0$. We have observed from extensive numerical experiments, for a variety of grid sizes, that the optimal grids are robust with respect to the choice of measurement operator and averaging formulas.

The grids presented in figure 2.3 share two common properties. First, they are indeed staggered with interlacing primary and dual nodes. Second, they are refined

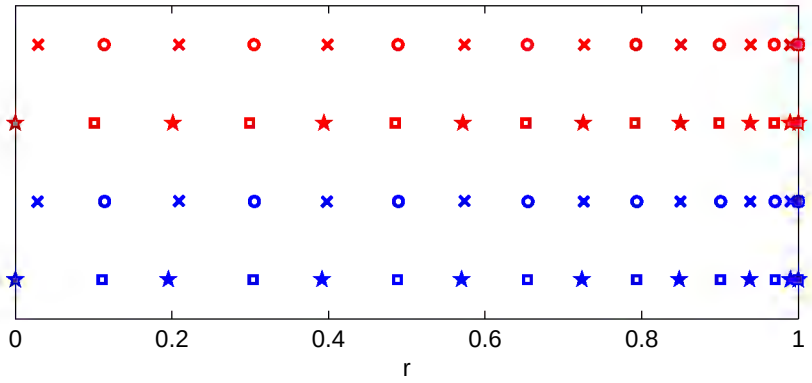

Figure 2.3: Radial optimal grids for different choices of averaging formulas and measurement operators ($n = 31$). Top two grids (red) correspond to $\mathcal{M}_n^*(\Lambda_1)$, bottom two grids (blue) correspond to $\mathcal{M}_n(\Lambda_1)$. Log-averaging formulas (2.56)–(2.57): primary $\times$, dual $\circ$. Averaging formulas (2.31)–(2.32): primary $\bigstar$, dual $\square$.

near the boundary of the unit disk $r = 1$, where the DtN map is measured. The gradual refinement towards the boundary accounts for the loss of resolution of the EIT problem inside the domain. These properties were observed in numerical experiments in [15, 44]. We prove them in below using the analytic expressions (2.52)–(2.53).

Lemma 2.4.1. *The optimal grid given by (2.52)–(2.53), (2.56)–(2.57) satisfies the interlacing conditions (2.27)–(2.28).*

Proof. Note, that the conductances (2.52)–(2.53) form a monotone interlacing sequence in the sense of

$$\left(\widehat{\gamma}_1^{(1)}\right) < \frac{1}{\gamma_1^{(1)}} < \widehat{\gamma}_2^{(1)} < \frac{1}{\gamma_2^{(1)}} < \ldots < \widehat{\gamma}_{m+1}^{(1)} < \frac{1}{\gamma_{m+1}^{(1)}}. \tag{2.58}$$

Summing (2.58) we can perform transformations

$$-h_\theta \sum_{s=1}^{j} \frac{1}{\gamma_s^{(1)}} > -h_\theta \sum_{s=1}^{j} \widehat{\gamma}_{s+1}^{(1)} > -h_\theta \sum_{s=1}^{j} \frac{1}{\gamma_{s+1}^{(1)}}, \tag{2.59}$$

$$-h_\theta \sum_{s=1}^{j} \frac{1}{\gamma_s^{(1)}} > -h_\theta \sum_{s=2}^{j+1} \widehat{\gamma}_s^{(1)} - h_\theta m_{1/2} \widehat{\gamma}_1^{(1)} > -h_\theta \sum_{s=2}^{j+1} \frac{1}{\gamma_s^{(1)}} - h_\theta m_{1/2} \widehat{\gamma}_1^{(1)}, \tag{2.60}$$

$$-h_\theta \sum_{s=1}^{j} \frac{1}{\gamma_s^{(1)}} > -h_\theta \sum_{s=2-m_{1/2}}^{j+1} \widehat{\gamma}_s^{(1)} > -h_\theta \sum_{s=2}^{j+1} \frac{1}{\gamma_s^{(1)}} - h_\theta \frac{1}{\gamma_1^{(1)}}, \tag{2.61}$$

which become after the exponentiation the interlacing condition

$$r_{j+1} > \widehat{r}_{j+2} > r_{j+2}. \tag{2.62}$$

□

An argument similar to the proof of lemma 2.4.1 can be used to show grid refinement property $\dfrac{r_j}{r_{j+1}} < \dfrac{r_{j+1}}{r_{j+2}}$.

Chapter 3

Partial data EIT with conformal and quasiconformal mappings

In this chapter we extend the inversion approach outlined in chapter 2 to the case of partial boundary measurements. The optimal grids introduced there for full boundary measurements are based on the rotational symmetry of the continuum problem for constant σ. For partial boundary measurements there is no rotational symmetry in the problem, so it is not immediately clear what class of grids should we look for, and how to construct them so that they have good approximation properties in some class of conductivity functions. Our main result in this chapter is that the grids can be constructed with an approach based on extremal quasiconformal mappings [77] that transform the problem with partial measurements to a problem with full boundary measurements. The results presented in this chapter were published in [18].

The chapter is organized as follows. We begin in section 3.1 with the study of the behavior of the EIT problem under the differentiable coordinate transformations, including conformal ones that preserve the isotropy of the conductivity. A more general class of quasiconformal mappings is discussed in section 3.2. We conclude the

chapter with section 3.3, where we present numerical results for both the conformal and the extremal quasiconformal mappings.

3.1 Coordinate transformations and the EIT

Let us consider how the circular resistor networks described in section 2.4 can be used in the case of partial boundary measurements. In particular, we would like to extend the reconstruction mapping $\mathcal{Q}_n(\Lambda_\gamma)$ to the partial data case. The other steps in the inversion method are the same as in the full boundary measurement case, as discussed in section 2.3. Here we focus our attention solely on $\mathcal{Q}_n(\Lambda_\gamma)$, for Λ_γ measured on the accessible boundary $\mathcal{B}_A \subset \mathcal{B}$.

The key idea is to map the partial data discrete EIT problem to the problem with measurements at equidistant points all around the boundary, where we already know how to define the optimal grids. Both problems are solved in $\mathbb{D}$, so we consider diffeomorphisms of the unit disk to itself.

Denote such a diffeomorphism by F and its inverse by G. If u solves (1.1), then $\widetilde{u}(x) = u(F(x))$ satisfies a similar equation with conductivity $\widetilde{\sigma}$ given by

$$\widetilde{\sigma}(x) = \left. \frac{G'(y)\sigma(y)\left(G'(y)\right)^T}{|\det G'(y)|} \right|_{y=F(x)}, \tag{3.1}$$

where G' denotes the Jacobian of G. The conductivity $\widetilde{\sigma}$ in (3.1) is the *push forward* of σ by G, and it is denoted by $G_*(\sigma)$. Note that if $G'(y)\left(G'(y)\right)^T \neq I$, then $\widetilde{\sigma}$ is a symmetric positive definite tensor provided $\det G'(y) \neq 0$. Thus, in general the push forward of an isotropic conductivity is anisotropic.

To write the transformed DtN map, we use the restrictions of diffeomorphisms G

and F to the boundary $g = G|_{\mathcal{B}}$ and $f = F|_{\mathcal{B}}$. Then, the push forward of the DtN map $g_*\Lambda_\sigma$ is

$$\left((g_*\Lambda_\sigma)\psi\right)(\theta) = \left(\Lambda_\sigma(\psi \circ g)\right)(\tau)|_{\tau=f(\theta)}\,, \quad \theta \in [0, 2\pi), \tag{3.2}$$

for $\psi \in H^{1/2}(\mathcal{B})$. As shown in [79], the DtN map is invariant under the push forward in the following sense

$$g_*\Lambda_\sigma = \Lambda_{G_*\sigma}. \tag{3.3}$$

This invariance tells us that given a diffeomorphism F, its boundary restriction $f = F|_{\mathcal{B}}$, their respective inverses G and g, and the DtN map Λ_σ, we can compute the push forward of the DtN map, solve the inverse problem for $g_*\Lambda_\sigma$ to obtain $\widetilde{\sigma}$, and then map it back using the inverse of (3.2). We will use the discrete analogue of this fact to transform the discrete measurements Λ_γ of Λ_σ on $\mathcal{B}_A$ to discrete measurements at the equidistant points θ_k, from which we can estimate $\widetilde{\sigma}$ with the method described in section 2.3.

Note however that the EIT problem is uniquely solvable only for isotropic conductivities. Anisotropic conductivities can be determined from the DtN map only up to a boundary-preserving diffeomorphism [79]. To overcome this ambiguity we propose two distinct approaches described in the next sections. The first approach is based on conformal mappings, which preserve the isotropy of the conductivity, at the expense of rigid placement of the measurement points in $\mathcal{B}_A$. The second approach uses extremal quasiconformal mappings, that minimize the artificial anisotropy of the reconstructed conductivity introduced by a general placement of the boundary measurement points in $\mathcal{B}_A$.

3.1.1 Conformal mappings and inversion grids

To ensure that the push forward (3.1) of the isotropic σ is isotropic itself, the mapping must satisfy $G'\left((G')^T\right) = I$ or, equivalently, $F'\left((F')^T\right) = I$. It means that F is *conformal* and the resulting conductivity is

$$G_*(\sigma) = \sigma \circ F. \tag{3.4}$$

Since all conformal mappings of the unit disk to itself belong to the family of Möbius transforms [58], F must be of the form

$$F(z) = e^{i\omega}\frac{z-a}{1-\overline{a}z}, \quad z \in \overline{\mathbb{D}},\ \omega \in [0, 2\pi),\ a \in \mathbb{C},\ |a| < 1, \tag{3.5}$$

where we associate $\mathbb{R}^2$ with the complex plane $\mathbb{C}$.

It remains to determine the constant parameters ω and a in (3.5). Let the accessible boundary $\mathcal{B}_A$ be the circular segment

$$\mathcal{B}_A = \left\{e^{i\tau} \mid \tau \in [-\beta, \beta]\right\}, \tag{3.6}$$

with $\beta \in (0, \pi)$. The inaccessible boundary is $\mathcal{B}_I = \mathcal{B}\backslash\mathcal{B}_A$. The restriction of (3.5) to $\mathcal{B}$ is denoted by

$$f(\theta) = F(e^{i\theta}). \tag{3.7}$$

It maps the boundary grid nodes θ_k, $\widehat{\theta}_k$ defined in section 2.4.2 to the transformed grid nodes τ_k, $\widehat{\tau}_k$ in $\mathcal{B}_A$, for $k = 1, \ldots, n$. We assume point-like measurements (χ_k have very small support), so that we can map any primary interval (θ_k, θ_{k+1}) to $\mathcal{B}_I$. Specifically, we take the interval $(\theta_{(n+1)/2}, \theta_{(n+3)/2})$ shown in figure 3.1. Let $\alpha = \pi(1 - 1/n)$, then

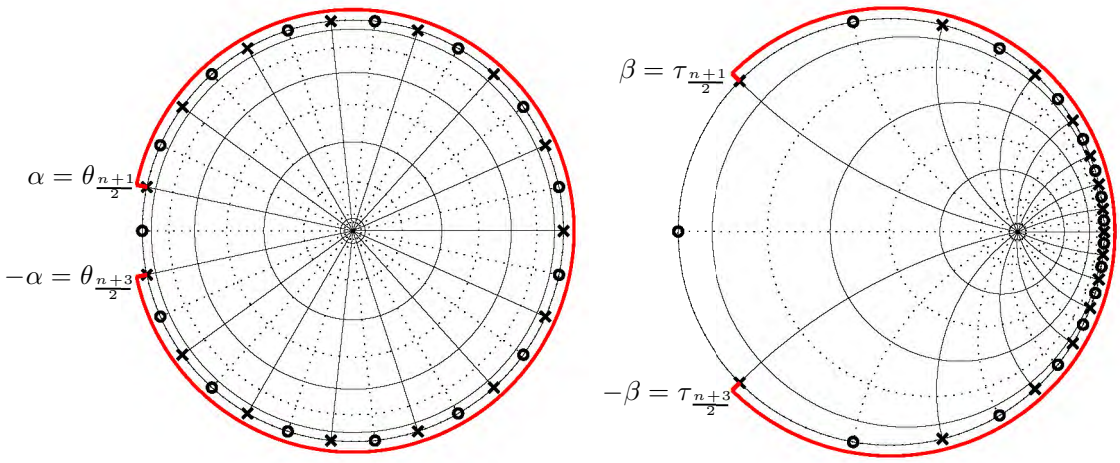

Figure 3.1: The optimal grid with $n = 15$ under the conformal mapping F, with $\beta = 3\pi/4$. Left: the optimal grid; right: the image of the optimal grid under F. Primary grid lines are solid black, dual grid lines are dotted black. Boundary grid nodes: primary $\times$, dual $\circ$. Accessible boundary is solid red.

the condition

$$f\left((\theta_{(n+1)/2}, \theta_{(n+3)/2})\right) = \mathcal{B}_I \tag{3.8}$$

becomes $F(e^{\pm i\alpha}) = e^{\pm i\beta}$ and the parameters of the Möbius transform are

$$a = \frac{\cos\alpha - \cos\beta}{1 - \cos(\alpha + \beta)}, \quad \omega = 0. \tag{3.9}$$

We show in figure 3.1 the transformation [1] of the optimal grid, which we name the *conformal mapping grid*. Note that by enforcing the condition (3.8), we have exhausted all degrees of freedom of the Möbius transform, and thus, we have no control over the placement of the boundary grid nodes τ_k, $\widehat{\tau}_k$. The resulting grid is refined towards the middle of the accessible boundary, and it is very sparse near the inaccessible boundary. This behavior persists as we increase the number n of primary boundary points, as we now explain.

[1] The grid is obtained with the log-averaging formulas and the measurement operator $\mathcal{M}_n^*$.

3.1.2 The limit distribution of boundary nodes in conformal mapping grids

To describe the asymptotic distribution of the boundary nodes under the conformal mappings, it is convenient to renumber τ_k, $\widehat{\tau}_k$. We define $\widetilde{\tau}_l = f(\pi + l\pi/n)$, $l = -n+1, \ldots, n$, so that when l is odd, $\widetilde{\tau}_l$ is a primary node and when l is even, it is a dual node. Then, we obtain after substituting (3.9) in (3.5), that

$$\cos\xi_l = \lim_{n\to\infty} \cos\widetilde{\tau}_l \;=\; \frac{l^2 - 1 + (l^2+1)\cos\beta}{l^2 + 1 + (l^2-1)\cos\beta}, \tag{3.10}$$

$$\sin\xi_l = \lim_{n\to\infty} \sin\widetilde{\tau}_l \;=\; \frac{2l\sin\beta}{l^2 + 1 + (l^2-1)\cos\beta}. \tag{3.11}$$

This limit distribution has a unique accumulation point at $\tau = 0$, as $l \to \infty$.

We illustrate the asymptotic behavior of the grid in figure 3.2. We observe that already for $n = 37$ the leftmost 13 nodes $\widetilde{\tau}_l$ are very close to their limit values ξ_l, $l = -6, \ldots, 6$. That is, as we increase n, there will be no further angular refinement of the grid in that region.

Note that as $n \to \infty$ and therefore $\alpha \to \pi$, the parameter a defined by (3.9) tends to -1. Thus, the only pole $1/\overline{a}$ of the Möbius transform (3.5) approaches $-1 \in \mathcal{B}$, and the mapping F degenerates in $\overline{\mathbb{D}}$.

The limiting behavior of the optimal grid under conformal automorphisms of $\mathbb{D}$ may suggest that the conformal mapping approach is not useful for solving the partial data EIT problem. After all, it is natural to expect the inversion grid to provide a converging scheme for the solution of the forward problem, for which grid refinement is a necessary condition. However, the instability of the EIT problem implies that we cannot improve the resolution of the reconstructions by simply taking more mea-

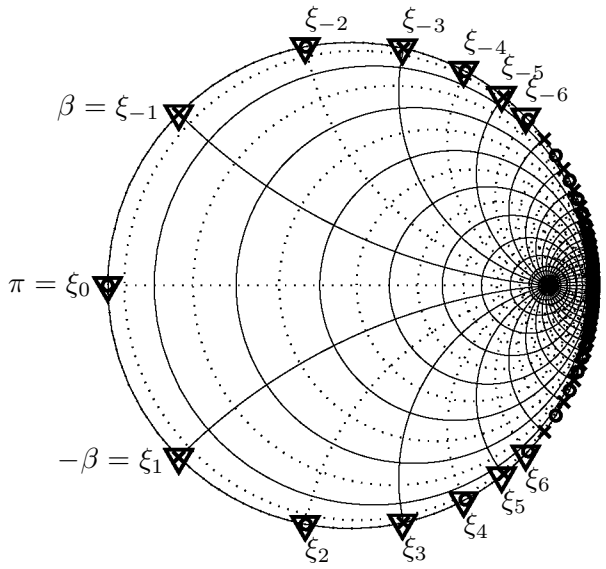

Figure 3.2: Limiting behavior ($n = 37$) of the image of the optimal grid under F, with $\beta = 3\pi/4$. Primary grid lines are solid, dual grid lines are dotted. Boundary grid nodes: primary τ_k are $\times$, dual $\widehat{\tau}_k$ are $\circ$. Limiting nodes $\xi_l = \lim_{n\to\infty} \widetilde{\tau}_l$ for $l = -6, \ldots, 6$ are $\bigtriangledown$.

surement points. Put otherwise, the limit $n \to \infty$ is not practically important in this problem. The numerical results in section 3.3 demonstrate that the conformal mapping approach gives reasonable reconstructions of the conductivity σ.

3.2 Quasiconformal mappings and anisotropy

So far we have identified two features of the conformal mapping grids, that may present problems for inversion. First, once the number of boundary grid nodes n and the size of the inaccessible boundary are fixed, we have no control over the positioning of the boundary grid nodes τ_k, where the measurements are made. Second, the grid does not refine asymptotically as $n \to \infty$. This is because the group of conformal automorphisms of the unit disk is too rigid. A more general approach would be to use a richer family of transforms at a price of introducing some anisotropy in the

reconstruction. A suitable family of mappings that allows the control of the artificial anisotropy of the reconstruction consists of *quasiconformal* mappings.

A quasiconformal mapping $W(z)$ is defined as a diffeomorphism that obeys the *Beltrami equation*

$$\frac{\partial W}{\partial \overline{z}} = \mu(z)\frac{\partial W}{\partial z}, \tag{3.12}$$

where the Beltrami coefficient $\mu(z)$ is a complex valued measurable function satisfying

$$\|\mu\|_\infty = \text{ess sup}|\mu(z)| < 1. \tag{3.13}$$

The Beltrami coefficient, also known as the *complex dilatation* $\mu(z)$ provides a measure of how much the mapping W differs from a conformal one. A conformal mapping corresponds to $\mu(z) \equiv 0$, in which case (3.12) reduces to the Cauchy-Riemann equation. Here we consider quasiconformal self mappings of the unit disk, so (3.12) and (3.13) hold for $z \in \mathbb{D}$.

Now let us describe the connection between the dilatation of the quasiconformal mapping and the anisotropy of the push-forward of an isotropic conductivity. Let $\widetilde{\sigma}(z)$ be an anisotropic conductivity with eigenvalues $\lambda_1(z) \geq \lambda_2(z) > 0$. Its *anisotropy* at z is defined by

$$\kappa(\widetilde{\sigma}, z) = \frac{\sqrt{L(z)} - 1}{\sqrt{L(z)} + 1}, \tag{3.14}$$

where $L(z) = \lambda_1(z)/\lambda_2(z)$, and

$$\kappa(\widetilde{\sigma}) = \sup_z \kappa(\widetilde{\sigma}, z) \tag{3.15}$$

is the maximum anisotropy. The relation between the Beltrami coefficient of a quasiconformal mapping and the anisotropy of the push forward of an isotropic conduc-

tivity by the mapping is given by the following result. [2]

Lemma 3.2.1. *Let $W(x,y) = [u(x,y), v(x,y)]^T$ be a quasi-conformal diffeomorphism, with the complex form $W(z) = u(z) + iv(z)$, $z = x + iy$, and the Beltrami coefficient $\mu(z)$. If σ is an isotropic conductivity, then*

$$\kappa(W_*(\sigma), z) = |\mu(z)|. \tag{3.16}$$

Proof. Since only the ratio of the eigenvalues L matters for determining the anisotropy, we can consider only the part $H = W'(W')^T$ of the definition of the push forward.

$$W' = \begin{bmatrix} u_x & u_y \\ v_x & v_y \end{bmatrix}, \quad H = \begin{bmatrix} u_x^2 + u_y^2 & u_x v_x + u_y v_y \\ u_x v_x + u_y v_y & v_x^2 + v_y^2 \end{bmatrix}. \tag{3.17}$$

The eigenvalues λ_1, λ_2 of H satisfy

$$\lambda_1 + \lambda_2 = \mathrm{Tr} H = u_x^2 + u_y^2 + v_x^2 + v_y^2, \tag{3.18}$$

$$\lambda_1 \lambda_2 = \det H = (\det W')^2 = (u_x v_y - u_y v_x)^2. \tag{3.19}$$

From (3.12) and the definition of complex derivatives $\dfrac{\partial}{\partial \bar{z}} = \dfrac{1}{2}\left(\dfrac{\partial}{\partial x} + i\dfrac{\partial}{\partial y}\right)$, $\dfrac{\partial}{\partial z} = \dfrac{1}{2}\left(\dfrac{\partial}{\partial x} - i\dfrac{\partial}{\partial y}\right)$ we derive

$$\mu = \frac{\frac{\partial W}{\partial z}}{\frac{\partial W}{\partial \bar{z}}} = \frac{(u_x + v_y) + i(v_x - u_y)}{(u_x - v_y) + i(v_x + u_y)}, \tag{3.20}$$

so that

$$|\mu| = \sqrt{\frac{u_x^2 + u_y^2 + v_x^2 + v_y^2 + 2(u_x v_y - u_y v_x)}{u_x^2 + u_y^2 + v_x^2 + v_y^2 - 2(u_x v_y - u_y v_x)}}. \tag{3.21}$$

[2] This result is probably known, but we could not find a proof in the literature.

Comparing (3.21) to (3.18) and (3.19) we can write

$$|\mu| = \sqrt{\frac{\lambda_1+\lambda_2+2\sqrt{\lambda_1\lambda_2}}{\lambda_1+\lambda_2-2\sqrt{\lambda_1\lambda_2}}} = \sqrt{\frac{(\sqrt{\lambda_1}+\sqrt{\lambda_2})^2}{(\sqrt{\lambda_1}-\sqrt{\lambda_2})^2}} \tag{3.22}$$

$$= \frac{\sqrt{\lambda_1}+\sqrt{\lambda_2}}{\sqrt{\lambda_1}-\sqrt{\lambda_2}} = \frac{\sqrt{\frac{\lambda_1}{\lambda_2}}+1}{\sqrt{\frac{\lambda_1}{\lambda_2}}-1} = \frac{\sqrt{L}-1}{\sqrt{L}+1}, \tag{3.23}$$

which completes the proof. □

It follows immediately that the L^∞ norm of the dilatation gives us a measure of the maximum anisotropy introduced by W to an isotropic conductivity

$$\kappa\left(W_*(\sigma)\right) = \|\mu\|_\infty. \tag{3.24}$$

Since the true unknown conductivity is isotropic, we would like to minimize the amount of anisotropy introduced into the reconstruction by the mapping W. This leads us to the *extremal* quasiconformal mappings, which minimize the maximum anisotropy $\|\mu\|_\infty$ under some constraints. In our case the constraints come in the form of prescribing the boundary value $f = W|_{\mathcal{B}}$, which gives us control over the positioning of the measurement points $\tau_k = f(\theta_k)$.

3.2.1 Extremal quasiconformal mappings

It is known [77] that for sufficiently regular boundary values, there exists a unique extremal quasiconformal mapping that is a Teichmüller mapping, i.e. its Beltrami coefficient satisfies

$$\mu(z) = \|\mu\|_\infty \frac{\overline{\phi(z)}}{|\phi(z)|}, \tag{3.25}$$

for some holomorphic function $\phi(z)$ in $\mathbb{D}$. Using this in (3.16), we obtain that the push forward of an isotropic conductivity by a Teichmüller mapping has a uniform anisotropy throughout $\mathbb{D}$.

Similar to (3.25), we can define the dilatation of W^{-1} in terms of a holomorphic function ψ. Then, according to [71], we can decompose a Teichmüller mapping W into

$$W = \Psi^{-1} \circ A_K \circ \Phi, \tag{3.26}$$

where

$$\Phi(z) = \int \sqrt{\phi(z)}dz, \qquad \Psi(\zeta) = \int \sqrt{\psi(\zeta)}d\zeta, \tag{3.27}$$

and A_K is affine. The mappings Φ and Ψ are conformal away from zeros of ϕ and ψ respectively. The only source of anisotropy in decomposition (3.26) is the affine mapping A_K, that we take to be

$$A_K(x + iy) = Kx + iy, \quad x, y \in \mathbb{R}, \tag{3.28}$$

where the constant parameter $K > 0$ determines the anisotropy

$$\kappa\left(W_*(\sigma)\right) = \|\mu\|_\infty = \left|\frac{K-1}{K+1}\right|. \tag{3.29}$$

To obtain the terms Φ and Ψ in the decomposition (3.26) of the Teichmüller mapping, we use the constraints on the boundary values $f = W|_{\mathcal{B}}$. Since we work with point-like boundary measurements, it is only important to have control over the behavior of the Teichmüller mapping at the measurement points $e^{i\theta_k}$. This leads us to consider the extremal polygonal quasiconformal mappings. A *polygon* in this context is a unit disk $\mathbb{D}$ with n distinguished points on $\mathcal{B}$, called the *vertices* of the polygon

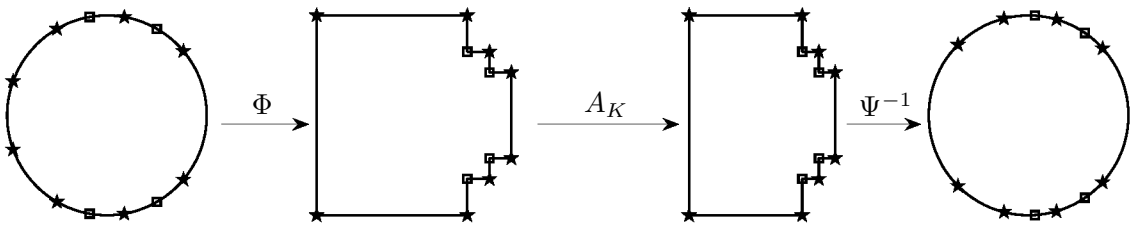

Figure 3.3: Teichmüller mapping decomposed into conformal mappings Φ and Ψ, and an affine transform A_K, $K = 3/4$. The poles of ϕ and ψ and their images under Φ and Ψ are ★, the zeros of ϕ and ψ and their images under Φ and Ψ are □.

(in our case $e^{i\theta_k}$).

The extremal polygonal quasiconformal mapping W takes the boundary points $e^{i\theta_k}$ to prescribed points $e^{i\tau_k}$, while minimizing the maximum dilatation. According to [78], the integrals Φ and Ψ in its decomposition map the unit disk conformally onto polygons comprised of a number of rectangular strips. But conformal mappings of the unit disk to polygons are Schwartz-Christoffel mappings [34], given by the general formula

$$S(z) = a + b \int^{z} \prod_{q=1}^{N} \left(1 - \frac{\zeta}{z_q}\right)^{\alpha_q - 1} d\zeta, \tag{3.30}$$

where $a, b \in \mathbb{C}$ are constants, N is the number of vertices of a polygon, $z_q \in \mathcal{B}$ are the pre-images of the vertices and $\pi\alpha_q$ are the interior angles of the polygon. Moreover, for the polygons comprised of rectangular strips $\alpha_q \in \{1/2, 3/2\}$.

Comparing the definitions (3.27) of Φ and Ψ with (3.30) we observe that ϕ and ψ are rational functions with first order poles at vertices with angle $\pi/2$ and first order zeros at vertices with angle $3\pi/2$. This behavior is illustrated in detail in figure 3.3, along with the behavior of each mapping in the decomposition (3.26). Note that we construct the mappings Φ, Ψ so that they are symmetric with respect to the real axis. This is done to maintain the symmetry of the optimal grid under W.

We have established that in order to map the unit disk to a polygon comprised

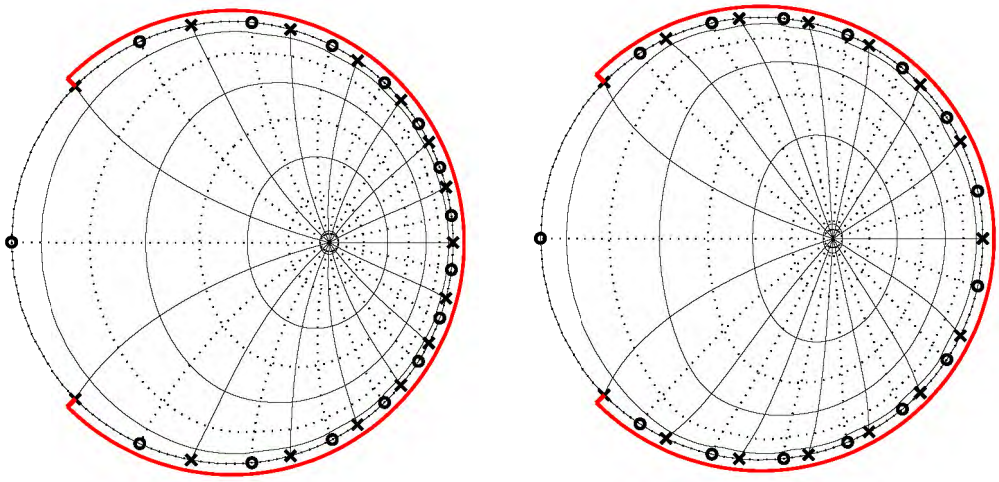

Figure 3.4: The optimal grid with $n = 15$ under the quasiconformal Teichmüller mappings W with different K. Left: $K = 0.8$; right: $K = 0.66$. Primary grid lines are solid black, dual grid lines are dotted black. Boundary grid nodes: primary $\times$, dual $\circ$. Accessible boundary is solid red.

of several rectangular strips it is necessary for ϕ and ψ to have zeros and poles on $\mathcal{B}$. In what follows we construct ϕ and ψ so that the zeros are at the dual grid nodes and the poles are at the primary grid nodes. Such construction gives us an extremal mapping, since according to [71], every Teichmüller mapping of the form (3.26) is extremal for the boundary values that it induces.

3.2.2 Teichmüller mappings and inversion grids

We illustrate the behavior of the optimal grids under the extremal quasiconformal mappings in figure 3.4. The number n of boundary primary grid nodes and the size of the accessible boundary are the same as for the conformal mapping example in figure 3.1, so that we can compare the two approaches. Similar to the conformal mapping case, we map the primary boundary grid interval $(\theta_{(n+1)/2}, \theta_{(n+3)/2})$ to the inaccessible boundary.

The grids for two different values of the affine stretching constant K are presented

in figure 3.4, with the larger value of K corresponding to less artificial anisotropy. For $K = 0.8$ we already observe that the clustering of the boundary grid nodes around 1 is much less pronounced then for the conformal mapping grid. As we decrease K to 0.66 the grid nodes move further away from the middle of $\mathcal{B}_A$ towards the inaccessible boundary. One should keep in mind that although the distribution of the grid nodes becomes more uniform for smaller values of K, the conductivity reconstructed on such grid would have a larger amount of artificial anisotropy, as shown in the numerical examples in the next section.

3.3 Numerical results

In this section we present numerical results for the reconstructions of smooth and piecewise constant conductivities. We begin in section 3.3.1 with the outline of the inversion method. Then, we describe our numerical implementation of the inversion method in section 3.3.2. The numerical results are in sections 3.3.3 and 3.3.4.

3.3.1 The inversion method

What we mean by inversion method, is the computation of the reconstruction $\mathcal{Q}_n(\Lambda_\gamma)$ from the discrete measurements $\Lambda_\gamma = \mathcal{M}_n(\Lambda_\sigma)$ made at the accessible boundary $\mathcal{B}_A$. This reconstruction can be viewed as an image of the unknown conductivity σ, as we show below with numerical simulations. The computation of the reconstruction is summarized in the algorithm below.

Algorithm 3.3.1. *To compute the reconstruction* $\sigma^\star = \mathcal{Q}_n\left(\mathcal{M}_n(\Lambda_\sigma)\right)$ *perform the following steps:*

(1) Compute the discrete DtN maps $\Lambda_\gamma = \mathcal{M}_n(\Lambda_\sigma)$ *and* $\Lambda_{\gamma^{(1)}} = \mathcal{M}_n(\Lambda_1)$ *using the*

measurement operator $\mathcal{M}_n$ defined in section 2.2.3. This implies choosing the odd number n of boundary measurements and the distribution of measurement points $e^{i\tau_k} \in \mathcal{B}_A$, for $k = 1, \ldots, n$.

(2) Solve the discrete EIT problem for the circular resistor network with discrete DtN map Λ_γ computed at step 1. This gives the conductances $\gamma_{j,k}$ and $\widehat{\gamma}_{j,k}$ of the resistors.

(3) Solve the discrete EIT problem for the circular resistor network with DtN map $\Lambda_{\gamma^{(1)}}$ computed at step 1, for the uniform conductivity $\sigma^{(1)} \equiv 1$. This gives the conductances $\gamma^{(1)}_{j,k}$ and $\widehat{\gamma}^{(1)}_{j,k}$.

(4) Compute the extremal quasiconformal mapping T that takes the uniformly distributed points $e^{i\theta_k} \in \mathcal{B}$ to the measurement points $e^{i\tau_k} \in \mathcal{B}_A$,

$$e^{i\tau_k} = T(e^{i\theta_k}), \qquad k = 1, \ldots, n. \tag{3.31}$$

Use this mapping to compute the grid nodes $T(\widehat{r}_j e^{i\theta_k})$ and $T(r_j e^{i\widehat{\theta}_k})$, where r_j, $\widehat{r}_j$ are the radii of the rotationally symmetric optimal grid, and $\theta_k = 2\pi(k-1)/n$, $\widehat{\theta}_k = 2\pi(k-1/2)/n$ are the equidistant angular grid nodes. In the particular case of τ_k distributed as in section 3.1.1, the mapping T is a conformal one.

(5) The reconstruction

$$\sigma^\star = \mathcal{Q}_n\left[\mathcal{M}_n(\Lambda_\sigma)\right] \in \mathcal{S} \tag{3.32}$$

is given by the piecewise linear interpolation of the following values at the trans-

formed grid nodes

$$\sigma^\star\left(T(\widehat{r}_{j+m_{1/2}}e^{i\theta_k})\right) = \gamma_{j,k}/\gamma^{(1)}_{j,k}, \quad j=1,\ldots,m+1, \tag{3.33}$$

$$\sigma^\star\left(T(r_j e^{i\widehat{\theta}_k})\right) = \widehat{\gamma}_{j,k}/\widehat{\gamma}^{(1)}_{j,k}, \quad j=2-m_{1/2},\ldots,m+1, \tag{3.34}$$

where k=1,. . . ,n.

3.3.2 Numerical implementation

In step 1 of the inversion algorithm we choose the number n of boundary nodes. The choice of n is studied in [15, 44], and it is related to the amount of noise present in the measured data. Recall that the theory of discrete inverse problems for networks with circular planar graphs described in section 2.4.1 provides an exact relation between the number of boundary nodes and the number of layers of a uniquely recoverable network. The discrete EIT problem is exponentially ill-conditioned, loosing roughly one digit of accuracy for each layer recovered. Hence the number of layers that can be stably recovered is limited by the noise level in the data, thus limiting n. A simple heuristic was proposed in [15, 44] to determine n by solving a sequence of discrete inverse problems for increasing n, until the layer peeling method [26] fails to produce positive conductances. In the numerical examples below $n = 21$ ($m = 4$, $m_{1/2} = 1$), and it is well below the heuristic limit, which guarantees a stable solution of the discrete inverse problem.

We use measurement functions χ_k with small supports, so the size of the inaccessible boundary is slightly smaller than the image of the primary grid cell $\left(\theta_{(n+1)/2}, \theta_{(n+3)/2}\right)$ that is mapped to $\mathcal{B}_I$ according to (3.8). We take $\chi_k(\theta)$ as the indicator functions of intervals centered around the primary boundary grid nodes $e^{i\theta_k}$ and occupying 10% of the corresponding dual boundary grid interval. They are transformed to

$\widetilde{\chi}_k(\tau) = \chi_k(g(\tau))$ by the boundary restriction g of the inverse of T. We indicate with small red squares the end points of the supports of $\widetilde{\chi}_k(\tau)$ in figures 3.6–3.10. Note that the measurements $\mathcal{M}_n(\Lambda_1)$ and $\mathcal{M}_n(\Lambda_\sigma)$ in steps 2 and 3 of the algorithm are computed using transformed functions $\widetilde{\chi}_k(\tau)$. The continuum DtN maps Λ_1 and Λ_σ are approximated with a finite difference scheme on a fine tensor product grid with 300 uniformly spaced nodes in angle and 100 uniformly spaced nodes in radius.

We solve the discrete inverse problems in steps 2 and 3 of the algorithm using the layer peeling method introduced in [26]. Being a direct method, the layer peeling is extremely fast, which makes our inversion algorithm computationally inexpensive. In fact, recovering all conductances in a network with layer peeling is faster than computing the Jacobian of the discrete DtN map with respect to the conductances. Thus, the layer peeling recovers the whole network faster than one iteration of any gradient-based optimization method, which may take hundreds of iterations to converge considering the ill-conditioning of the problem.

Note that since the transformed measurement functions $\widetilde{\chi}_k(\tau)$ are not rotationally symmetric in the sense of (2.26), the conductances $\gamma^{(1)}_{j,k}$ and $\widehat{\gamma}^{(1)}_{j,k}$ obtained in step 3 depend on the angular index k, even though the conductivity $\sigma^{(1)} \equiv 1$ is rotationally invariant.

The Teichmüller mapping T in step 4 is computed using the decomposition (3.26) for a fixed value of the affine stretching constant K. Choosing K is a tradeoff between the resolution and the distortion of the reconstruction, as shown in the numerical examples below. The conformal mappings Φ and Ψ in decomposition (3.26) are computed numerically using the Schwartz-Christoffel toolbox [33]. In case $K = 1$ the mapping T is conformal, so we can use (3.5), with the parameters given by (3.9) to obtain $T = F$.

Recall from the numerical results in section 2.4.5 that the optimal grid depends

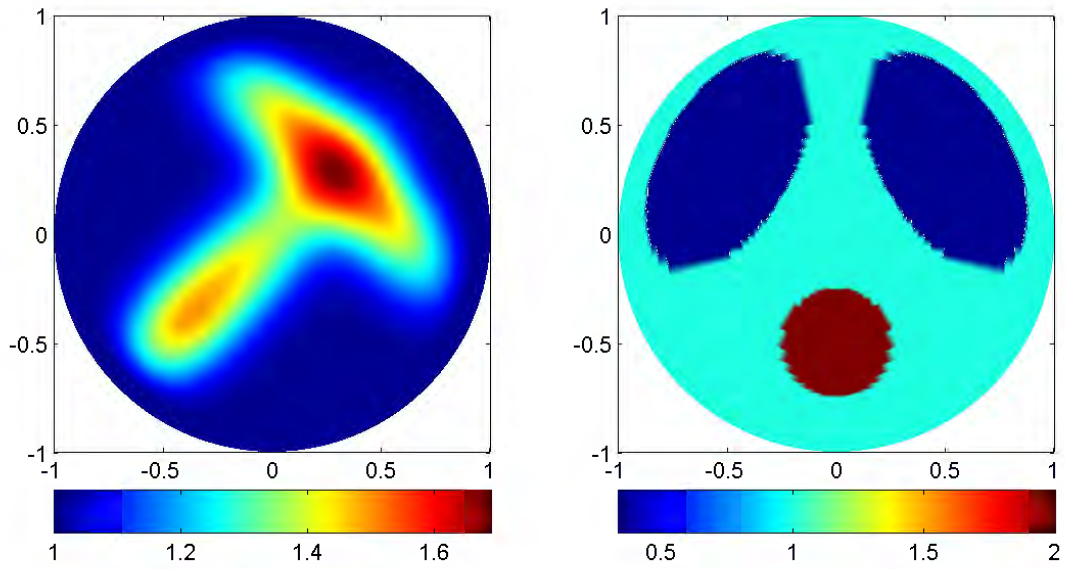

Figure 3.5: The conductivities used in the numerical experiments. Left: smooth conductivity *sigX*; right: piecewise constant chest phantom *phantom1*.

weakly on the choice of averaging formulas and of the measurement operator. In all the numerical results presented below, we use the radii r_j, $\widehat{r}_j$ that correspond to log-averaging formulas and the measurement operator $\mathcal{M}_n^*$, for which these radii are computed exactly.

To compare the reconstructions for partial measurements with those for full boundary measurements, we present numerical results for the same conductivity functions considered in [15, 44]. They are shown in figure 3.5. The first one is a smooth conductivity (*sigX*), given by the superposition of two Gaussians. The second one is piecewise constant (*phantom1*), and it models a chest phantom [67].

It appears from the examples of optimal grids in figures 3.1 and 3.4, that the reconstructions will have better resolution near the accessible boundary. To explore this phenomenon, we rotate the accessible boundary (and therefore the grid) by ω_0 to move the high resolution region around the domain. Note that both *sigX* and

*phantom*1 have axes of symmetry. We specifically choose ω_0 so that the axis of symmetry of the grid $z = te^{i\omega_0}$, $t \in \mathbb{R}$, is neither collinear with nor orthogonal to the axis of symmetry of σ.

For each reconstruction we compute the pointwise relative error for every $z \in \mathbb{D}$ using the formula

$$E(z) = \left| \frac{\sigma^\star(z)}{\sigma(z)} - 1 \right|. \tag{3.35}$$

The mean relative error is

$$[E] = \frac{\int_H E(z)dz}{\int_H dz} \cdot 100\%, \tag{3.36}$$

where H is the convex hull of the optimal grid nodes, where the reconstruction $\sigma^\star(z)$ is defined. We give $[E]$ in the top right corner of every reconstruction plot.

3.3.3 Reconstructions of smooth conductivity

We begin with reconstructions of the smooth conductivity *sigX*. In figure 3.6 we show reconstructions for two different values of ω_0, which demonstrate how the resolution of our method depends on the relative position of the accessible boundary and the features of the conductivity. We refer to the two distinct features of the hammer-like conductivity *sigX* as the "head" and the "handle".

For $\omega_0 = 3\pi/10$ the region of high resolution is close to the head feature for both the conformal and quasiconformal mapping reconstructions. As expected, the conformal mapping reconstruction looses quickly resolution away from the middle of the accessible boundary. The quasiconformal reconstruction has a more uniform resolution throughout the domain. However, we observe that the quasiconformal reconstruction is somewhat distorted compared to the true conductivity, which is

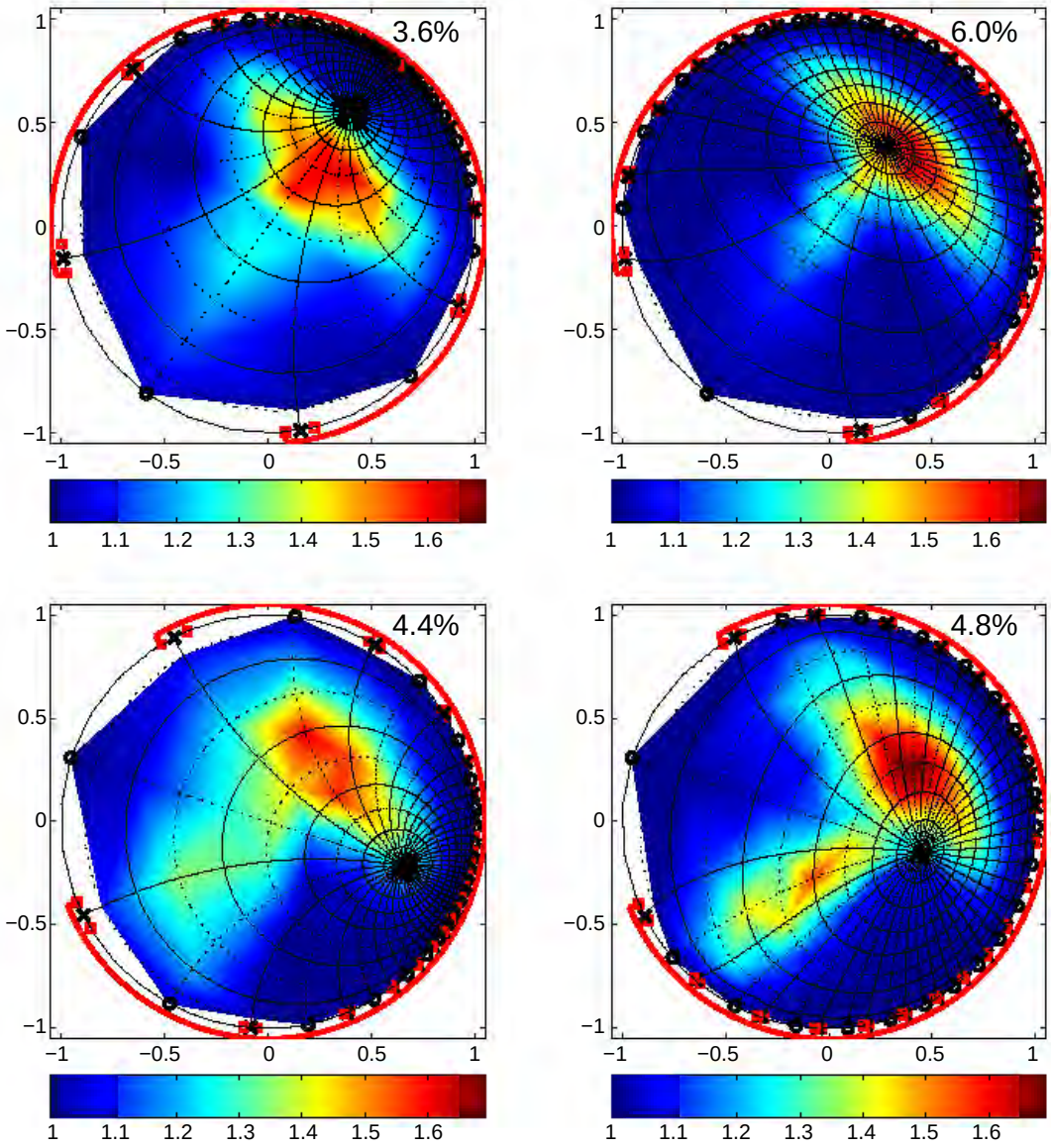

Figure 3.6: Reconstructions of the smooth conductivity *sigX*, $\beta = 3\pi/4$, $n = 21$. Top row: $\omega_0 = 3\pi/10$; bottom row: $\omega_0 = -\pi/10$. Left column: conformal mapping; right column: quasiconformal mapping, $K = 0.7$. $\mathcal{B}_A$ is solid red. Percentages: mean relative errors $[E]$.

the reason why it has a slightly larger mean relative error. We believe that this is a manifestation of the artificial anisotropy that is implicitly introduced by the quasiconformal mapping. Such distortions are observed for all reconstructions that

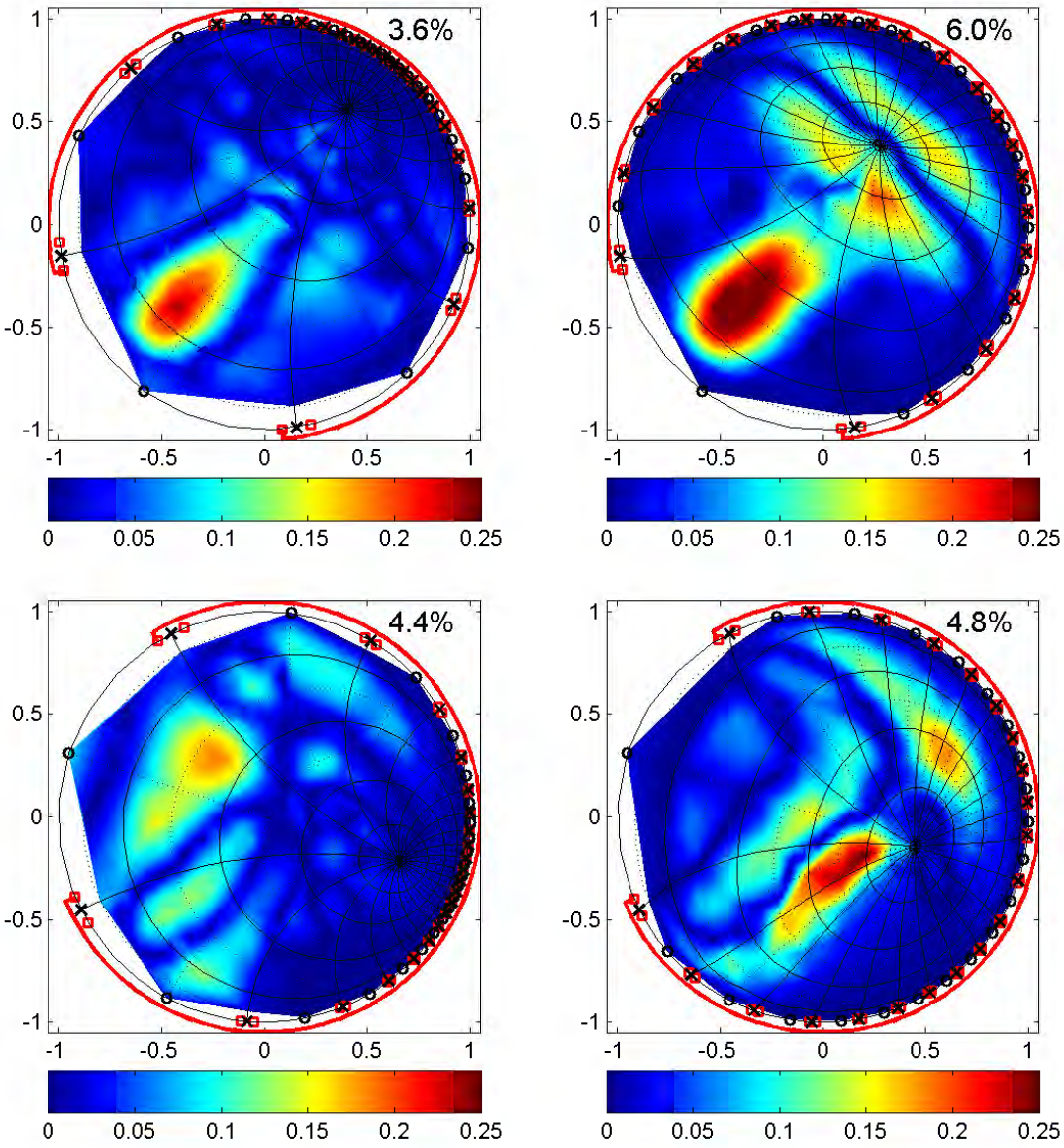

Figure 3.7: Pointwise relative error $E(z)$ for the reconstructions of the smooth conductivity *sigX* given in figure 3.6. Percentages: mean relative errors $[E]$.

we consider, both for the smooth and piecewise constant conductivities.

In the case $\omega_0 = -\pi/10$ the difference between the conformal and the quasi-conformal reconstructions becomes more pronounced. The middle of the accessible boundary is away from both features of the conductivity, so the conformal mapping

reconstruction is very coarse. The quasiconformal mapping reconstruction captures both features much better. However, similar to the case $\omega_0 = 3\pi/10$, we observe some distortion in the reconstruction, especially where the handle is connected to the head, which leads to a larger relative error compared to the conformal case.

The distribution of the relative error throughout $\mathbb{D}$ for all four reconstructions of the smooth conductivity *sigX* is given in figure 3.7. As expected, in the conformal case the error is small close to the middle of $\mathcal{B}_A$. The error in the quasiconformal case is concentrated around the features of the conductivity, which shows that the main source of error is the distortion.

3.3.4 Reconstructions of piecewise constant conductivity

Let us now consider the reconstructions of the piecewise constant chest phantom. Unlike in the smooth conductivity case, we study the behavior of the reconstructions not only for different values of ω_0, but also for different choices of β. We refer to the low and high conductivity features of the phantom as the "lungs" and the "heart" respectively.

We show in figure 3.8 the reconstructions for $\omega_0 = -\pi/10$, and two sizes of the accessible boundary corresponding to $\beta = 4\pi/3$ and $\beta = 2\pi/3$, respectively. The middle of the accessible boundary is located close to the bottom of the right lung, and so the conformal mapping reconstruction captures the right lung quite well. However, the left lung is basically indistinguishable, and both the position and the conductivity value of the heart are captured poorly. The quasiconformal mapping reconstruction does a better job of imaging both the right lung and the heart, and even the left lung can be distinguished as a separate feature. This behavior becomes more pronounced as the accessible boundary is shrunk further.

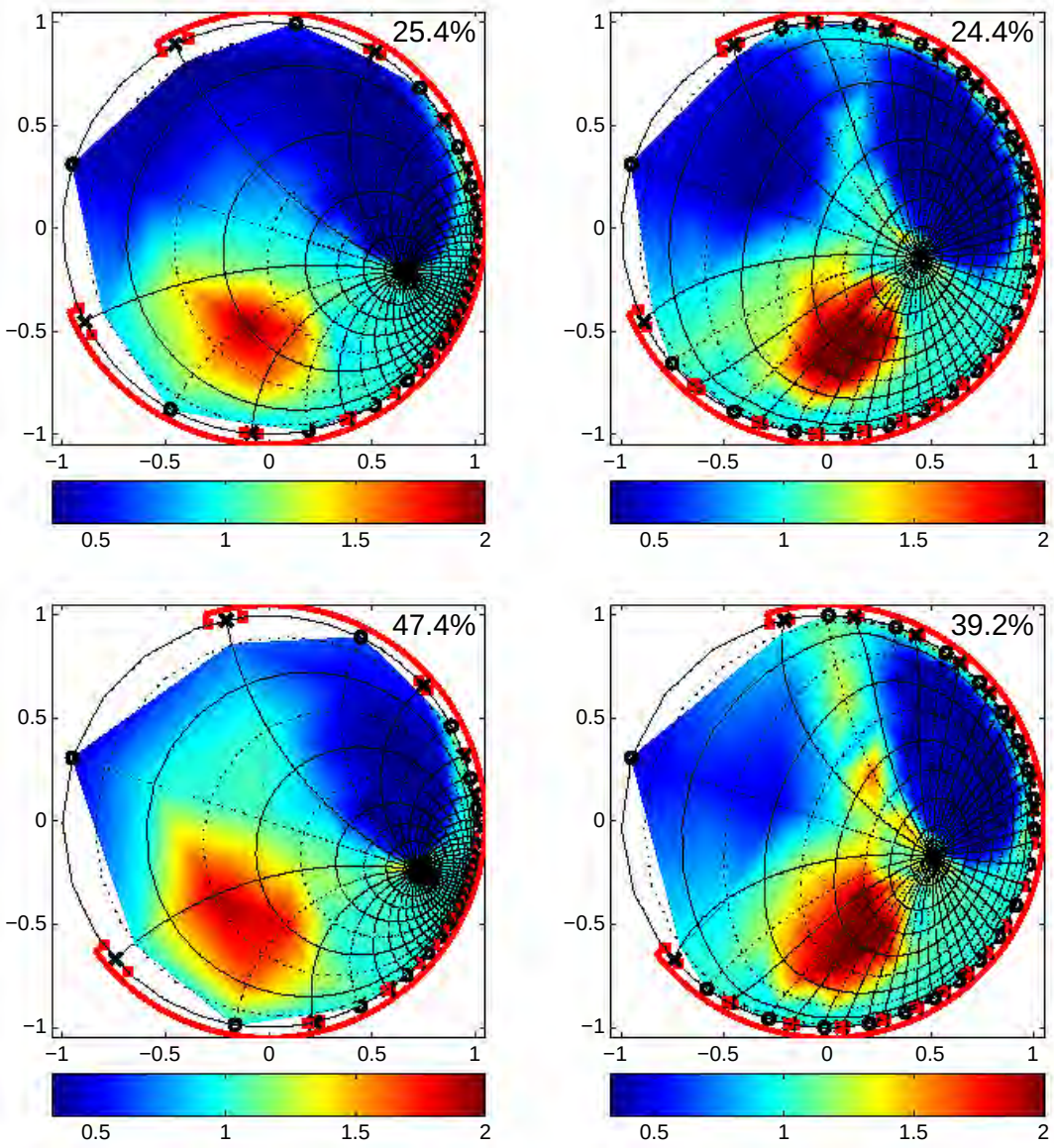

Figure 3.8: Reconstructions of piecewise constant conductivity *phantom1*, $\omega_0 = -\pi/10$, $n = 21$. Top row: $\beta = 3\pi/4$, $K = 0.7$; bottom row: $\beta = 2\pi/3$, $K = 0.63$. Left column: conformal mapping; right column: quasiconformal mapping. $\mathcal{B}_A$ is solid red. Percentages: mean relative errors $[E]$.

The choice of ω_0 in figures 3.9 and 3.10 allows us to focus the reconstruction on the lungs and the heart respectively. We notice again that the conformal mapping reconstruction captures the geometry and the magnitude of the conductivity features

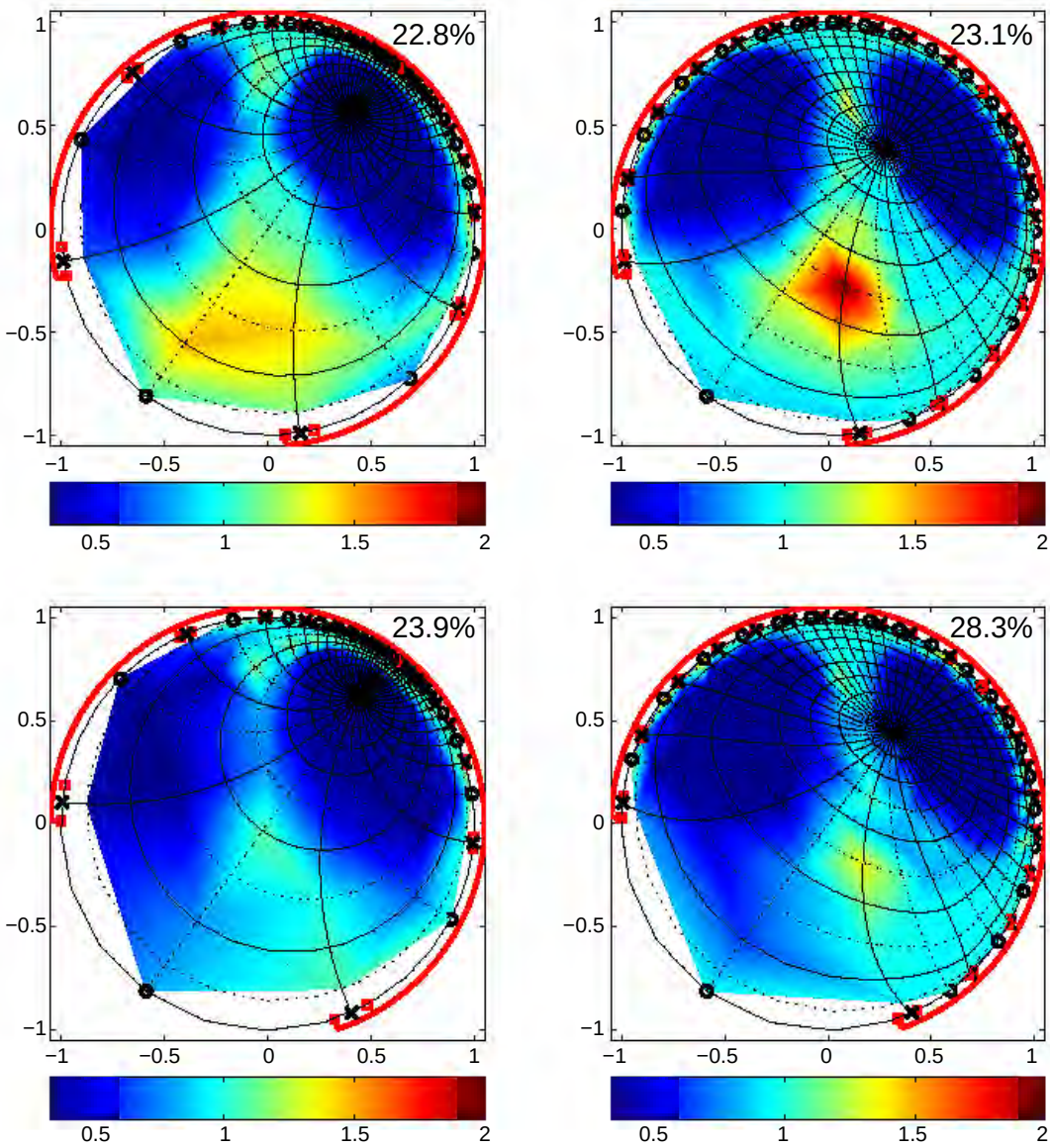

Figure 3.9: Reconstructions of piecewise constant conductivity *phantom1*, $\omega_0 = 3\pi/10$, $n = 21$. Top row: $\beta = 3\pi/4$, $K = 0.7$; bottom row: $\beta = 2\pi/3$, $K = 0.63$. Left column: conformal mapping; right column: quasiconformal mapping. $\mathcal{B}_A$ is solid red. Percentages: mean relative errors $[E]$.

in its high resolution region very well. None of the two approaches has a clear advantage over the other in terms of the relative error. Overall, the relative errors are higher for the reconstructions of the piecewise constant chest phantom than those for

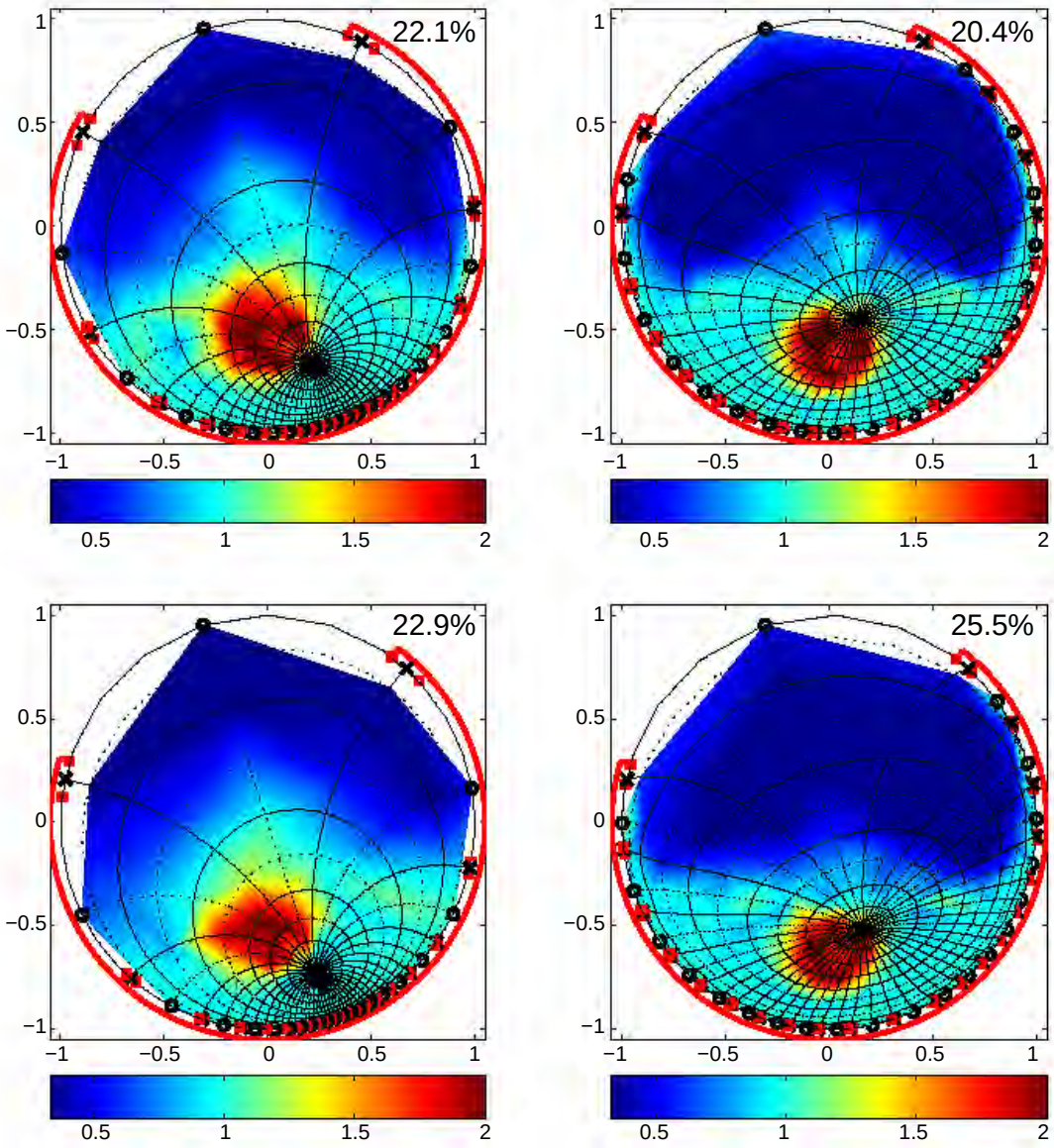

Figure 3.10: Reconstructions of piecewise constant conductivity *phantom1*, $\omega_0 = -2\pi/5$, $n = 21$. Top row: $\beta = 3\pi/4$, $K = 0.7$; bottom row: $\beta = 2\pi/3$, $K = 0.63$. Left column: conformal mapping; right column: quasiconformal mapping. $\mathcal{B}_A$ is solid red. Percentages: mean relative errors $[E]$.

the smooth conductivity reconstruction. This is in part due to a behavior similar to Gibbs phenomenon, which can be clearly observed in the quasiconformal reconstruction with $\beta = 2\pi/3, K = 0.63$ in figure 3.8. It manifests itself as a couple of spurious

oscillations to the left from the right lung.

We can now conclude that both the conformal and quasiconformal approaches can be useful in different situations. If we have some a priori information on where the features of interest of the conductivity may be located, and if we have enough control over where the DtN map is measured, we can lump the measurements at the points prescribed by a conformal mapping, choosing the middle of the accessible boundary close to the suspected location of the features of interest. When no a priori information is available, or the accessible boundary is small, the quasiconformal approach is superior to the conformal one, because it has a better resolution throughout the domain.

Chapter 4

Partial data EIT with pyramidal networks and sensitivity grids

Even with the use of conformal and quasiconformal mappings, the construction of the optimal grids in chapter 3 remains essentially one dimensional, since it reduces the problem to the full data setting, where the optimal grid is tensor product.

The numerical experiments in section 3.3 show a trade-off between having undistorted images and resolution distributed throughout Ω. To eliminate distortions, the transformed conductivity should remain isotropic, which means that the coordinate transformation must be conformal. However, the resulting grids have poor refinement properties, with node accumulation in the vicinity of the center of $\mathcal{B}_A$, and very poor resolution of the images in the remainder of Ω. The conformal mappings also require a rigid placement of the measurement points on $\mathcal{B}_A$. The extremal quasiconformal grids achieve a more uniform resolution in Ω, and allow the arbitrary placement of the measurement points on $\mathcal{B}_A$. However, they induce artifacts in the images because the transformed conductivity is anisotropic.

In this chapter we propose to use instead networks with *pyramidal* graphs that can

be embedded in Ω, while keeping the boundary points in $\mathcal{B}_A$.We do so by introducing the truly two dimensional optimal *sensitivity grids*, that are based on the sensitivity analysis of both the continuum and the discrete EIT problems. The results presented in this chapter were published in [19].

The chapter is organized as follows. In section 4.1 we present the theory of inverse problems for pyramidal networks. The sensitivity grids are introduced in section 4.2. We conclude the chapter with the numerical experiments in section 4.3.

4.1 The inverse problem for pyramidal networks

Unlike the networks with circular topology, for which the layer peeling algorithm was developed in [26], no such algorithm is to be found in the literature for the pyramidal networks. We show that these networks are indeed recoverable in section 4.1.1, and in section 4.1.2 we develop a layer peeling algorithm.

4.1.1 Criticality of pyramidal networks

The pyramidal networks are also known in the literature under the name *standard*, since they can be chosen to be the representatives of certain classes of networks equivalent under $Y - \Delta$ transformations [27]. Keeping the same notation as in the previous chapters, we denote the graphs of the pyramidal networks with n boundary nodes by Γ_n, and illustrate how they look in figure 4.1, for even and odd n. Hereafter, we refer to the edges of the graphs as "vertical" or "horizontal" according to their orientation in figure 4.1.

To use the pyramidal networks for inversion, we need to establish that they are uniquely recoverable from the DtN map, which is equivalent to showing that the graphs Γ_n are critical. It is mentioned in [27, Proposition 7.3], without proof, that

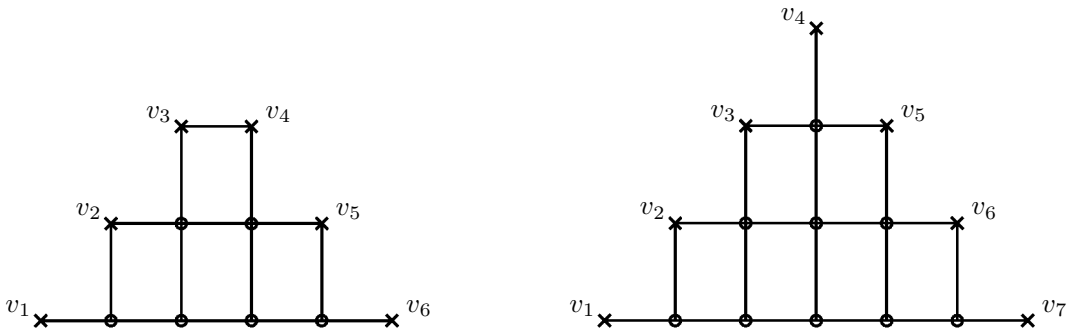

Figure 4.1: Pyramidal (standard) graphs Γ_n. Left: $n = 6$; right: $n = 7$. Boundary nodes v_j, $j = 1, \ldots, n$ are $\times$, interior nodes are $\circ$.

the networks Γ_n, $n \geq 2$ are critical. Below we give the proof for the case of even n. The extension of the proof to odd n is straightforward.

Lemma 4.1.1. *Pyramidal networks with graphs Γ_n, $n = 2m$, $m \in \mathbb{N}$ are critical.*

Proof. Our proof is based on the observation that the pyramidal graphs have a self similarity property. If we remove (peel) the layer of edges of Γ_n that emanate from the boundary nodes, the resulting graph is Γ_{n-2}. The number of layers that we can peel until no edges are left is m, and it is related to the number of boundary nodes as $n = 2m$.

To prove that the network is critical we must construct for every edge $e \in E$ a circular pair $(P_e; Q_e) \in \pi(\Gamma_n)$, such that the connection between P_e and Q_e is broken when e is removed (deleted) from Γ_n. We do so in two steps. First, we show that circular pairs $(P; Q)$ of maximal size $|P| = |Q| = m$ are uniquely connected. Then, we demonstrate how to construct such a pair, whose unique connection passes through a given edge e. Therefore, the deletion of e must break the connection.

Unique connectivity of maximal circular pairs: We show by induction over $n = 2m$ that any circular pair $(P; Q)$ of maximal size $|P| = |Q| = m$ is uniquely

Figure 4.2: Unique connections for maximal circular pairs $(P;Q)$ for induction base case $n = 4$. Nodes in P are $\circ$, nodes in Q are $\times$.

connected through Γ_n. Since

$$|P| + |Q| = 2m = n = |Y_B|,$$

we have $Y_B = P \cup Q$ and we can write, without loss of generality,

$$P = \{v_{s+1}, \ldots, v_{s+m}\},\ Q = \{v_{s+m+1}, \ldots, v_{2m}, v_1, \ldots, v_s\}, \tag{4.1}$$

for some integer s satisfying $1 < s \leq m$. The induction step is 4, so we consider two base cases: $n = 2$ and $n = 4$. The case $n = 2$ is trivial, because Γ_2 is a single resistor connecting the two boundary nodes v_1 and v_2. In the case $n = 4$ there exist two maximal circular pairs (up to swapping P and Q) $P = \{v_2, v_3\}$, $Q = \{v_1, v_4\}$, and $P = \{v_3, v_4\}$, $Q = \{v_1, v_2\}$. The unique connections are illustrated in figure 4.2.

Now, the subgraphs Γ_j of Γ_n, for $j = 2, 4, \ldots, n-2$, are obtained by repeated peeling of the layers of edges adjacent to the boundary, and subsequent relabeling of the nodes adjacent to the peeled edges as boundary nodes. In particular, we obtain Γ_{n-4} by peeling two layers from Γ_n.

The inductive hypothesis says that every maximal circular pair $(P';Q')$ of Γ_{n-4} is connected by a unique set of disjoint paths in Γ_{n-4}. To show that the maximal pair (4.1) of Γ_n is uniquely connected through the graph Γ_n, we must show that $(P;Q)$

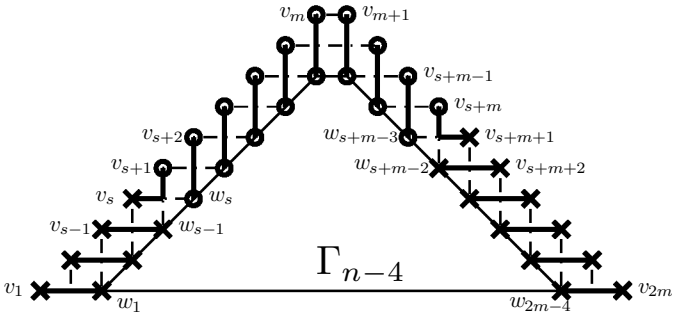

Figure 4.3: Induction step from Γ_{n-4} to Γ_n: connection between $(P;Q)$ and $(P';Q')$. Nodes in P and P' are $\circ$, nodes in Q and Q' are $\times$. Edges not in the connection are dashed, edges in the connection are thick solid. Narrow solid lines bound Γ_{n-4} (not actual edges).

must be connected to a maximal pair $(P';Q')$ of Γ_{n-4}, which we denote by

$$P' = \{w_s, w_{s+1}, \ldots, w_{s+m-3}\}, \quad Q' = \{w_{s+m-2}, \ldots, w_{2m-4}, w_1, \ldots, w_{s-1}\}. \tag{4.2}$$

Furthermore, the connection is unique. The construction is illustrated in figure 4.3, and we distinguish two cases.

The case $1 < s < m$**:** The connection is constructed starting with $v_1, v_{2m} \in Q$. Since these nodes are connected to Γ_n by horizontal edges only, these edges must be added to the connecting paths. Moreover, the paths must continue along horizontal edges to w_1 and w_{2m-4}, because if we take vertical edges, we reach the boundary nodes v_2, v_{2m-1}, that we are not allowed to touch.

Next, we observe that there is a unique way of connecting v_2 and v_{2m-1} to w_2 and w_{2m-5}, which is also by horizontal edges. Indeed, if we added the vertical edges to the paths, the paths would intersect with the horizontal edges added at the previous step. Similarly, we build the paths connecting the nodes from Q to Q', until we reach v_s and v_{s+m+1}. Arguing as before, all the edges must be horizontal.

It remains to connect the nodes in P. We start from $v_m, v_{m+1} \in P$, and since they are not allowed to be connected by a common horizontal edge, we add two vertical edges to the paths. The next two edges must also be vertical, otherwise the paths would either intersect, or touch the boundary at v_{m-1} or v_{m+2}. We repeat this argument for other nodes in P until we reach v_{s+1} and v_{s+m}. For each of the nodes $v_{s+1} \in P$ and $v_{s+m} \in P$ we add one vertical edge, at which point they meet with the horizontal edges added for $v_s \in Q$ and $v_{s+m+1} \in Q$, which completes the paths for these two pairs of nodes.

Thus, we have constructed the paths between $v_{s+1} \in P$ and $v_s \in Q$, and between $v_{s+m} \in P$ and $v_{s+m+1} \in Q$, while the remaining nodes in P and Q are connected by a unique set of paths (horizontal for Q, vertical for P) to the nodes in P' and Q'. Invoking the induction hypothesis for the maximal pair $(P'; Q')$ in Γ_{n-4}, we conclude that $(P; Q)$ is connected by a unique set of paths through Γ_n, for $1 < s < m$.

The case $s = m$: Arguing as above, the nodes of $P = \{v_{m+1}, \ldots, v_{2m}\}$ and $Q = \{v_1, \ldots, v_m\}$ are connected to P' and Q' by horizontal edges, since $v_1 \in Q$ and $v_{2m} \in P$. A circular pair $(P'; Q')$ has the form $P' = \{w_{m-1}, \ldots, w_{2m-4}\}$, $Q' = \{w_1, \ldots, w_{m-2}\}$, and $v_m \in Q$ is connected to $v_{m+1} \in P$ by a common horizontal edge. Then, the result follows by the induction hypothesis for the maximal pair $(P'; Q')$ in Γ_{n-4}.

Connection through a given edge: To complete the proof we need to show how to construct a maximal circular pair $(P_e; Q_e)$ for any given edge e, such that the unique connection passes through e. First, consider a horizontal edge e. As we showed above for $P = \{v_{m+1}, \ldots, v_{2m}\}$ and $Q = \{v_1, \ldots, v_m\}$, the unique connection passes through all horizontal edges of Γ_n. Thus, the deletion of any horizontal edge breaks the connection.

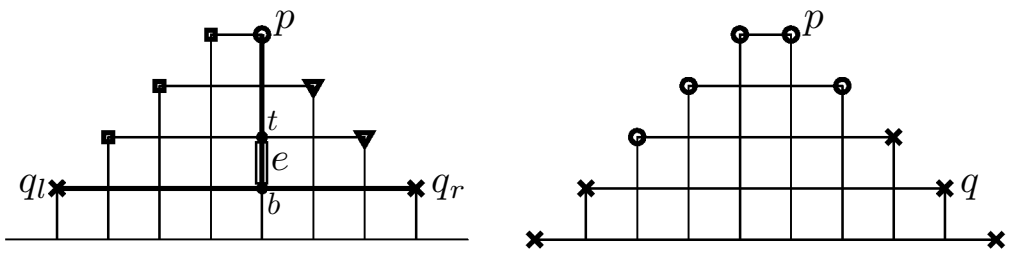

Figure 4.4: Left: two circular subsets of boundary nodes to choose from. Nodes in an even subset are $\bigtriangledown$, nodes in the odd subset are $\square$. Right: construction of (P_e, Q_e), nodes in P_e are $\circ$, nodes in Q_e are $\times$.

Let $e = (t, b)$ be a vertical edge with end nodes t (top) and b (bottom). We follow the vertical edges from t up to the boundary node p, that we add to P_e. We also consider a horizontal line of edges passing through node b. We denote the boundary end nodes of this line by $q_l \in B$ (left one) and $q_r \in B$ (right one), as shown in the left plot in figure 4.4.

Consider a subgraph of Γ_n consisting of its upper part lying on and above the horizontal line of edges connecting q_l and q_r. This subgraph is itself pyramidal with an even number of boundary nodes. Thus, one of the two subsets of boundary nodes lying either between p and q_r, or between q_l and p, must have an even number of nodes (zero is considered even). We choose the subset with even number of nodes and let q be either q_r or q_l depending on which subset we chose. Then, we add q to Q_e.

The rest of P_e and Q_e is populated as follows. Consider the two circular subsets of boundary nodes between p and q, and between q and p. Both subsets have an even number of nodes. Half of the nodes in each subset we add to P_e, and another half we add to Q_e, depending on whether the node is closest to p or q, respectively. This is illustrated in figure 4.4.

Now, we have constructed the maximal pair $(P_e; Q_e)$, which must be connected

by a unique set of m disjoint paths, as proved at step 1. Moreover, the path from p to q must consist of the following two segments: the line of vertical edges from b to p (this includes e), and the line of horizontal edges from b to q. Indeed, since $p \in P_e$, the construction of the unique path (step 1) shows that it should be connected to P'_e by vertical edges, which in turn is also connected to P''_e by vertical edges, and so on. Here we use the notation at step 1, with P'_e the set of $m-2$ points on the boundary of Γ_{n-4}, and P''_e the set of $m-4$ points on the boundary of Γ_{n-8}.

A similar argument for $q \in Q_e$ shows that its segment of the path consists of the horizontal edges. By the construction of p and q, these two path segments intersect at b. Finally, since the connection for $(P_e; Q_e)$ is unique, and the path between $p \in P_e$ and $q \in Q_e$ contains $e \in E$, deleting e from Γ_n breaks the connection, which completes the proof. □

4.1.2 Layer peeling for pyramidal networks

Now, let us show how to solve the inverse problem for the networks with pyramidal graphs $\Gamma_n = (Y, E)$, with a direct (layer peeling) algorithm that determines the conductance $\gamma : E \to \mathbb{R}^+$ in a finite number of algebraic operations.

The layer peeling algorithms for circular networks [26] is based on a concept of *special solutions*, which are the potentials arising from special choices of boundary data. These potentials limit the current flow to a certain subset of edges of a network, so that the conductance of these edges can be recovered. The edges are then "peeled", and the method proceeds deeper into the network, until the conductance of all edges is recovered. We use the same ideas to derive a layer peeling algorithm for pyramidal networks. Here we consider the networks with an even number n of boundary nodes. The extension to odd n is possible.

Algorithm 4.1.2. *To determine the conductance γ of the pyramidal network (Γ_n, γ), with given DtN map $\Lambda_\gamma \in \mathcal{D}_n$, take the following steps:*

(1) To compute the conductances of horizontal and vertical edges emanating from the boundary node v_p, for each $p = 1, \ldots, 2m$, define the following sets:

$Z = \{v_1, \ldots, v_{p-1}, v_{p+1}, \ldots, v_m\}$, $C = \{v_{m+2}, \ldots, v_{2m}\}$, $H = \{v_1, \ldots, v_p\}$ and $V = \{v_p, \ldots, v_{m+1}\}$, in the case $p \leq m$.

$Z = \{v_{m+1}, \ldots, v_{p-1}, v_{p+1}, \ldots, v_{2m}\}$, $C = \{v_1, \ldots, v_{m-1}\}$, $H = \{v_p, \ldots, v_{2m}\}$ and $V = \{v_m, \ldots, v_p\}$, for $m + 1 \leq p \leq 2m$.

(2) Compute the conductance $\gamma(e_{p,h})$ of the horizontal edge emanating from v_p, using

$$\gamma(e_{p,h}) = \left(\Lambda^{(n)}_{p,H} - \Lambda^{(n)}_{p,C} \left(\Lambda^{(n)}_{Z,C} \right)^{-1} \Lambda^{(n)}_{Z,H} \right) \mathbf{1}_H, \tag{4.3}$$

where $\mathbf{1}_H$ is a column vector of ones of size $|H|$.

Compute also the conductance $\gamma(e_{p,v})$ of the vertical edge emanating from v_p

$$\gamma(e_{p,v}) = \left(\Lambda^{(n)}_{p,V} - \Lambda^{(n)}_{p,C} \left(\Lambda^{(n)}_{Z,C} \right)^{-1} \Lambda^{(n)}_{Z,V} \right) \mathbf{1}_V. \tag{4.4}$$

(3) Once $\gamma(e_{p,h})$, $\gamma(e_{p,v})$ have been computed, peel the outer layer from Γ_n to obtain the subgraph Γ_{n-2} with the set $S = \{w_1, \ldots, w_{2m-2}\}$ of boundary nodes. Assemble the blocks K_S K_{SB}, K_{BS}, K_{BB} of the Kirchhoff matrix of (Γ_n, γ), and compute the updated DtN map $\Lambda^{(n-2)}$ of the network (Γ_{n-2}, γ), as follows

$$\Lambda^{(n-2)} = -K_S - K_{SB}\, P^T \left(P \left(\Lambda^{(n)} - K_{BB} \right) P^T \right)^{-1} P\, K_{BS}. \tag{4.5}$$

Here $P \in \mathbb{R}^{(n-2)\times n}$ is a projection operator: $PP^T = I_{n-2}$.

(4) If $m = 1$ terminate. Otherwise, decrease m by 1, update $n = 2m$ and go back to step 1.

The algorithm has two essential parts. First, the steps 1 and 2 are designed to restrict the current flow to the edges $e_{p,h}$ and $e_{p,v}$ emanating from the boundary node v_p. The potential drop on these edges is set to one and therefore, the conductance computed at step 2 is the current through v_p. Second, we peel the recovered layer in step 3, and compute the DtN map for the smaller network with graph Γ_{n-2}. Recursive application of these two operations recovers the whole network. The theoretical justification of the algorithm is in the following theorem.

Theorem 4.1.3. *The conductance γ of a pyramidal network (Γ_n, γ), with $n = 2m$, $m \in \mathbb{N}$, is uniquely recoverable from its DtN map $\Lambda_\gamma^{(n)}$ by Algorithm 4.1.2.*

Proof. The outline of the proof is as follows. First, we show that *special solutions* corresponding to the excitations defined at steps 1 and 2 of the algorithm, if they exist, give a unit potential drop on the edges emanating from the boundary node v_p. Then, we show the existence of such solutions. Finally, we establish formula (4.5) for the updated DtN map.

Special solutions with unit potential drop: Recall that $Y_B = \{v_1, \ldots, v_{2m}\}$ is the set of boundary nodes of Γ_n, and $S = \{w_1, \ldots, w_{2m-2}\}$ is the set of boundary nodes of Γ_{n-2}. This is the subgraph of Γ_n obtained by peeling the edges emanating from the nodes in Y_B. Let $e_{p,h} = (v_p, w_p)$, $e_{p,v} = (v_p, w_{p-1})$ be the horizontal and vertical edges emanating from $v_p \in Y_B$.

We construct the special solutions $u^{(p,h)}$ and $u^{(p,v)}$ so that the potential drop on $e_{p,h}$ and $e_{p,v}$ is one, and we can recover $\gamma(e_{p,h})$ and $\gamma(e_{p,v})$ from the measured current $J_p^{(h)}$ and $J_p^{(v)}$, respectively. The behavior of the special solutions is illustrated in figure 4.5.

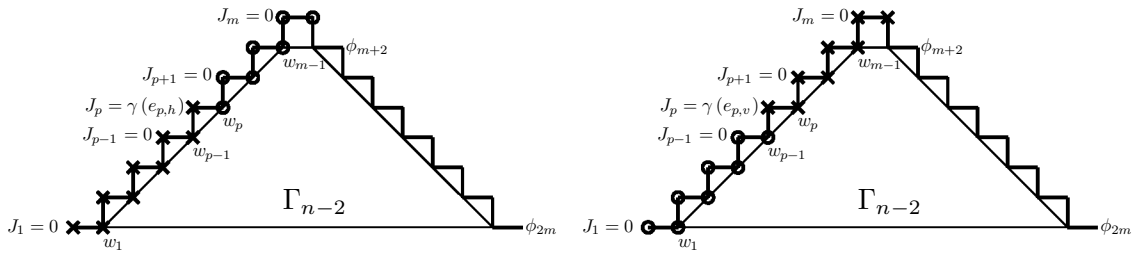

Figure 4.5: Special solutions. Left: special solution for $\gamma(e_{p,h})$; right: special solution for $\gamma(e_{p,v})$. Nodes with zero potential are $\circ$, nodes with unit potential are $\times$. Edges to be peeled are thick solid. Narrow solid lines bound Γ_{n-2} (not actual edges).

Consider first the case $1 \leq p \leq m$, and begin the construction of the special solution $u^{(p,h)}$ by setting the boundary conditions. The boundary conditions are stated in terms of the following subsets of Y_B: $H = \{v_1, \ldots, v_p\}$, $Z = \{v_1, \ldots, v_{p-1}, v_{p+1}, \ldots, v_m\}$, $F = \{v_{p+1}, \ldots, v_{m+1}\}$ and $C = \{v_{m+2}, \ldots, v_{2m}\}$. If we denote by ϕ the boundary potential, then its restriction to C, denoted by ϕ_C, is determined from the combination of Dirichlet and Neumann data

$$\begin{cases} \phi_H &= 1, \\ \phi_F &= 0, \\ J_Z &= 0. \end{cases} \tag{4.6}$$

This is shown later in the proof, where we establish the existence of special solutions.

Now, let us denote by ψ the restriction of the potential to S. The current at the boundary node v_j is given by

$$J_j = \gamma(e_{j,h})(\phi_j - \psi_j) + \gamma(e_{j,v})(\phi_j - \psi_{j-1}), \tag{4.7}$$

for all nodes in Y_B, except v_1 and v_{2m}, where only the first term is present. This is because there is only one horizontal edge emanating from each of these two nodes.

We show by induction that $u^{(p,h)}$, the potential drop on $e_{p,h}$ is one, and the drop on $e_{p,v}$ is zero. Thus, according to (4.7),

$$\gamma\left(e_{p,h}\right) = J_p^{(h)}. \tag{4.8}$$

Let us first show that $\psi_{p-1} = 1$. Since $v_1 \in Z \cap H$, equation (4.7) for $j = 1$ gives

$$0 = J_1^{(h)} = \gamma\left(e_{1,h}\right)(1 - \psi_1), \quad \text{therefore} \quad \psi_1 = 1.$$

Next, we proceed by induction in $j = 2, \ldots, p-1$, $v_j \in Z \cap H$. Suppose that $\psi_{j-1} = 1$, then (4.7) becomes

$$0 = \gamma\left(e_{j,h}\right)(1 - \psi_j),$$

which becomes $\psi_{p-1} = 1$ for $j = p - 1$.

Now we use another induction argument to show that $\psi_p = 0$. Since $v_m \in Z \cap F$ and $v_{m+1} \in F$, equation (4.7) for $j = m$ gives

$$0 = J_m^{(h)} = \gamma\left(e_{m,h}\right)(\phi_m - \phi_{m+1}) + \gamma\left(e_{m,v}\right)(\phi_m - \psi_{m-1}) = -\gamma\left(e_{m,v}\right)\psi_{m-1},$$

thus $\psi_{m-1} = 0$. We proceed by induction in $j = m - 1, \ldots, p + 1$, where $v_j \in Z \cap F$. Suppose that $\psi_j = 0$, then (4.7) gives

$$0 = \gamma\left(e_{j,v}\right)(0 - \psi_{j-1}),$$

and if we set $j = p + 1$, we get $\psi_p = 0$. We have just established that $\psi_{p-1} = 1$, $\psi_p = 0$, and since $\phi_p = 1$, (4.8) holds.

To determine $\gamma\left(e_{p,v}\right)$ we construct a special solution $u^{(p,v)}$ in a similar manner. The sets Z and C are the same as for $u^{(p,h)}$, while $V = \{v_p, \ldots, v_{m+1}\}$ and $F =$

$\{v_1, \ldots, v_{p-1}\}$. The boundary conditions are determined by (4.6), with H replaced by V. An induction argument similar to the one above, shows that the potential drop on $e_{p,h}$ is zero, and the drop on $e_{p,v}$ is one. Thus,

$$\gamma\left(e_{p,v}\right) = J_p^{(v)}. \tag{4.9}$$

Existence of special solutions: We now establish the existence of solutions with boundary conditions (4.6), by converting them to Dirichlet conditions, for which existence and uniqueness is known [27]. Since conditions on ϕ_H and ϕ_F are Dirichlet, we need to convert $J_Z = 0$ to a Dirichlet condition on ϕ_C, $C = Y_B \setminus (H \cup F)$. We rewrite $J_Z = 0$ using the DtN map as

$$0 = \Lambda_{Z,F}^{(n)}\phi_F + \Lambda_{Z,H}^{(n)}\phi_H + \Lambda_{Z,C}^{(n)}\phi_C, \tag{4.10}$$

which is combined with (4.6) to get

$$\phi_C = -\left(\Lambda_{Z,C}^{(n)}\right)^{-1}\Lambda_{Z,H}\mathbf{1}_H, \tag{4.11}$$

where $\mathbf{1}_H$ is a column vector of ones of size $|H|$. Thus, the question of existence of the special solution is equivalent to $\det \Lambda_{Z,C}^{(n)} \neq 0$.

To show the invertability of $\Lambda_{Z,C}^{(n)}$, we use the result from [27, Theorem 4.2], which says that for a circular pair $(P;Q)$ with $|P| = |Q| = k$, the condition $(-1)^k \det \Lambda_{P,Q} > 0$ is satisfied if and only if $(P;Q)$ is connected through the network, otherwise $\det \Lambda_{P,Q} = 0$. We demonstrate that $(Z;C) \in \pi(\Gamma_n)$ by constructing the connection explicitly, as shown in figure 4.6.

For $j = 1, \ldots, p-1$ we connect $v_j \in Z$ and $v_{2m-j+1} \in C$ with paths of horizontal

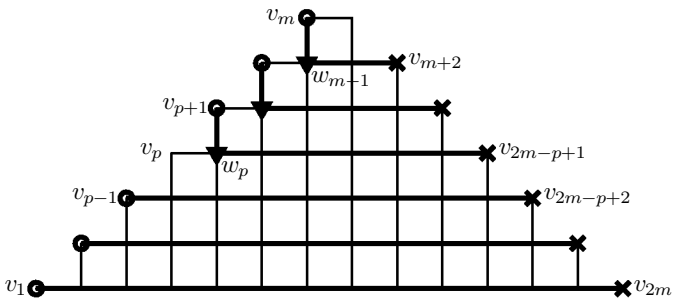

Figure 4.6: Connection for $(Z; C)$. Nodes in Z are $\circ$, nodes in C are $\times$. The paths are thick solid lines, edges not in the paths are narrow solid lines. Nodes at the intersections of vertical and horizontal path segments are ∇.

edges. For $j = p+1, \ldots, m$ we connect $v_j \in Z$ and $v_{2m-j+2} \in C$ with paths consisting of one vertical edge $e_{j,v} = (v_j, w_{j-1})$ and a path of horizontal edges connecting w_{j-1} and v_{2m-j+2}.

Recall that so far we considered the case $1 \leq p \leq m$. The case $m+1 \leq p \leq 2m$ is similar. In fact, since Γ_n is symmetric with respect to the vertical axis, the argument becomes identical to the previous one if we relabel the boundary nodes $v_j \to v_{2m-j+1}$, $j = 1, \ldots, 2m$. This exhausts all possible $v_p \in B$, and we can finally obtain the formulas (4.3)–(4.4) by substituting (4.11) into

$$J_p = \Lambda^{(n)}_{p,H}\phi_H + \Lambda^{(n)}_{p,C}\phi_C, \quad \text{and} \quad J_p = \Lambda^{(n)}_{p,V}\phi_V + \Lambda^{(n)}_{p,C}\phi_C.$$

DtN map update formula: Once we know the conductances of the edges emanating from Y_B, we peel the outer layer and reduce the inverse problem to the one for the smaller network (Γ_{n-2}, γ). It remains to derive the DtN map $\Lambda^{(n-2)} \in \mathbb{R}^{(n-2)\times(n-2)}$ of this network.

We rewrite equation (2.12) using the specific structure of the DtN map of (Γ_n, γ). The graph Γ_n consists of m layers of nodes. Each layer is a set of boundary nodes of

Γ_{2j}, $j = 1, \ldots, m$. The layer j is connected by paths of length one only to the two adjacent layers $j-1$ and $j+1$ (except for $j = 1, m$). Thus, the Kirchhoff matrix K of (Γ_n, γ) has a block tridiagonal structure

$$K = \begin{bmatrix} K_{11} & K_{12} & 0 & \cdots & 0 \\ K_{21} & K_{22} & K_{23} & \cdots & 0 \\ 0 & K_{32} & \ddots & \ddots & \vdots \\ \vdots & \vdots & \ddots & K_{SS} & K_{SB} \\ 0 & 0 & \cdots & K_{BS} & K_{BB} \end{bmatrix} = \begin{bmatrix} K_{II} & K_{IB} \\ K_{BI} & K_{BB} \end{bmatrix}. \tag{4.12}$$

Here $K_{jj} \in \mathbb{R}^{2j \times 2j}$, $j = 1, \ldots, m$, are the diagonal blocks with $K_{m-1,m-1} = K_{SS}$, $K_{m,m} = K_{BB}$. Furthermore, $K_{j,j+1} \in \mathbb{R}^{2j \times (2j+2)}$, $K_{j,j+1} = K_{j+1,j}^T$, $j = 1, \ldots, m-1$, are the off-diagonal blocks corresponding to connections between the layers j and $j+1$.

Using (4.12) we rewrite (2.12) as

$$\Lambda^{(n)} = K_{BB} - K_{BS} \left(K_{II}^{-1}\right)_{SS} K_{SB}. \tag{4.13}$$

We can also relate the potential ϕ at the boundary Y_B of Γ_n to the potential ψ at the boundary S of Γ_{n-2} via

$$K_{BS}\psi = (\Lambda^{(n)} - K_{BB})\phi. \tag{4.14}$$

Recall that the matrix of the DtN map is defined as the current response for boundary potential excitations that are the columns of an identity matrix. Thus, we rewrite (4.14) in matrix form with an identity matrix $\Psi = I_{n-2}$ and an unknown $\Phi \in \mathbb{R}^{n \times (n-2)}$,

to obtain an overdetermined matrix equation

$$K_{BS} = (\Lambda^{(n)} - K_{BB})\Phi, \tag{4.15}$$

that we now show to be solvable.

Note that once we recover the conductance for the edges emanating from Y_B, we know the blocks K_{BS} and K_{BB} of the Kirchhoff matrix K. Let $M = (\Lambda^{(n)} - K_{BB})$, and obtain from (4.13) that

$$M = -K_{BS}\left(K_{II}^{-1}\right)_{SS} K_{SB}. \tag{4.16}$$

To show that (4.15) is solvable, we need to show that M is full rank. We do so by considering a block LDU decomposition of K_{II}. Since K_{II} is block tridiagonal, it admits a decomposition

$$K_{II} = \begin{bmatrix} I & 0 & & \\ L_1 & I & \ddots & \\ & \ddots & \ddots & 0 \\ & & L_{m-2} & I \end{bmatrix} \begin{bmatrix} D_1 & 0 & & \\ 0 & D_2 & \ddots & \\ & \ddots & \ddots & 0 \\ & & 0 & D_{m-1} \end{bmatrix} \begin{bmatrix} I & U_1 & & \\ 0 & I & \ddots & \\ & \ddots & \ddots & U_{m-2} \\ & & 0 & I \end{bmatrix}, \tag{4.17}$$

where all blocks D_j, $j = 1, \ldots, m-1$, are non-singular, because K_{II} is invertible. If we denote the diagonal blocks of K_{II}^{-1} by Z_j, $j = 1, \ldots, m-1$, it can be shown [39, 40, 82] that they satisfy

$$Z_{m-1} = D_{m-1}^{-1}, \tag{4.18}$$

$$Z_j = D_j^{-1} + U_j Z_{j+1} L_j, \quad j = m-2, \ldots, 1. \tag{4.19}$$

Of particular interest to us is (4.18), which gives $Z_{m-1} = D_{m-1}^{-1} = \left(K_{II}^{-1}\right)_{SS}$, hence $\left(K_{II}^{-1}\right)_{SS}$ is invertible. Since Γ_n is connected, the blocks K_{BS} and K_{SB} are full rank. This establishes that M is of full rank.

We can now solve equation (4.15). Let $P \in \mathbb{R}^{(n-2)\times n}$ be a full rank projector, so that $PP^T = I_{n-2}$. Then, if we search for Φ in the form $\Phi = P^T\widehat{\Phi}$, we obtain from (4.15) that

$$PK_{BS} = PMP^T\widehat{\Phi}, \tag{4.20}$$

$$\Phi = P^T(PMP^T)^{-1}PK_{BS}. \tag{4.21}$$

The final step in deriving $\Lambda^{(n-2)}$ is to write the Kirchhoff law for the nodes in S. If $G = Y_I \backslash S$, then

$$K_{SG}u_G + (K_S + K_G)\psi + K_{SB}\phi = 0, \tag{4.22}$$

where we split K_{SS} in two parts $K_{SS} = K_S + K_G$, corresponding to the edges connecting S to Y_B and S to G, respectively. The DtN map of (Γ_{n-2}, γ) is then the current from S to B, given by

$$J_{SB} = -K_S\psi - K_{SB}\phi,$$

which we rewrite in matrix form using $\Psi = I_{n-2}$ and (4.21), to obtain (4.5). □

4.2 Optimal grids for pyramidal networks

The construction of the optimal grids presented below is based on an observation that the full knowledge of the optimal grid is not required for inversion. Indeed, to compute the reconstruction using (2.23) we only need to know the intersections $P_{\alpha,\beta}$ of the primary and dual grid segments. Our approach is to estimate these points

from the sensitivity analysis of both the continuum and the discrete EIT problems. The analysis is presented in sections (4.2.1) –(4.2.2). Then, the general definition of the grids is given in section (4.2.3). Finally, a particular case of grids for pyramidal networks in considered in section (4.2.4).

4.2.1 Kernel of the DtN map

We begin the sensitivity analysis with the derivation of the expression of the kernel of the DtN map. We need the Dirichlet Green's function $G(x, y)$, the solution of

$$\nabla_x \cdot (\sigma(x)\nabla_x G(x, y)) = -\delta(x - y), \quad x \in \Omega, \tag{4.23}$$

with homogeneous Dirichlet boundary condition

$$G(x, y)|_{x\in\mathcal{B}} = 0, \tag{4.24}$$

where $y \in \Omega$ is the *source* location.

Our numerical simulations are for domain $\Omega = \mathbb{D}$ the unit disk, and $\Omega = \mathbb{R}^2_-$ the lower half plane, respectively. In both cases we can write $G(x, y)$ explicitly [41] when $\sigma \equiv 1$, as needed in the computation of the optimal grids. For $\Omega = \mathbb{D}$ we have [41]

$$G_{\mathbb{D}}(x, y) = \frac{1}{2\pi}\left(-\log|x - y| + \log|y|\,(|x - \widetilde{y}|)\right), \tag{4.25}$$

where $\widetilde{y} = y/|y|^2$ and $|\cdot|$ is the Euclidean norm. When $\Omega = \mathbb{R}^2_-$,

$$G_{\mathbb{R}^2_-}(x, y) = \frac{1}{2\pi}\left(-\log|x - y| + \log|x - \widehat{y}|\right), \tag{4.26}$$

for $\widehat{y} = (I - 2\mathbf{e}_2\mathbf{e}_2^T)y$, I the 2×2 identity matrix, and $\mathbf{e}_2 = (0, 1)^T$.

Consider a general σ that we assume regular enough to admit the integral representation (2.19) of the DtN map, and let us derive the expression of the kernel $\mathcal{K}_\sigma(x,y)$ in terms of $G(x,y)$. Combining Green's second identity

$$\int_\Omega \left(f\nabla\cdot(\sigma\nabla g) - g\nabla\cdot(\sigma\nabla f)\right) dV = \int_{\mathcal{B}} \sigma\left(f\frac{\partial g}{\partial\nu} - g\frac{\partial f}{\partial\nu}\right) dS \tag{4.27}$$

for $f = u(x)$, $g = G(x,y)$, with (4.23), (4.24), (1.1) and (1.2) we obtain

$$u(y) = -\int_{\mathcal{B}} \sigma(x)\phi(x)\nu(x)\cdot\nabla_x G(x,y) dS_x, \quad y\in\Omega. \tag{4.28}$$

Then, we can write, formally,

$$\sigma(y)\left.\frac{\partial u}{\partial\nu}\right|_{y\in\mathcal{B}} = -\int_{\mathcal{B}} \sigma(y)\sigma(x)\left(\nu(x)\cdot\nabla_x\right)\left(\nu(y)\cdot\nabla_y\right) G(x,y)\phi(x) dS_x, \tag{4.29}$$

and obtain

$$\mathcal{K}_\sigma(x,y) = -\sigma(x)\sigma(y)\left(\nu(x)\cdot\nabla_x\right)\left(\nu(y)\cdot\nabla_y\right) G(x,y), \quad x,y\in\mathcal{B}. \tag{4.30}$$

Note that although $G(x,y)$ is not defined for $y\in\mathcal{B}$, equation (4.30) contains the normal derivative of $G(x,y)$ with respect to y, which is well defined.

Differentiating (4.25) and (4.26) we obtain the kernel $\mathcal{K}_1(x,y)$ of the DtN map for Laplace's equation in the unit disk and in the half plane, respectively. The Jacobian of $\widetilde{y}$ is given by

$$D_y(\widetilde{y}) = \frac{I}{|y|^2} - \frac{2yy^T}{|y|^4}, \tag{4.31}$$

which allows us to compute

$$\left(\nu(y)\cdot\nabla\right) G_{\mathbb{D}}(x,y) = \frac{1}{2\pi}\left(1 + 2y\cdot\widetilde{(x-y)}\right), \quad |y| = 1. \tag{4.32}$$

The second differentiation in conjunction with (4.31), (4.30) and $|x| = |y| = 1$ gives

$$\mathcal{K}_1(x,y) = -\frac{1}{\pi|x-y|^2}. \tag{4.33}$$

The expression of the kernel in the case $\Omega = \mathbb{R}^2_-$ is exactly the same. Moreover, formula (4.33) is valid for any region conformally equivalent to the unit disk. This follows from the invariance of the DtN map under conformal coordinate transformations [79].

The behavior of the kernel $\mathcal{K}_\sigma(x,y)$ for general σ is similar to (4.33) in the sense that away from the diagonal $x = y$, it admits the representation [51]

$$\mathcal{K}_\sigma(x,y) = -\frac{k(x,y)}{\pi|x-y|^2}. \tag{4.34}$$

Here $k(x,y)$ is a symmetric, positive continuous function on $\mathcal{B} \times \mathcal{B}$, that does not vanish on the diagonal.

4.2.2 Sensitivity functions

Given the kernel of the DtN map, we can now perform the sensitivity analysis with respect to the changes in σ. Since (4.30) gives $\mathcal{K}_\sigma(x,y)$ in terms of the Green's function, we compute first the sensitivity of $G(x,y)$.

Let $G(x,y) + \delta G(x,y)$ be the Green's function corresponding to the perturbed conductivity $\sigma + \delta\sigma$. To compute the sensitivity of G, it suffices to assume very small perturbations $\delta\sigma$ and approximate $\delta G(x,y)$ by the solution of the linearized equation

$$\begin{aligned} \nabla_x \cdot (\sigma(x)\nabla_x \delta G(x,y)) &= -\nabla_x \cdot (\delta\sigma(x)\nabla_x G(x,y)), \quad x \in \Omega, \\ \delta G(x,y) &= 0, \quad x \in \mathcal{B}. \end{aligned} \tag{4.35}$$

We have

$$\begin{aligned}\delta G(x,y) &= \int_\Omega G(x,s)\nabla_s \cdot (\delta\sigma(s)\nabla_s G(s,y))\, ds, \\ &= -\int_\Omega \delta\sigma(s)\nabla_s G(x,s)\cdot\nabla_s G(s,y) ds, \end{aligned} \tag{4.36}$$

where we integrated by parts.

Next, let us use linearization in equation (4.30) to write the perturbation $\delta\mathcal{K}_\sigma(x,y)$ of the kernel

$$\delta\mathcal{K}_\sigma(x,y) = \left(\frac{\delta\sigma(x)}{\sigma(x)} + \frac{\delta\sigma(y)}{\sigma(y)}\right)\mathcal{K}_\sigma(x,y) - \sigma(x)\sigma(y)\frac{\partial}{\partial\nu_x}\frac{\partial}{\partial\nu_y}\delta G(x,y). \tag{4.37}$$

Assuming that $\delta\sigma|_{\mathcal{B}} = 0$, we obtain from (4.37) and (4.36) that

$$\delta\mathcal{K}_\sigma(x,y) = \int_\Omega \delta\sigma(s) D\mathcal{K}_\sigma(s;x,y) ds, \tag{4.38}$$

with Jacobian

$$D\mathcal{K}_\sigma(s;x,y) = \sigma(x)\sigma(y)\left(\nabla_s\frac{\partial}{\partial\nu_x}G(x,s)\right)\cdot\left(\nabla_s\frac{\partial}{\partial\nu_y}G(s,y)\right), \quad s\in\Omega. \tag{4.39}$$

Moreover, in the case $\sigma\equiv 1$ used to compute the grids, we have

$$\nabla_s\frac{\partial}{\partial\nu_x}G(x,s) = \frac{1}{\pi|x-s|^2}\left(I - 2\frac{(x-s)(x-s)^T}{|x-s|^2}\right)\nu(x), \tag{4.40}$$

$$\nabla_s\frac{\partial}{\partial\nu_y}G(s,y) = \frac{1}{\pi|y-s|^2}\left(I - 2\frac{(y-s)(y-s)^T}{|y-s|^2}\right)\nu(y). \tag{4.41}$$

Now, let us derive similar sensitivity formulas for the discrete setting. Given the decomposition (2.10) of the Kirchhoff matrix, we note that the discrete equivalent of

the Green's function is

$$G = -K_{II}^{-1} K_{IB}. \tag{4.42}$$

Denote by γ_k the conductances in our critical network, for $k = 1, \ldots, g$, and $g = n(n-1)/2$. Note that the discrete DtN map $\Lambda_\gamma \in \mathbb{R}^{n \times n}$ has precisely g degrees of freedom, since it is symmetric, and its diagonal is determined by the conservation of currents. Thus, the critical network, which is uniquely recoverable from Λ_γ, has as many conductances as the number of degrees of freedom of Λ_γ. We obtain by differentiating (2.12) with respect to γ_k that

$$\frac{\partial \Lambda_\gamma}{\partial \gamma_k} = \begin{bmatrix} G^T & I \end{bmatrix} \frac{\partial K}{\partial \gamma_k} \begin{bmatrix} G \\ I \end{bmatrix}. \tag{4.43}$$

But K is linear in γ, so the partial derivative $\frac{\partial K}{\partial \gamma_k}$ is just the Kirchhoff matrix of a network with all the conductances being zero, except for $\gamma_k = 1$.

We denote by $\mathrm{vec}(M)$ the operation of stacking the entries in the strict upper triangular part of a matrix $M \in \mathbb{R}^{n \times n}$ in a vector of size g. Then, we can form the Jacobian matrix $D_\gamma \Lambda_\gamma \in \mathbb{R}^{g \times g}$, with entries given by

$$(D_\gamma \Lambda_\gamma)_{jk} = \left(\mathrm{vec} \left(\frac{\partial \Lambda_\gamma}{\partial \gamma_k} \right) \right)_j. \tag{4.44}$$

As the last step before defining the *sensitivity functions*, let us observe that the measurement operator $\mathcal{M}_n$ can be viewed as acting on the kernel of the DtN map. This is obvious for the pointwise measurements (2.20), and for measurements (2.17)

we have

$$\left(\mathcal{M}_n(D\mathcal{K}_\sigma)\right)_{ij}(s) = \begin{cases} \int\limits_{\mathcal{B}\times\mathcal{B}} \chi_i(x) D\mathcal{K}_\sigma(s;x,y)\chi_j(y)dxdy, & i \neq j, \\ -\sum\limits_{k\neq i} \int\limits_{\mathcal{B}\times\mathcal{B}} \chi_i(x) D\mathcal{K}_\sigma(s;x,y)\chi_k(y)dxdy, & i = j. \end{cases} \tag{4.45}$$

Definition The sensitivity function of the conductance γ_k with respect to the changes in the conductivity σ is the k^{th} component of the vector function

$$(D_\sigma\gamma)(s) = \left(D_\gamma \Lambda_\gamma|_{\Lambda_\gamma = \mathcal{M}_n(\Lambda_\sigma)} \right)^{-1} \mathrm{vec}\left(\mathcal{M}_n(D\mathcal{K}_\sigma)(s)\right), \quad s \in \Omega, \tag{4.46}$$

that we denote by $(D_\sigma\gamma_k)(s)$, $k = 1, \ldots, g$.

We are particularly interested in the sensitivity functions $D_1\gamma_k$ corresponding to $\sigma \equiv 1$. They are used to define the optimal grid, as explained next.

4.2.3 Definition of sensitivity grids

Given the sensitivity functions (4.46), we define the points

$$S_{\alpha,\beta} = \arg\max_{s\in\Omega}(D_\sigma\gamma_{k(\alpha,\beta)})(s), \tag{4.47}$$

where the solution $\gamma_{k(\alpha,\beta)}$ of the discrete inverse problem is most sensitive to changes in the continuum conductivity σ. Here k is an indexing operator that stacks all the conductances in a vector in $\mathbb{R}^g$. If the maximum in (4.47) is attained at multiple points in Ω, we define $S_{\alpha,\beta}$ as the arithmetic average of those points. We use the points $S_{\alpha,\beta}$ in (2.23), instead of the intersections $P_{\alpha,\beta}$ of the unknown grid lines, and we call the grids with nodes $S_{\alpha,\beta}$ the *sensitivity grids*.

Let us now illustrate the relationship between the points $S_{\alpha,\beta}$ and $P_{\alpha,\beta}$ in the case

of full boundary measurements, where we computed the optimal grid nodes explicitly in section 2.4.4. We show in figure 4.7 the optimal grids and the sensitivity functions for the circular networks. Note that the sensitivity functions of the conductances of various edges are mostly contained in the corresponding cells of the optimal grid. Moreover, the maxima $S_{\alpha,\beta}$ (the yellow squares in figure 4.7) are almost indistinguishable from $P_{\alpha,\beta}$ (the black circles in the figure).

4.2.4 Sensitivity grids for pyramidal networks

One can use the definition above to obtain sensitivity grids from any critical resistor network. However, not all network topologies give grids with good approximation properties. In particular, the numerical results in section 4.3 show that the pyramidal networks work better than the circular ones, for the partial data problem.

Note from figure 4.1 that in the pyramidal networks, the nodes v_1 and v_n which delimit the accessible boundary $\mathcal{B}_A$, are separated by $n-2$ interior nodes connected by the bottommost $n-1$ horizontal edges that we associate with the inaccessible boundary $\mathcal{B}_I$. Thus, the number of nodes associated with $\mathcal{B}_A$ and $\mathcal{B}_I$ grow at the same rate as n increases. In comparisson, *all* the boundary nodes of the circular networks are mapped to the accessible boundary conformally or quasiconformally. The conformal mappings preserve the isotropy of the conductivity, but give grids with poor resolution away from the center of $\mathcal{B}_A$. The quasiconformal grids have better resolution at the price of distortions in the reconstruction, due to the induced anisotropy of the conductivity. We believe that because the pyramidal networks allow the simultaneous growth of the sets of nodes in associated with $\mathcal{B}_A$ and $\mathcal{B}_I$, they are better suited for partial data EIT. This is supported by the numerical results in section 4.3.

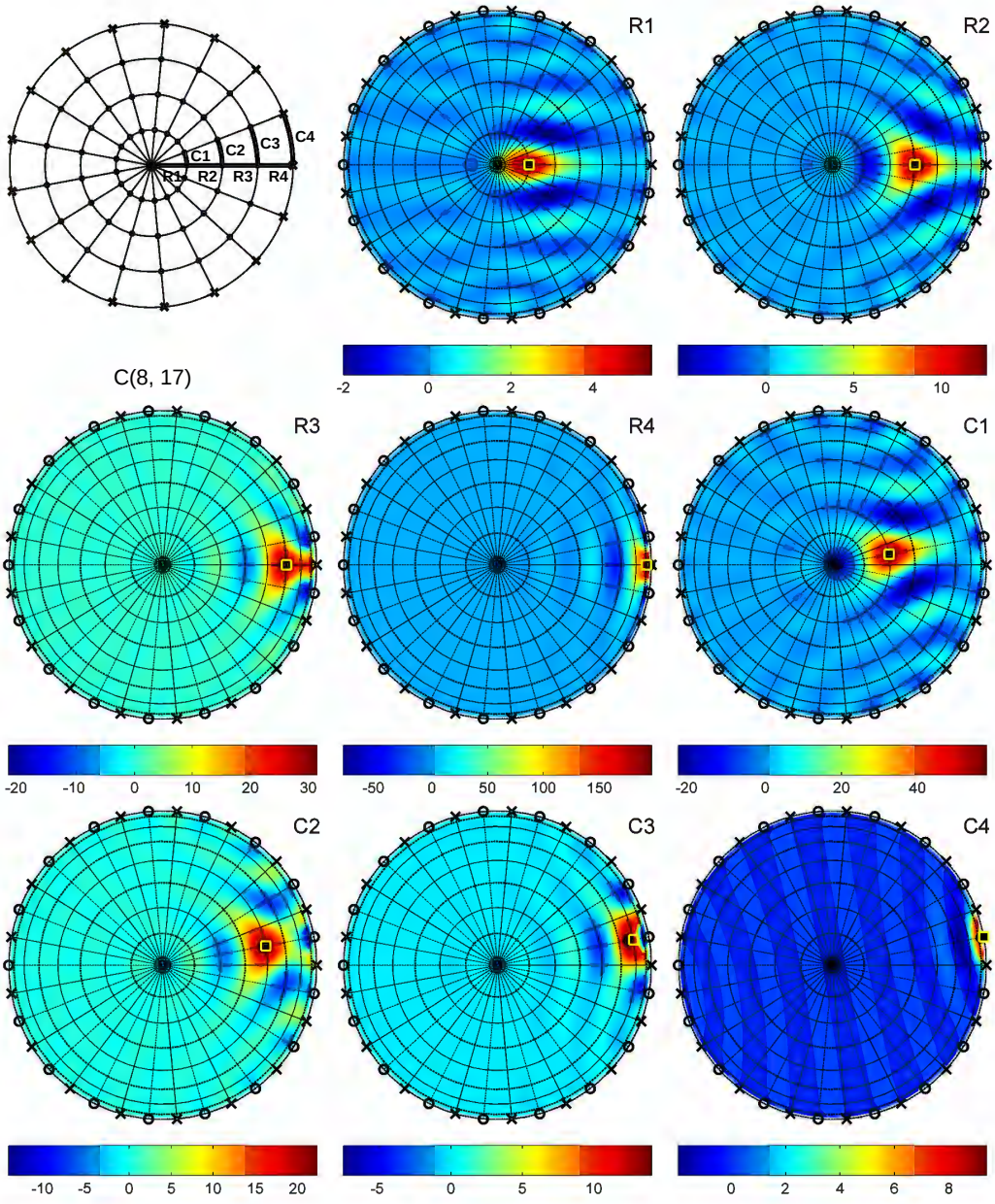

Figure 4.7: Sensitivity functions in $\mathbb{D}$ corresponding to the circular network and a tensor product optimal grid. Top left: circular network with 8 layers, $n = 17$, boundary nodes are $\times$, sensitivities are computed for the edges R1–R4 and C1–C4 (bold). Left to right, top to bottom: sensitivity functions for the radial (R1–R4) and angular (C1–C4) conductances. Optimal grid lines: primary are solid, dual are dotted. Nodes $P_{\alpha,\beta}$ are yellow $\square$, $S_{\alpha,\beta}$ are black $\bullet$.

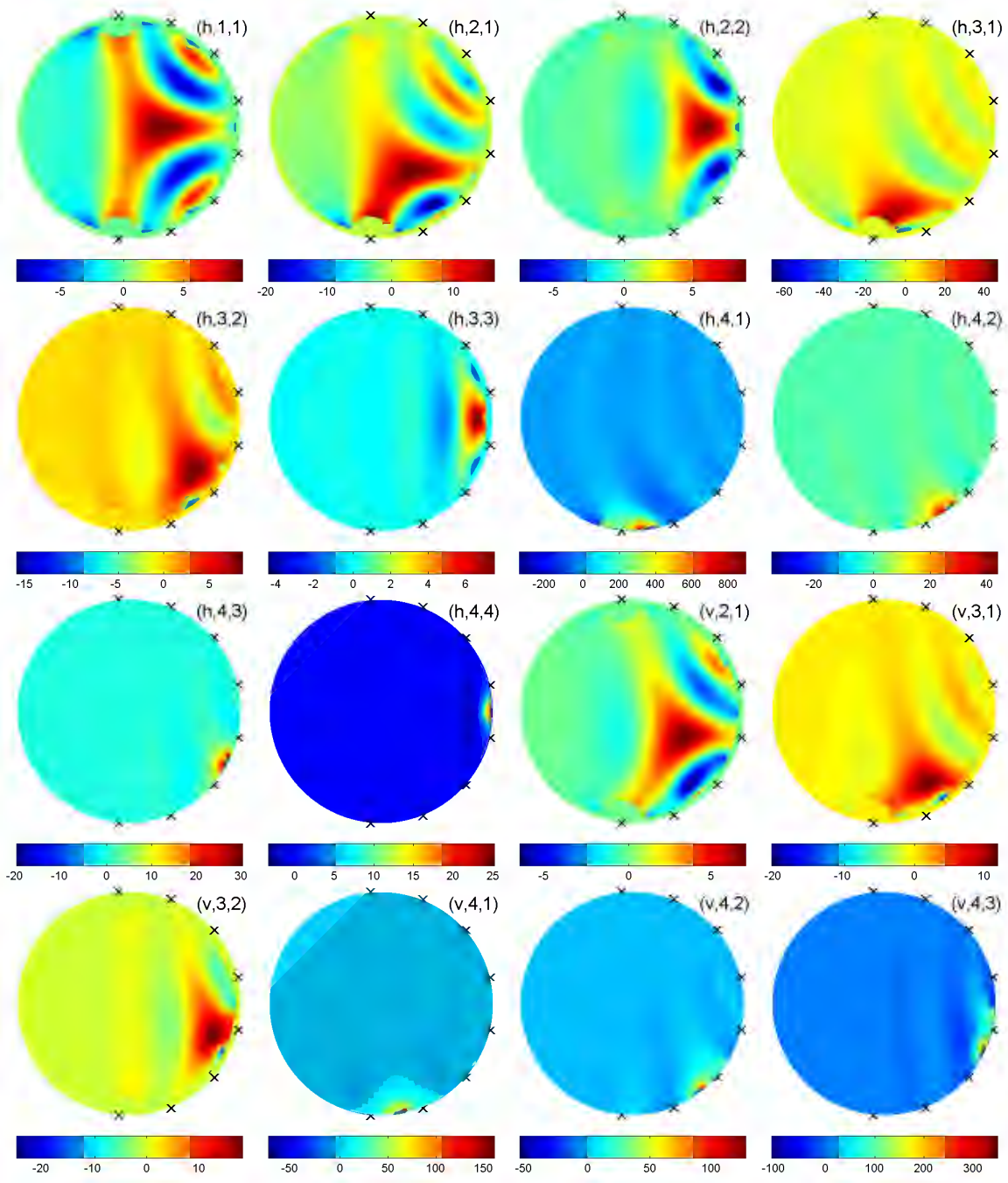

Figure 4.8: Sensitivity functions in $\mathbb{D}$ for the pyramidal network with $m = 4$, $n = 8$. The edges corresponding to each sensitivity function are indexed by (t, l, j), where $t \in \{h, v\}$ is the type of the edge (horizontal/vertical), l is the layer number and j is the index of the edge in the layer. θ_j are $\times$, $\beta = 0.52\pi$.

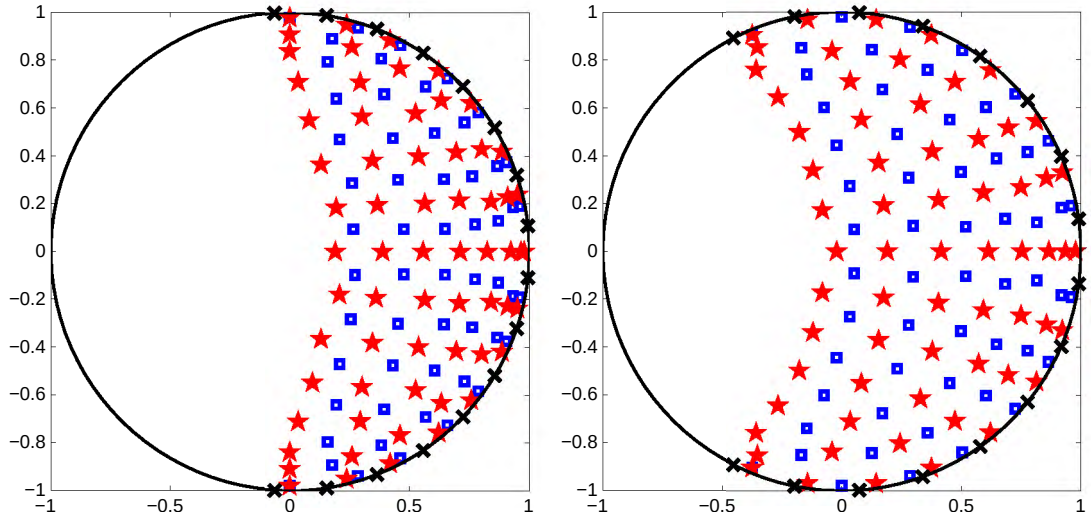

Figure 4.9: Sensitivity grids in $\mathbb{D}$ for Γ_{16}. Left: $\beta = 0.52$; right: $\beta = 0.65$. Blue $\square$ correspond to vertical edges, red $\bigstar$ correspond to horizontal edges, θ_j are black $\times$.

We illustrate in figure 4.8 the sensitivity functions $D_1\gamma_k$ in the unit disk $\mathbb{D}$, for the pyramidal network with $m = 4$ layers and $n = 8$ boundary nodes. We use the notation (t, l, j) to index the edges of Γ_n. Here $t \in \{h, v\}$ describes the type of the edge (horizontal/vertical), and $l = 1, \ldots, m$ determines the layer to which the edge belongs ($l = m$ is the outermost layer). The edges in layer l are indexed by j, with $j = 1, \ldots, 2l - 1$ for $t = h$, and $j = 1, \ldots, 2l - 2$ for $t = v$.

The supports of the measurement functions χ_j, used in (2.17) to define $\mathcal{M}_n(\Lambda_1)$, are centered at uniformly spaced points $\theta_j \in \partial\mathbb{D}$, $j = 1, \ldots, n$, on the accessible boundary $\mathcal{B}_A = \{\theta \mid \theta \in (-\beta, \beta)\}$. Note that θ_j are symmetric with respect to the middle $\theta = 0$ of the accessible boundary. This implies that $\mathcal{M}_n(\Lambda_1)$ is symmetric with respect to relabeling $v_j \to v_{2m-j+1}$, $j = 1, \ldots, 2m$, and so are the conductances. Thus, we only show in figure 4.8 the sensitivity functions for one half of the conductances in each layer l. The other half can be obtained from the symmetry $\theta \to -\theta$.

The sensitivity functions $D_1\gamma_k(s)$ shown in figure 4.8 have singularities near the

supports of χ_j. Once we "regularize" them, by setting them to zero in the vicinity of the singularities, we observe the well defined peaks that allow us to determine $S_{\alpha,\beta}$.

In figure 4.9 we show the grids obtained from the maxima of the regularized sensitivity function for two different sizes of the accessible boundary. While there is some grid refinement towards $\mathcal{B}_A$, the grids remain remarkably uniform deeper inside the domain. Note also that the neighboring points $S_{\alpha,\beta}$ form very regular quadrilaterals, that are close to being rectangular. This is what is typically expected from grids with good approximation properties.

4.3 Numerical results

In this section we present the numerical results with pyramidal networks and sensitivity grids. The reconstruction algorithm is discussed in section 4.3.1. It is followed by a description of the numerical experiments in section 4.3.2. The reconstructions are presented for the unit disk and for the half plane in sections 4.3.3 and 4.3.4, respectively. In the case of the unit disk, we compare the reconstructions with those obtained in section 3.3 using the conformal and quasiconformal mappings.

4.3.1 The inversion method

The algorithm that computes the reconstruction $\mathcal{Q}_n\left(\mathcal{M}_n(\Lambda_\sigma)\right)$ with the pyramidal networks and sensitivity grids is somewhat similar to that from section 3.3.1.

Algorithm 4.3.1. *To compute the reconstruction $\sigma^\star = \mathcal{Q}_n\left(\mathcal{M}_n(\Lambda_\sigma)\right)$ perform the following steps:*

(1) Let β be the size of the accessible boundary, and n the number of measurement functions χ_j, $j = 1, \ldots, n$. Let $\mathcal{M}_n(\Lambda_\sigma)$ be the measurements for the unknown

conductivity. Compute $\mathcal{M}_n(\Lambda_1)$ *for the constant reference conductivity* $\sigma \equiv 1$.

(2) Solve the discrete inverse problem (2.22) using algorithm 4.1.2, to obtain the conductances $\gamma^{(1)}_{\alpha,\beta}$.

(3) Use the solution of the discrete inverse problem from the previous step to compute the sensitivity functions $D_1\gamma^{(1)}_{\alpha,\beta}$ *as in (4.46). Compute the maxima* $S_{\alpha,\beta}$ *of the regularized sensitivity functions.*

(4) Solve the discrete inverse problem (2.21) using algorithm 4.1.2, to obtain the conductances $\gamma_{\alpha,\beta}$.

(5) Compute the reconstruction $\sigma^\star$ *as the piecewise linear interpolation of the following quantities*

$$\sigma^\star(S_{\alpha,\beta}) = \frac{\gamma_{\alpha,\beta}}{\gamma^{(1)}_{\alpha,\beta}}. \tag{4.48}$$

We implement the piecewise linear interpolation of (4.48) by computing the Delaunay triangulation of $S_{\alpha,\beta}$. Then, the reconstruction is defined on the union T of triangles in the triangulation. In the case of the unit disk, we remove from T the triangles that have all three vertices at points $S_{\alpha,\beta}$ corresponding to the bottommost chain of horizontal resistors in Γ_n. For each triangle in T, the vertex values of $\sigma^\star$ are interpolated by a linear function.

4.3.2 Implementation details

Similar to the reconstructions with circular networks and (quasi-)conformal mappings, we begin by choosing the number n of measurement functions, which is the same as the number of boundary nodes of the pyramidal network. Note that in comparison with the critical circular networks, for which the number of layers is roughly one quarter of

n, the pyramidal networks have a number of layers which is roughly $n/2$, which makes the layer peeling procedure less stable. Most of the numerical experiments presented below use the pyramidal networks with $n = 16$, only for the less stable high contrast case we set $n = 14$. The circular networks used for comparison have $n = 17$, since they are only recoverable for odd n.

For the reconstructions in the unit disk we use the same test conductivity functions as in section 3.3.2 (see figure 3.5). The high contrast conductivity used in section 4.3.3.3 is simply

$$\sigma(r,\theta) = \begin{cases} 1, & \theta \in \left[\frac{\pi}{2}, \frac{3\pi}{2}\right], \\ C_0, & \theta \in \left(0, \frac{\pi}{2}\right) \cup \left(\frac{3\pi}{2}, 2\pi\right), \end{cases} \tag{4.49}$$

where C_0 is the contrast factor.

The rotation parameter ω_0 is the same as in section 3.3.2. The integral in the mean relative error (3.36) is computed over the set T, as defined in the previous section.

4.3.3 Reconstructions in the unit disk

We present below the reconstructions in $\mathbb{D}$ for the smooth and piecewise constant conductivities of low and high contrasts. The reconstructions are computed for two sizes of the accessible boundary, $\beta = 0.52\pi$ (slightly more than half of $\partial\mathbb{D}$) and $\beta = 0.65\pi$ (almost two thirds of $\partial\mathbb{D}$).

4.3.3.1 Reconstructions of smooth conductivity.

We begin in figure 4.10 with the reconstructions of the smooth conductivity, for $\omega_0 = 6\pi/10$ and $\omega_0 = 3\pi/10$. Both reconstructions capture the features of the conductivity without visible distortions of the geometry. There is a slight loss of

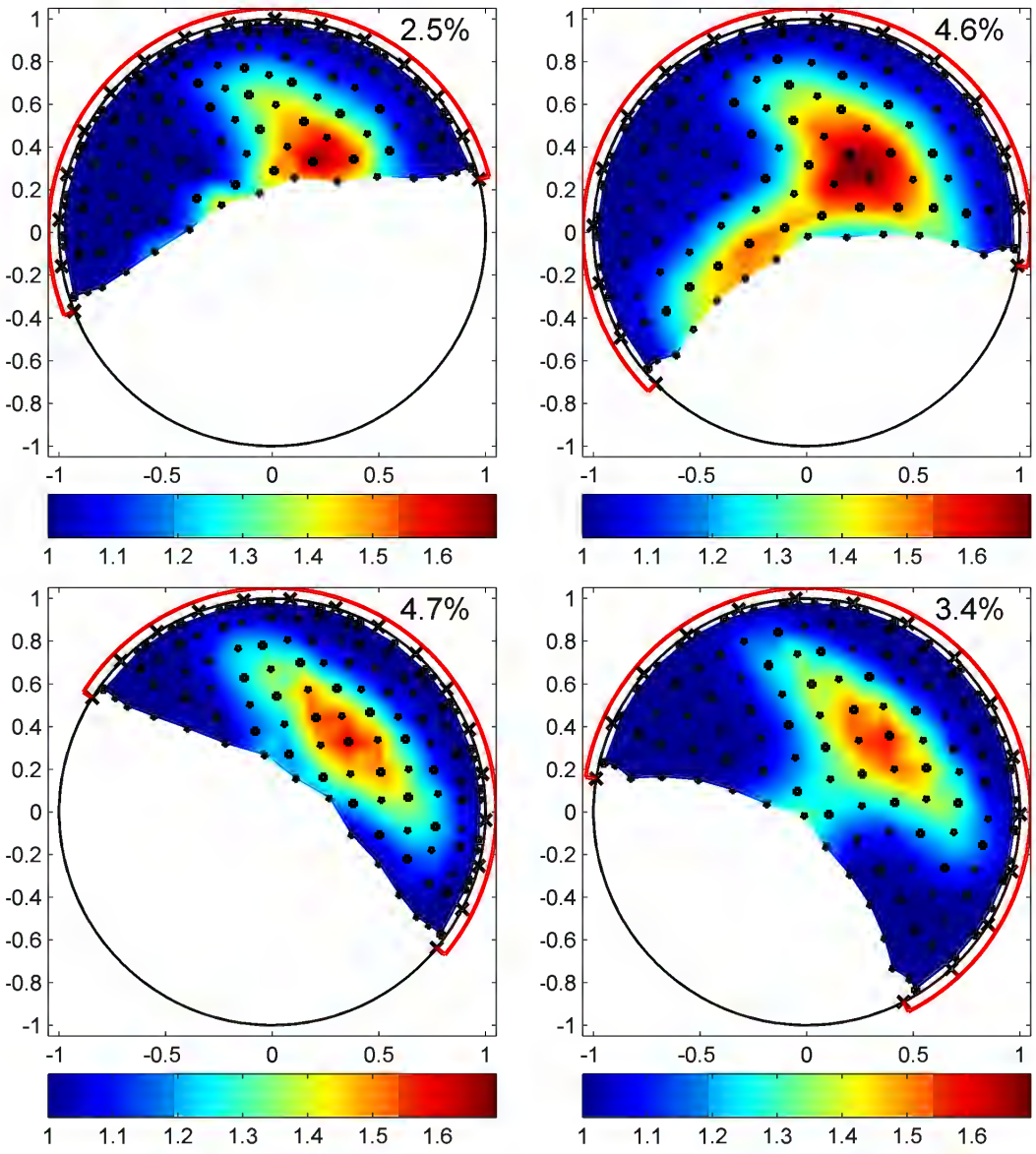

Figure 4.10: Reconstructions of smooth conductivity $sigX$ with $m = 8$, $n = 16$. Top row: $\omega_0 = 6\pi/10$; bottom row: $\omega_0 = 3\pi/10$. Left column: $\beta = 0.52\pi$; right column: $\beta = 0.65\pi$. Sensitivity grid nodes are $\bullet$, θ_j are $\times$, $\mathcal{B}_A$ is solid red. Percentages: mean relative errors $[E]$.

contrast in the case $\omega_0 = 3\pi/10$, however the overall error $[E]$ is still less than 5%.

In figure 4.11 we compare the reconstructions on the sensitivity grids with those obtained using a method of extremal quasiconformal mappings. We observe in figure

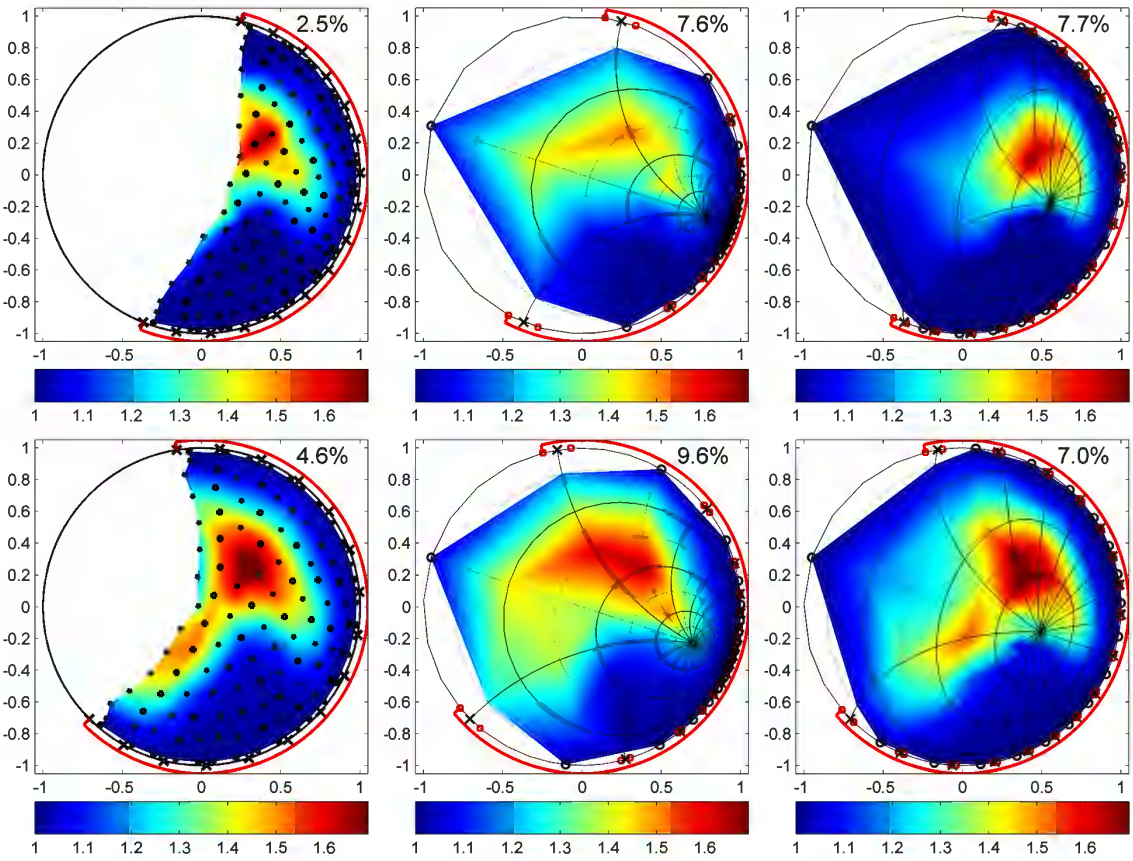

Figure 4.11: Comparison of reconstructions of smooth conductivity *sigX*, $\omega_0 = -\pi/10$. Top row: $\beta = 0.52\pi$; bottom row: $\beta = 0.65\pi$. Left column: reconstructions with pyramidal networks and sensitivity grids with $m = 8$, $n = 16$; middle column: conformal mapping reconstructions with $n = 17$; right column: quasiconformal mapping reconstructions with $n = 17$, $K = 0.52$(top), 0.65(bottom).

4.11 that in the case $\beta = 0.52\pi$, both the conformal and quasiconformal reconstructions have a mean relative error that is three times larger than that of the reconstruction on the sensitivity grid. As we expand $\mathcal{B}_A$ to $\beta = 0.65\pi$, the quasiconformal solution shows some improvement, but it still has a larger error [E]. Thus, the approach with pyramidal networks and sensitivity grids is superior, because it gives a uniform resolution, and it does not introduce any distortions.

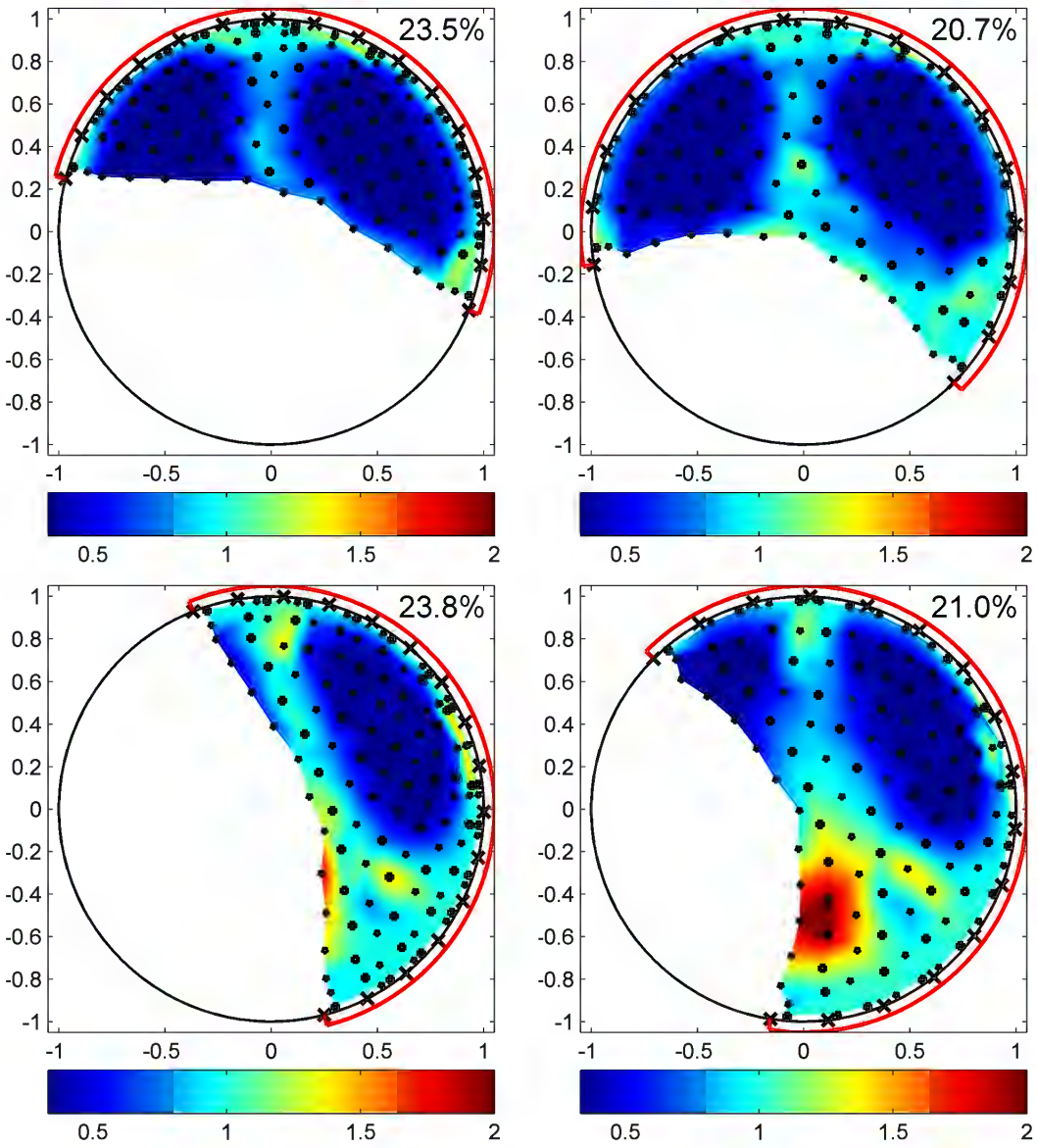

Figure 4.12: Reconstructions of piecewise constant conductivity *phantom1* with $m = 8$, $n = 16$. Top row: $\omega_0 = 4\pi/10$; bottom row: $\omega_0 = \pi/10$. Left column: $\beta = 0.52\pi$; right column: $\beta = 0.65\pi$. Sensitivity grid nodes are $\bullet$, θ_j are $\times$, $\mathcal{B}_A$ is solid red. Percentages: mean relative errors $[E]$.

4.3.3.2 Reconstructions of piecewise constant conductivity.

Let us now consider reconstructions of the piecewise constant chest phantom. We refer to the low and high conductivity regions of the phantom as the lungs and the

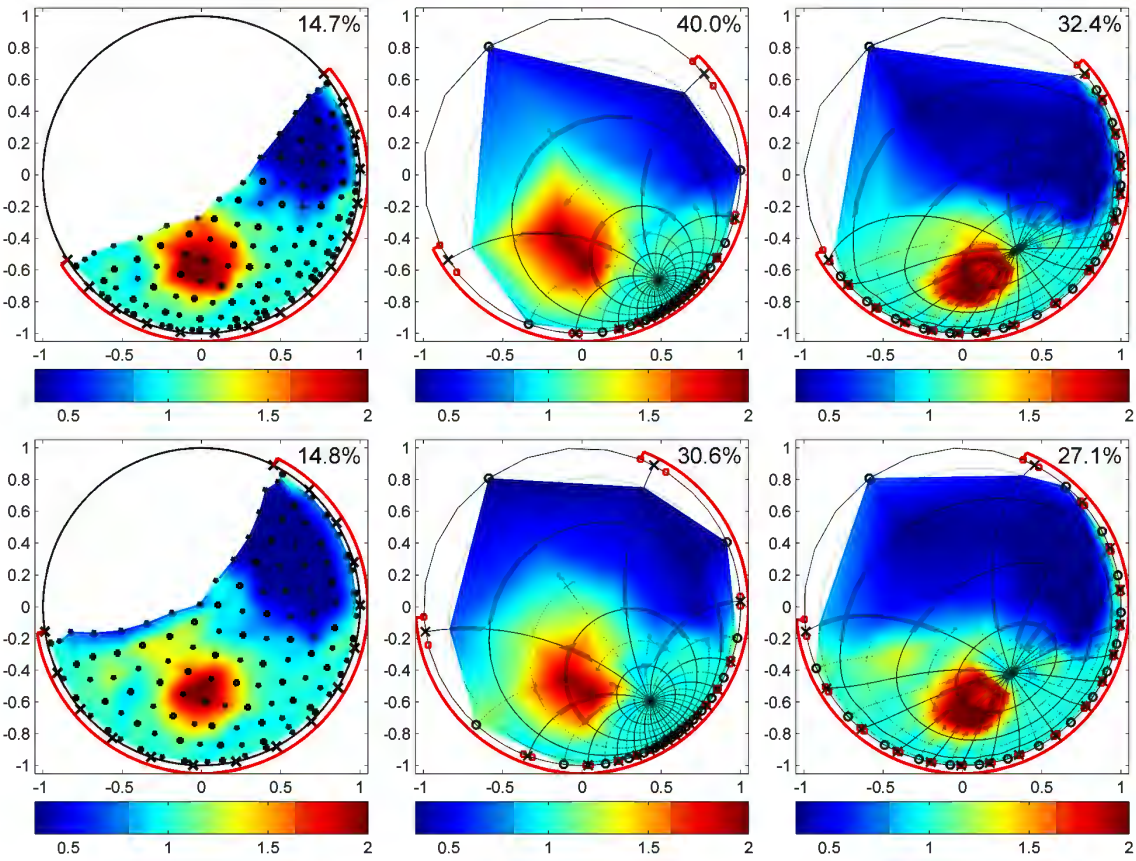

Figure 4.13: Comparison of reconstructions of piecewise constant conductivity *phantom1*, $\omega_0 = -3\pi/10$. Top row: $\beta = 0.52\pi$; bottom row: $\beta = 0.65\pi$. Left column: reconstructions with pyramidal networks and sensitivity grids with $m = 8$, $n = 16$; middle column: conformal mapping reconstructions with $n = 17$; right column: quasiconformal mapping reconstructions with $n = 17$, $K = 0.52$(top), 0.65(bottom).

heart, respectively. In figure 4.12, we show the reconstructions for $\omega_0 = 4\pi/10$ and $\omega_0 = \pi/10$.

We observe that the reconstructions have a much larger error $[E]$ compared to those for the smooth conductivity *sigX*. This is a manifestation of Gibbs phenomenon. In figure 4.12, this phenomenon is more pronounced in the case $\omega_0 = \pi/10$, especially for $\beta = 0.52\pi$, where we observe three overshoots near the right lung.

In figure 4.13, we compare the performance of our method with the method of

extremal quasiconformal mappings. Similar to the case of smooth conductivity, the reconstructions on the sensitivity grids are superior, with a mean relative error that is half of the error of the conformal and quasiconformal reconstructions.

4.3.3.3 High contrast reconstructions

An advantage of the reconstruction mapping based on resistor networks is that it is obtained from the full non-linear inverse problem, without artificial regularization, aside from limiting the size of the networks. Thus, it avoids the problems of many other approaches, that often struggle to recover high contrast features of $\sigma(x)$. The numerical results in this section show that our reconstructions capture contrasts that are orders of magnitude larger than those recoverable by traditional approaches.

In the top row of figure 4.14 we present reconstructions of the piecewise constant conductivity 4.49, with exceptionally large contrast $C_0 = 10^4$. The mean relative error does not give a clear estimate of the quality of the reconstruction for such a large contrast, so we use the pointwise relative error $E(z)$ instead, which we show in the bottom row of figure 4.14.

Our method is able to capture both the location of the interface of discontinuity and the values of the conductivity on both sides of the interface. While the relative error is large near the interface due to the spurious oscillations, away from the interface the error is less than 5%. Note that these reconstructions are achieved without any special assumptions on the conductivity, which shows the versatility of the method.

4.3.4 Reconstructions in the half plane

We already mentioned in section 4.2.4 that the pyramidal networks are better suited for the partial data EIT problem, because of the fixed ratio of the number of nodes

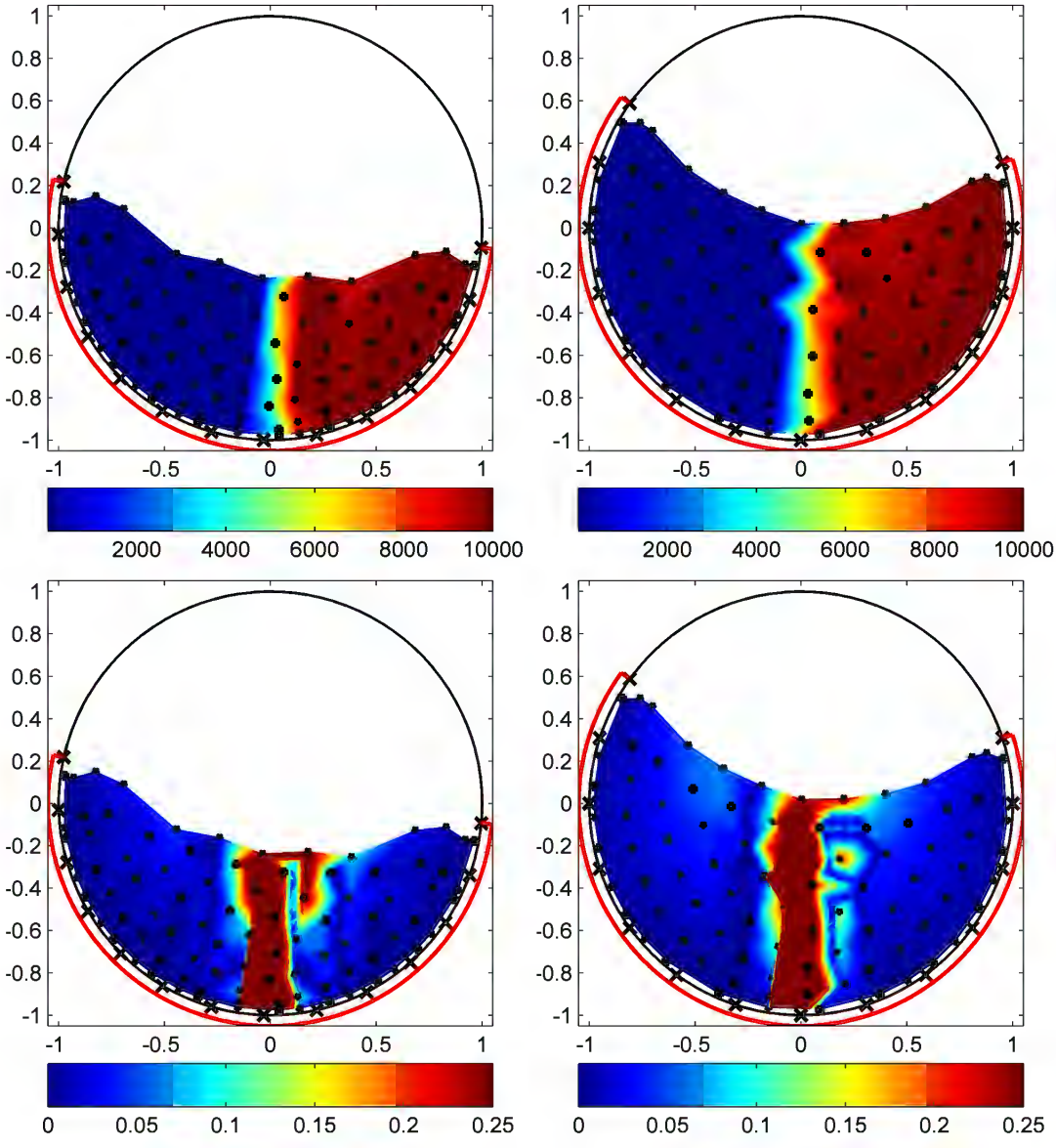

Figure 4.14: Reconstructions of high contrast piecewise constant conductivity with $m = 7$, $n = 14$, $\omega_0 = -11\pi/20$. Top row: reconstructions; bottom row: pointwise relative error $E(z)$. Left column: $\beta = 0.52$; right column: $\beta = 0.65$. Sensitivity grid nodes are $\bullet$, θ_j are $\times$, $\mathcal{B}_A$ is solid red.

associated with the accessible and inaccessible parts of the boundary. The sensitivity grids obtained from these networks have good approximation properties for order one ratios of the accessible and inaccessible boundary, as illustrated with the numerical

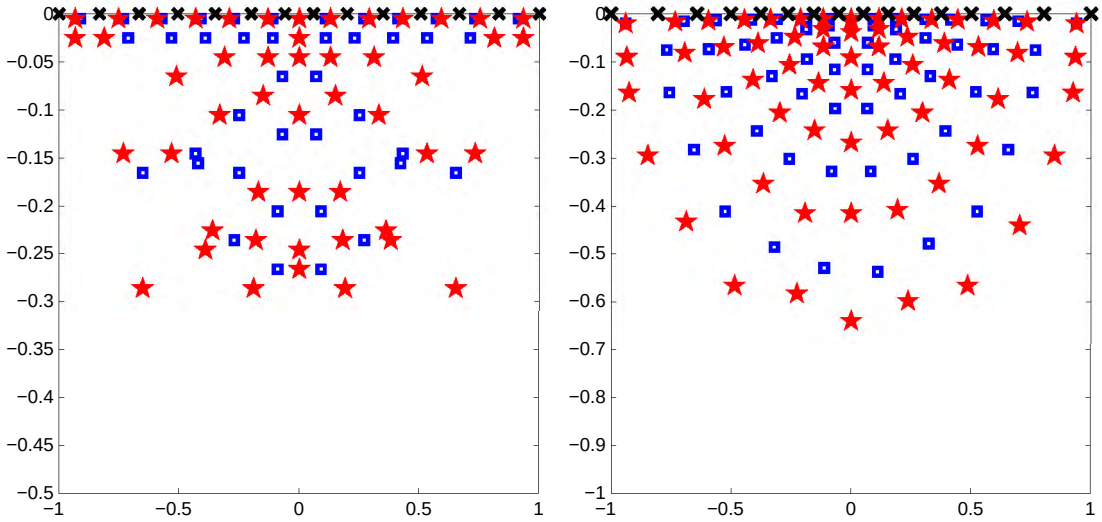

Figure 4.15: Optimal grids in the half plane. Left: sensitivity grid computed directly ($n = 14$); right: sensitivity grid mapped conformally from the unit disk ($n = 16$). Blue □ correspond to vertical edges, red ★ correspond to horizontal edges, measurement points x_j are black ×.

results above. When this ratio approaches infinity, we are basically in the full boundary measurement case, where the circular networks are more appropriate. Here we discuss the other limit, where the ratio tends to zero. This limit arises when considering the EIT problem in the lower half plane $\mathbb{R}^2_-$, with measurements limited to a finite segment of the horizontal axis.

Let $\mathcal{B}_A = [-1, 1]$ be the accessible boundary, and let the "measurement points" $x_j \in \mathcal{B}_A$ be the centers of the supports of the measurement functions $\chi_j(x)$. If we attempt to compute the sensitivity grid for an arbitrarily chosen distribution of x_j, it will likely have poor properties for inversion. See for example the grid shown in the left plot in figure 4.15. To get a good grid, in this limit case of zero ratio of accessible to inaccessible boundary, we use conformal mappings. We map conformally a grid that has good properties in one domain (e.g. the unit disk with measurements at points θ_j, uniformly distributed on half of the boundary) to the half plane, with

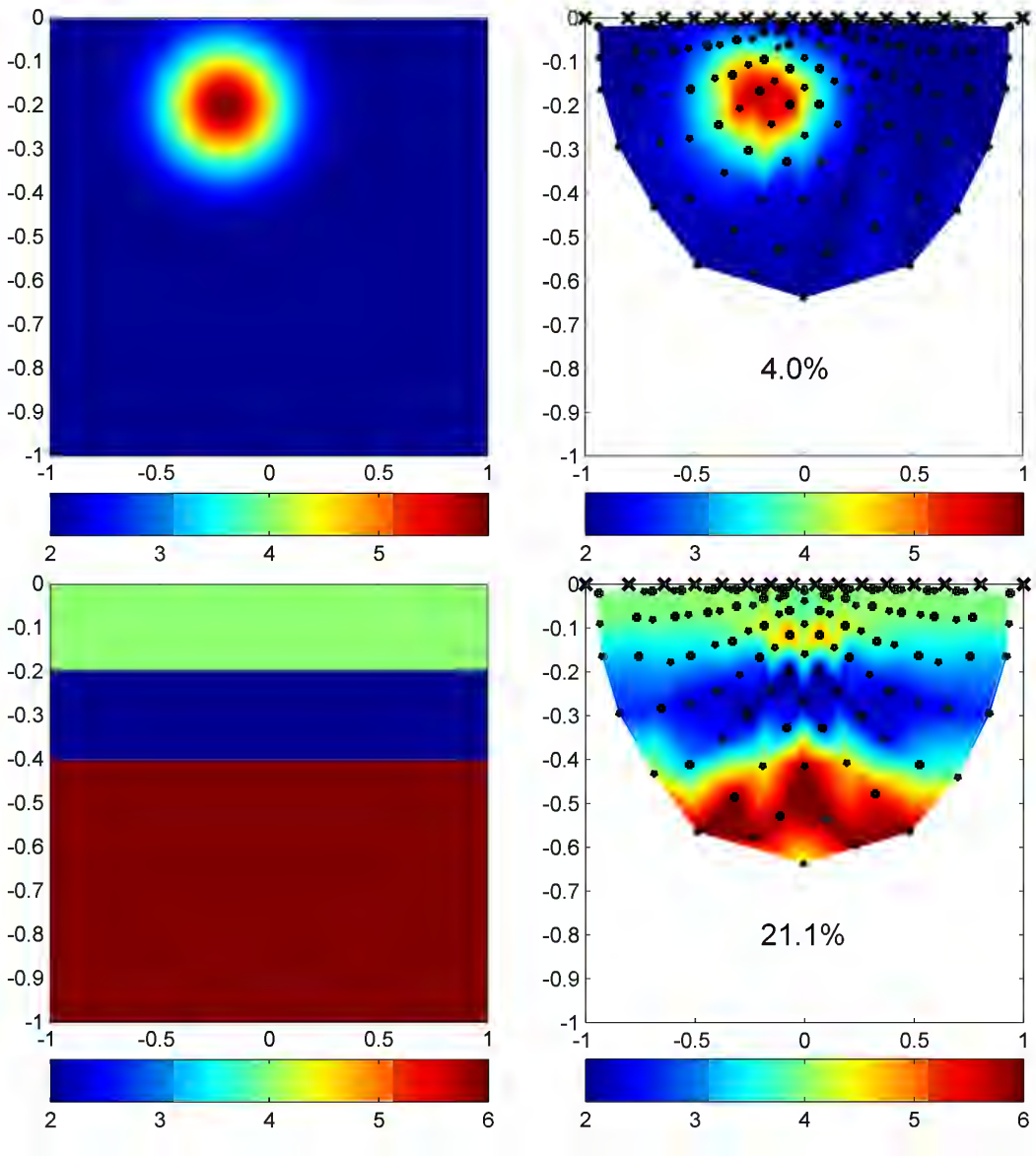

Figure 4.16: Reconstruction in the half plane with $m = 8$, $n = 16$. Top row: smooth conductivity σ_g; bottom row: piecewise constant conductivity σ_l. Left column: true conductivities; right column: reconstructions. Grid nodes are $\bullet$, x_j are black $\times$, percentages are $[E]$.

measurements in $\mathcal{B}_A$.

The grid in the right plot in figure 4.15 is obtained with the conformal fractional

linear transform $w : \mathbb{D} \to \mathbb{R}^2_-$ given by

$$w(z) = ih\frac{\bar{z}-1}{\bar{z}+1}, \qquad h = \tan\left(\frac{\pi-\beta}{2}\right), \tag{4.50}$$

for which the distribution of x_j is

$$x_j = h\cot\left(\frac{\pi-\theta_j}{2}\right), \qquad j = 1,\ldots,n. \tag{4.51}$$

We observe that the distribution of the nodes of the resulting grid is very regular, and there is greater penetration depth compared to that of the grid computed directly from the regularized sensitivity functions. The numerical reconstructions in figure 4.16 are obtained with the conformally mapped grid.

Similar to the study in $\mathbb{D}$, we reconstruct both a smooth and a piecewise constant conductivity in $\mathbb{R}^2_-$. The smooth conductivity σ_g consists of a single inclusion in the homogeneous background medium modeled by a Gaussian. The piecewise constant conductivity σ_l has three horizontal layers. Both test conductivities are shown in the left column in figure 4.16. The reconstructions are shown in the right column.

As in the case of the unit disk, we observe a much smaller error $[E]$ for the reconstruction of a smooth conductivity compared to that of the reconstruction of the piecewise constant σ_l. While both the position and the magnitude of the Gaussian inclusion are determined with high precision, the magnitude of the middle layer of σ_l is somewhat overestimated, and there are also two symmetric overshoots in the top layer. However, the overall quality of the reconstruction is comparable to what we observe in the unit disk, which shows that our method is versatile with respect to the choice of the domain.

Chapter 5

Conclusions and future work

In this thesis we developed two distinct approaches to the numerical solution of the EIT problem with partial boundary measurements in two dimensions. Both approaches extend the method of numerical solution of the full data EIT presented in [15, 44]. The method relies on a model reduction technique that encodes the information about the unknown conductivity function in a few parameters. The reduced models are well connected, critical resistor networks that are consistent with discrete measurements of the DtN map of the continuum problem, and are uniquely determined by them. The resistor networks arise in finite volume discretizations of the elliptic equation for the electric potential on staggered grids. A special choice of the grids, the so-called optimal grids, is used to connect the solution of the discrete inverse problem for resistor network to the numerical approximation of the solution of the continuum EIT. The optimal grids are computed as a part of the inverse problem, so that they solve exactly the discrete inverse problem for a reference constant conductivity.

The construction of the optimal grids for the full data EIT in [15, 44] is based on the rotational symmetry of the problem for the constant conductivity in the unit

disk. Thus, the grids are essentially one dimensional, since they are tensor products of uniform angular grids and non-uniform adaptive radial grids. In the partial data EIT the rotational symmetry is broken, so a different approach must be taken. Our main contribution in chapter 3 is the construction of the optimal grids for the partial data problem that uses the theory of extremal quasiconformal (Teichmüller) mappings. The idea is to map the problem with partial measurements on the accessible boundary to the problem with equidistantly distributed measurements on the entire boundary. Thus, the problem is reduced to the full data case that we can solve using the method from [15, 44].

We perform in chapter 3 extensive numerical and analytical studies, and we make the following crucial observations about the aforementioned approach. First, there is a direct connection between the coordinate transformations and the anisotropy of the conductivity. The only family of mappings that preserve the isotropy of the transformed conductivity are the conformal mappings. Second, the properties of the mappings inside the domain have a strong influence on the boundary behavior and vice versa. This is important, since the boundary behavior of the coordinate transformations determines the placement of the measurements.

Enforcing the conformality of the mapping leads to clustering of the measurements around the midpoint of the accessible boundary. This in turn leads to poor resolution of the reconstructions away from the middle of the accessible boundary. If we relax the conformal requirement, we need to consider the quasiconformal mappings, that lead to anisotropic transformed conductivities. Since the anisotropy is an artifact of the method, we minimize it by using the extremal quasiconformal mappings. The grids obtained using Teichmüller mappings exhibit a much more uniform resolution than those obtained with the conformal mappings. They are also more flexible with respect to positioning of the measurements on the boundary. However, the numerical results

demonstrate that the reconstructions on such grids somewhat distort the features of the conductivity. We attribute such behavior to the presence of the artificial anisotropy.

Our motivation for an alternative approach to the partial data problem comes from the realization that the problems of the reconstructions with conformal and extremal quasiconformal mappings are due to the essentially one dimensional structure of the optimal grids, and the inadequate topology of the reduced models, the circular resistor networks, for the partial measurements setup. In chapter 4 we study the pyramidal networks, that are much better suited for the partial data problem. Our contribution to the study of discrete inverse problem is the proof of criticality of the pyramidal networks, and the construction of a fast direct layer peeling algorithm, that solves the discrete inverse problem for pyramidal networks in a finite number of algebraic operations.

The use of pyramidal networks brings a significant difficulty. Namely, the problem of finding the optimal grid for pyramidal network cannot be reduced to one dimension. We solve this difficulty by introducing a novel approach to computing the truly two dimensional optimal grids, using the sensitivity analysis of both the continuum and the discrete EIT problems. Explicitly, the optimal grid nodes are computed as the maxima of the sensitivity functions of the solutions of the inverse discrete problem with respect to the changes of the continuum conductivity. Such an approach is indeed very flexible. It provides a unified framework for computing the optimal grids, that is independent of the choice of the domain and the topology of the network. The numerical experiments with the reconstructions in both the unit disk and the half plane support this observation. Another important property of the sensitivity grids observed in the numerics is that they combine the advantages of both the conformal and quasiconformal grids in the circular case without having the drawbacks of either

of them. The sensitivity grids provide both uniform resolution and the absence of distortions in the reconstructions.

Our methods compare favorably to more traditional approaches to the numerical solution of the EIT. First, our methods do not rely on any form of artificial regularization aside from limiting the size of the networks and the number of measurements. This helps to avoid the artifacts in the reconstructions due to arbitrary choices of penalty functionals and parameters. Second, our methods do not require any prior information on the conductivity. No assumptions on regularity or location of the features are necessary. Third, the use of layer peeling algorithm for the solution of the discrete inverse problem makes the reconstruction extremely fast. In fact, solving the whole discrete inverse problem is faster than evaluating a single Jacobian for the problem of comparable discretization size. Thus, our method is faster than one iteration of any optimization based approach. Finally, since the reconstruction is based on the solution of the full non-linear problem, we are able to recover the contrasts in the conductivities that are orders of magnitude higher than those attainable via linearization or optimization based methods.

5.1 Future work

The results obtained in this thesis can be extended and improved in several ways. The list below summarizes possible topics of future work.

Partial data EIT with measurements on disjoint subsets of the accessible boundary. In this thesis we considered the partial measurements on the connected subsets of the boundary. However, in many practical applications the measurements are made on several disjoint subsets of the boundary. For example, in geophysical exploration cross-well tomography is used, where the measurements are made simul-

taneously in two parallel wells. As our studies show, the topology of the underlying discrete problem is of crucial importance for the study of partial data problems. Thus, the first step in solving the two-sided inverse problem would be finding an appropriate resistor network topology.

Non-stationary inverse problem. Although we associated the problem of finding the coefficient of an elliptic equation from the DtN map with the EIT problem, similar mathematical formulations also arise in other physical settings. For example, equation (1.1) describes the pressure of a stationary flow in porous medium with permeability σ governed by Darci's law. However, the problem of hydrological imaging differs from EIT due to the large time scales required for the flow to become stationary. Thus, it makes sense to study the time dependent parabolic equation instead of the stationary elliptic one.

Compatibility of three dimensional data with circular planar networks. The study of the two dimensional EIT in this thesis was possible due to the results on the compatibility of the measured data with the discrete models. In fact, the two dimensional DtN maps are almost completely characterized for both the discrete and continuum settings [51, 27]. No such characterization exists in three dimensions. The study of conditions under which the measured three dimensional DtN map may be compatible with planar networks would be the first step towards the inversion in three dimensions.

Three-dimensional EIT with resistor networks. The research on the applications of resistor networks to the numerical solution of EIT [15, 44, 18, 19] was made possible due to the theory of discrete inverse problems developed by Morrow, Ingerman and others in [26, 27, 28, 49]. Unfortunately, the theory is only applicable to the circular planar graphs, that restricts its use to two spatial dimensions. However, it seems that the crucial concept of criticality of resistor networks can be generalized to

networks with non-planar graphs, which may provide the opportunities for the study of the three dimensional problem. It should be mentioned that if the networks of suitable topology are found, the optimal grids can be constructed using the sensitivity approach that we developed here.

Extensions of the approach based on discrete models and optimal grids to other inverse problems. The use of resistor network models and the optimal grids for EIT was motivated by an earlier success of a similar approach to the inverse spectral problem in one dimension [14, 16]. In this thesis we have overcame one of the difficulties that limited this approach to the cases where the optimal grids must be computed from one dimensional arguments. The sensitivity grid approach effectively eliminates all such constraints. However, if one wishes to generalize the methods developed here to other inverse problems, it is still required to build the appropriate discrete models that admit a well-defined solution of the discrete inverse problem. This may present substantial difficulties, since the discrete inverse problems may have rather elaborate structure, as can be seen in the case of resistor networks with circular planar graphs.

Bibliography

[1] G. Alessandrini. Stable determination of conductivity by boundary measurements. *Applicable Analysis*, 27(1):153–172, 1988.

[2] G. Alessandrini. Singular solutions of elliptic equations and the determination of conductivity by boundary measurements. *Journal of Differential Equations*, 84(2):252–272, 1990.

[3] K. Astala and L. Päivärinta. Calderón's inverse conductivity problem in the plane. *Annals of Mathematics-Second Series*, 163(1):265–300, 2006.

[4] K. Astala, L. Päivärinta, and M. Lassas. Calderón's Inverse Problem for Anisotropic Conductivity in the Plane. *Communications in Partial Differential Equations*, 30(1):207–224, 2005.

[5] S. Asvadurov, V. Druskin, M.N. Guddati, and L. Knizhnerman. On optimal finite-difference approximation of PML. *SIAM Journal on Numerical Analysis*, 41(1):287–305, 2004.

[6] S. Asvadurov, V. Druskin, and L. Knizhnerman. Application of the difference Gaussian rules to solution of hyperbolic problems. *Journal of Computational Physics*, 158(1):116–135, 2000.

[7] D.C. Barber and B.H. Brown. Progress in electrical impedance tomography. *Inverse Problems in Partial Differential Equations*, pages 151–64, 1990.

[8] J.A. Barcelo, T. Barcelo, and A. Ruiz. Stability of the inverse conductivity problem in the plane for less regular conductivities. *Journal of Differential Equations*, 173(2):231–270, 2001.

[9] T. Barcelo, D. Faraco, and A. Ruiz. Stability of Calderón inverse conductivity problem in the plane. *Journal de mathématiques pures et appliquées*, 2007.

[10] J.G. Berryman. Weighted least-squares criteria for seismic traveltime tomography. *IEEE Transactions on Geoscience and Remote Sensing*, 27(3):302–309, 1989.

[11] O.D. Biesel, D.V. Ingerman, J.A. Morrow, and W.T. Shore. Layered Networks, the Discrete Laplacian, and a Continued Fraction Identity. http://www.math.washington.edu/~reu/papers/current/william/layered.pdf.

[12] L. Borcea. A nonlinear multigrid for imaging electrical conductivity and permittivity at low frequency. *Inverse Problems*, 17(2):329–360, 2001.

[13] L. Borcea, J.G. Berryman, and G.C. Papanicolaou. High-contrast impedance tomography. *Inverse Problems*, 12(6):835–858, 1996.

[14] L. Borcea and V. Druskin. Optimal finite difference grids for direct and inverse Sturm-Liouville problems. *Inverse Problems*, 18(4):979–1002, 2002.

[15] L. Borcea, V. Druskin, and F. Guevara Vasquez. Electrical impedance tomography with resistor networks. *Inverse Problems*, 24(3):035013 (31pp), 2008.

[16] L. Borcea, V. Druskin, and L. Knizhnerman. On the Continuum Limit of a Discrete Inverse Spectral Problem on Optimal Finite Difference Grids. *Communications on Pure and Applied Mathematics*, 58(9):1231, 2005.

[17] L. Borcea, V. Druskin, and A. Mamonov. Solving the discrete EIT problem with optimization techniques, 2007. Schlumberger-Doll Report.

[18] L. Borcea, V. Druskin, and A.V. Mamonov. Circular resistor networks for electrical impedance tomography with partial boundary measurements. *Inverse Problems*, 26(4):045010, 2010.

[19] L. Borcea, V. Druskin, A.V. Mamonov, and F. Guevara Vasquez. Pyramidal resistor networks for electrical impedance tomography with partial boundary measurements. Submitted to Inverse Problems, 2010.

[20] R.M. Brown and G.A. Uhlmann. Uniqueness in the inverse conductivity problem for nonsmooth conductivities in two dimensions. *Communications in partial differential equations*, 22(5):1009, 1997.

[21] A.L. Bukhgeim and G. Uhlmann. Recovering a potential from partial Cauchy data. *Communications in Partial Differential Equations*, 27(3):653–668, 2002.

[22] A.P. Calderón. On an inverse boundary value problem, Seminar on Numerical Analysis and its Applications to Continuum Physics, Soc. *Brasileira de Matematica, Rıo de Janeiro*, pages 65–73, 1980.

[23] M. Cheney, D. Isaacson, and E.L. Isaacson. Exact solutions to a linearized inverse boundary value problem. *Inverse Problems*, 6(6):923–934, 1990.

[24] M. Cheney, D. Isaacson, J.C. Newell, S. Simske, and J. Goble. NOSER: An algorithm for solving the inverse conductivity problem. *International Journal of Imaging systems and technology*, 2(2), 1990.

[25] M.T. Chu and G.H. Golub. Structured inverse eigenvalue problems. *Acta Numerica*, 11:1–71, 2003.

[26] E. Curtis, E. Mooers, and J.A. Morrow. Finding the conductors in circular networks from boundary measurements. *RAIRO - Mathematical Modelling and Numerical Analysis*, 28:781–814, 1994.

[27] E.B. Curtis, D. Ingerman, and J.A. Morrow. Circular planar graphs and resistor networks. *Linear Algebra and its Applications*, 23:115–150, 1998.

[28] E.B. Curtis and J.A. Morrow. *Inverse problems for electrical networks*. World Scientific, 2000.

[29] P.J. Davis. *Circulant matrices*. American Mathematical Society, 1994.

[30] Y.C. de Verdière, I. Gitler, and D. Vertigan. Reseaux electriques planaires II. *Commentarii Mathematici Helvetici*, 71(1):144–167, 1996.

[31] D.C. Dobson. Convergence of a reconstruction method for the inverse conductivity problem. *SIAM Journal on Applied Mathematics*, pages 442–458, 1992.

[32] D.C. Dobson and F. Santosa. An image enhancement technique for electrical impedance tomography. *Inverse Problems*, 10(2):317–334, 1994.

[33] T.A. Driscoll. Schwarz-Christoffel Toolbox Users Guide: Version 2.3, 2002. Department of Mathematical Sciences, University of Delaware, Newark, DE.

[34] T.A. Driscoll and L.N. Trefethen. *Schwarz-Christoffel Mapping*. Cambridge University Press, 2002.

[35] V. Druskin. The unique solution of the inverse problem of electrical surveying and electrical well-logging for piecewise-continuous conductivity. *Izv. Earth Physics*, 18:51–3, 1982.

[36] V. Druskin. On uniqueness of the determination of the three-dimensional underground structures from surface measurements with variously positioned steady-state or monochromatic field sources. *Sov. Phys.–Solid Earth*, 21:210–4, 1985.

[37] V. Druskin and L. Knizhnerman. Gaussian spectral rules for second order finite-difference schemes. *Numerical Algorithms*, 25(1):139–159, 2000.

[38] V. Druskin and S. Moskow. Three-point finite-difference schemes, Pade and the spectral Galerkin method. I. One-sided impedance approximation. *Mathematics of Computation*, 71(239):995–1020, 2002.

[39] I.S. Duff, A.M. Erisman, and J.K. Reid. *Direct methods for sparse matrices*. Oxford University Press, USA, 1986.

[40] A.M. Erisman and W.F. Tinney. On computing certain elements of the inverse of a sparse matrix. *Communications of the ACM*, 18(3):177–179, 1975.

[41] L.C. Evans. *Partial Differential Equations*. AMS, 1997.

[42] I.M. Gel'fand and B.M. Levitan. On the determination of a differential equation from its spectral function. *Izvestiya Rossiiskoi Akademii Nauk. Seriya Matematicheskaya*, 15(4):309–360, 1951.

[43] R.M. Gray. *Toeplitz and circulant matrices: A review*. Now Publishers Inc, 2006.

[44] F. Guevara Vasquez. *On the Parametrization of Ill-posed Inverse Problems Arising from Elliptic Partial Differential Equations*. PhD thesis, Rice University, Houston, TX, USA, 2006.

[45] J. Hadamard. Sur les problemes aux derivees partielles et leur signification physique. *Princeton University Bulletin*, 13(49-52):4, 1902.

[46] H. Heck and J. Wang. Stability estimates for the inverse boundary value problem by partial Cauchy data. *Inverse Problems*, 22(5):1787, 2006.

[47] O.Y. Imanuvilov, G. Uhlmann, and M. Yamamoto. Global uniqueness from partial Cauchy data in two dimensions. *Arxiv preprint arXiv:0810.2286*, 2008.

[48] O.Y. Imanuvilov, G. Uhlmann, and M. Yamamoto. Partial data for the Calderon problem in two dimensions. *Arxiv preprint arXiv:0809.3037*, 2008.

[49] D. Ingerman. Discrete and continuous Dirichlet-to-Neumann maps in the layered case. *SIAM Journal on Mathematical Analysis*, 31:1214–1234, 2000.

[50] D. Ingerman, V. Druskin, and L. Knizhnerman. Optimal finite difference grids and rational approximations of the square root I. Elliptic problems. *Communications on Pure and Applied Mathematics*, 53(8):1039–1066, 2000.

[51] D. Ingerman and J. A. Morrow. On a characterization of the kernel of the Dirichlet-to-Neumann map for a planar region. *SIAM Journal on Applied Mathematics*, 29:106–115, 1998.

[52] D. Isaacson and M. Cheney. Effects of measurement precision and finite numbers of electrodes on linear impedance imaging algorithms. *SIAM Journal on Applied Mathematics*, pages 1705–1731, 1991.

[53] C.E. Kenig, J. Sjostrand, and G. Uhlmann. The Calderon problem with partial data. *Annals of Mathematics-Second Series*, 165(2):567–592, 2007.

[54] R. Kohn and A. McKenney. Numerical implementation of a variational method for electrical impedance tomography. *Inverse Problems*, 6(3):389–414, 1990.

[55] R. Kohn and M. Vogelius. Determining conductivity by boundary measurements. *Communications on Pure and Applied Mathematics*, 37:289–98, 1984.

[56] R. Kohn and M. Vogelius. Determining conductivity by boundary measurements II. Interior results. *Communications on Pure and Applied Mathematics*, 38(5), 1985.

[57] R.V. Kohn and M. Vogelius. Relaxation of a variational method for impedance computed tomography. *Communications on Pure and Applied Mathematics*, 40(6), 1987.

[58] M.A. Lavrentiev and B.V. Shabat. *Methods of the complex variable function theory (in Russian).* Nauka, Moscow, 1987.

[59] B.M. Levitan. *Inverse Sturm-Liouville Problems.* VSP, 1987.

[60] L. Liu. *Stability estimates for the two-dimensional inverse conductivity problem.* University of Rochester. Dept. of Mathematics, 1997.

[61] N. Mandache. Exponential instability in an inverse problem for the Schrodinger equation. *Inverse Problems*, 17(5):1435–1444, 2001.

[62] V.A. Marchenko. *Spectral theory of Sturm-Liouville operators.* Naukova Dumka, Kiev, 1972.

[63] J.L. Mueller, D. Isaacson, and J.C. Newell. A reconstruction algorithm for electrical impedance tomography data collected on rectangular electrode arrays. *IEEE Transactions on Biomedical Engineering*, 46(11):1379–1386, 1999.

[64] J.L. Mueller, D. Isaacson, and J.C. Newell. Reconstruction of conductivity changes due to ventilation and perfusion from EIT data collected on a rectangular electrode array. *Physiological Measurement*, 22(1):97–106, 2001.

[65] J.L. Mueller and S. Siltanen. Direct reconstructions of conductivities from boundary measurements. *SIAM Journal on Scientific Computing*, 24(4):1232–1266, 2003.

[66] J.L. Mueller, S. Siltanen, and D. Isaacson. A direct reconstruction algorithm for electrical impedance tomography. *IEEE Transactions on Medical Imaging*, 21(6):555–559, 2002.

[67] J.L. Mueller, S. Siltanen, and D. Isaacson. A direct reconstruction algorithm for electrical impedance tomography. *IEEE Trans. Med. Imaging*, 21(6):555–559, 2002.

[68] A.I. Nachman. Reconstructions from boundary measurements. *Annals of Mathematics*, pages 531–576, 1988.

[69] A.I. Nachman. Global uniqueness for a two-dimensional inverse boundary value problem. *Annals of Mathematics*, pages 71–96, 1996.

[70] F. Natterer. A discrete Gelfand-Levitan theory. Technical report, Technical report, Institut fuer Numerische und instrumentelle Mathematik, 1994.

[71] E. Reich. Quasiconformal mappings of the disk with given boundary values. *Lecture Notes in Mathematics*, 505:101–137, 1976.

[72] F. Santosa and M. Vogelius. A backprojection algorithm for electrical impedance imaging. *SIAM Journal on Applied Mathematics*, pages 216–243, 1990.

[73] S. Siltanen, J. Mueller, and D. Isaacson. An implementation of the reconstruction algorithm of A Nachman for the 2D inverse conductivity problem. *Inverse Problems*, 16(3):681–700, 2000.

[74] S. Siltanen, J.L. Mueller, and D. Isaacson. Reconstruction of high contrast 2-D conductivities by the algorithm of A. Nachman. In *Radon Transforms and Tomography: 2000 Ams-IMS-Siam Joint Summer Research Conference on Radon Transforms and Tomography, Mount Holyoke College, South Hadley, Massachusetts, June 18-22, 2000*, volume 278, page 241. American Mathematical Society, 2001.

[75] E. Somersalo, M. Cheney, and D. Isaacson. Existence and uniqueness for electrode models for electric current computed tomography. *SIAM Journal on Applied Mathematics*, 52(4):1023–1040, 1992.

[76] E. Somersalo, M. Cheney, D. Isaacson, and E. Isaacson. Layer stripping: a direct numerical method for impedance imaging. *Inverse Problems*, 7:899–926, 1991.

[77] K. Strebel. On the existence of extremal Teichmüller mappings. *Journal d'Analyse Mathématique*, 30(1):464–480, 1976.

[78] K. Strebel. Extremal quasiconformal polygon mappings for arbitrary subdomains of compact Riemann surfaces. In *Annales Academiæ Scientiarum Fennicæ Mathematica*, volume 27, pages 237–248. Academia Scientiarum Fennica, 2002.

[79] J. Sylvester. An anisotropic inverse boundary value problem. *Communications on Pure and Applied Mathematics*, 43(2):201–232, 1990.

[80] J. Sylvester. A convergent layer stripping algorithm for the radially symmetric impedance tomography problem. *Communications in partial differential equations*, 17(11-12):1955–1994, 1992.

[81] J. Sylvester and G. Uhlmann. A global uniqueness theorem for an inverse boundary value problem. *Annals of Mathematics*, 125(1):153–169, 1987.

[82] K. Takahashi, J. Fagan, and M.S. Chen. Formation of a sparse bus impedance matrix and its application to short circuit study. In *Power Industry Computer Applications Conference*, pages 63–69, 1973.

[83] A.N. Tikhonov. Regularization of incorrectly posed problems. *Soviet Math. Dokl*, 4(6):1624–1627, 1963.

[84] A.N. Tikhonov, V.Y. Arsenin, and F. John. *Solutions of ill-posed problems*. VH Winston Washington, DC, 1977.

[85] A. Wexler and C.J. Mandel. Impedance Computed Tomography Algorithm and System for Ground Water and Hazardous Waste Imaging. *Hazardous Wastes in Ground Water: A Soluble Dilemma*, pages 156–161, 1985.